

Structured Non-Noble Metal Catalysts for the Liquid-Phase Reduction of Nitroaromatics

THÈSE N° 7685 (2017)

PRÉSENTÉE LE 16 JUIN 2017

À LA FACULTÉ DES SCIENCES DE BASE

LABORATOIRE DE GÉNIE DE LA RÉACTION CHIMIQUE

PROGRAMME DOCTORAL EN CHIMIE ET GÉNIE CHIMIQUE

ÉCOLE POLYTECHNIQUE FÉDÉRALE DE LAUSANNE

POUR L'OBTENTION DU GRADE DE DOCTEUR ÈS SCIENCES

PAR

Oliver Anthony BESWICK

acceptée sur proposition du jury:

Prof. S. Gerber, présidente du jury
Prof. L. Kiwi, Prof. P. J. Dyson, directeurs de thèse
Dr B. Louis, rapporteur
Prof. A. E. Palomares Gimeno, rapporteur
Dr F. E. Héroguel, rapporteur



ÉCOLE POLYTECHNIQUE
FÉDÉRALE DE LAUSANNE

Suisse
2017

“I learned that courage was not the absence of fear, but the triumph over it. The brave man is not he who does not feel afraid, but he who conquers that fear.”

Nelson Mandela

Remerciements

Un grand nombre de personnes ont contribué à l'accomplissement de ce travail de thèse. Je vais profiter de quelques pages pour leur témoigner ma reconnaissance.

La Prof. Lioubov Kiwi-Minsker m'a donné l'opportunité, il y a 4 ans, d'être le dernier doctorant à réaliser une thèse au GGRC. Du début à la fin, elle m'a accordé son soutien et sa confiance. Ses précieux conseils m'ont aidé dans la rédaction de publications scientifiques, la réalisation de présentations destinées à des conférences internationales ou encore à améliorer mes plans d'expériences. Être son assistant pour les cours donnés aux étudiants en Bachelor et Master en génie chimique, a été une chance immense. Mes connaissances théoriques dans les domaines du dimensionnement de réacteurs chimiques et de la catalyse hétérogène ont été renforcées par le partage de savoir dont elle m'a fait bénéficier. Je remercie donc vivement Lioubov pour cette aventure de longue haleine.

Mes remerciements s'adressent aussi au Prof. Paul Dyson qui a accepté d'être le co-directeur de ma thèse. Il ne s'est pas contenté de revêtir cette casquette pour permettre administrativement la continuation de ce travail après le départ à la retraite de la Prof. Lioubov Kiwi-Minsker mais y a pris pleinement part. Il a grandement contribué à nos trois dernières publications scientifiques, en les relisant avec la plus grande attention et en prodiguant d'excellents conseils qui ont permis de les améliorer. Enfin, le Prof. Paul Dyson a pris le temps de corriger en détail le chapitre de l'état de l'art de cette thèse.

Un grand merci aux membres de mon comité de thèse, à savoir la présidente du jury, la Prof. Sandrine Gerber, et les rapporteurs, le Prof. Antonio Palomares Gimeno, le Dr. Benoît Louis et le Dr. Florent Héroguel pour l'important travail de relecture, les corrections suggérées et l'intéressante discussion qui a suivi ma présentation durant l'examen oral.

Je remercie Igor Iouranov qui a été essentiel tout au long de ce doctorat. Igor a synthétisé mes catalyseurs, m'a porté secours face aux problèmes techniques survenant sur les installations et m'a transmis durant de longues conversations une fraction de son immense savoir en chimie. J'ai aussi apprécié nos riches discussions politiques, d'histoire et voire même sur les subtilités qui entourent la fabrication du whisky.

Mes remerciements vont également au Prof. Albert Renken que j'admire pour son dévouement à la science et plus exactement au génie chimique. Grâce ses explications, le nombre de Thiele et le facteur d'efficacité, notamment, n'ont plus de secret pour moi.

Un grand merci à Danièle Laub, Colette Vallotton, Duncan Alexander et Thomas LaGrange de l'équipe du CIME pour les préparations d'échantillons et les centaines images de microscopie réalisées au cours de cette thèse. Malgré le grand défi que représentait l'imagerie de mes échantillons, des images époustouflantes des minuscules nanoparticules de fer, cobalt ou nickel réparties au sein de fibres de carbone activé, ont pu être obtenues. L'intérêt marqué de Thomas a même permis, au fil des ans, d'observer les colonnes d'atomes des nanoparticules de nickel. Il a été un contributeur majeur de ma thèse, sans qui, la représentation de la phase active de mes catalyseurs n'aurait jamais été aussi bonne.

Je remercie Nicolas Xanthopoulos et Pierre Métraux pour les analyses XPS et leur aide dans l'interprétation de celles-ci.

Mes collègues doctorants et post-doctorants m'ont non seulement aidé pour ma thèse mais ont rendu bien des pauses de midi et soirées mémorables. Leur départ successif au cours des années a laissé un vide considérable. Avant d'être mon collègue, Guillaume m'a supervisé durant mon projet de master au GGRC, mais c'est surtout l'un de mes potes avec qui je pars chaque été autour du monde, et ce depuis notre temps au gymnase de Nyon. Au laboratoire, Guillaume a été un collègue et ami fidèle, qui n'a jamais hésité à interrompre son travail en cours pour m'assister dans la résolution de mes problèmes. Après avoir achevé son doctorat et

déménagé à Berne, diverses choses m'ont manqué : ses entrées intempestives dans mon bureau et celui de mes autres collègues, sans autre réel motif que de faire passer un peu le temps ; nos discussions sur l'actualité ou le football, sujet qui me « passionne » tant. Merci également pour la relecture de la version intermédiaire de ma thèse et les suggestions faites pour l'examen oral de celle-ci. Charline, Daniel et Artur ont tous trois fait partie de « l' open space crew » durant mon projet de master. Cette période n'a été que du pur fun et j'ai eu la chance de les retrouver durant ma thèse. Merci Daniel pour ton aide d'expert en informatique, tes tuyaux sur les meilleurs jeux en ligne du moment, le gaspacho qui s'est si bien associé aux copies d'examen de certains étudiants et plus sérieusement pour ta collaboration sur les articles que nous avons publiés ensemble. Charline, grâce à toi, cette salade que j'avais disposée dans le frigo, je ne l'ai pas oubliée. Tes confitures, mousses au chocolat et gâteaux étaient tout bonnement divins. C'était sympa aussi, les invites Balélec. Mais bien plus important que tes qualités culinaires ou d'organisatrice, c'est ton altruisme, qui m'a qui beaucoup marqué et que tu sembles être parvenue à masquer des étudiants en prétendant être de mauvaise (une bonne technique pour éviter leurs fichues questions !). Artur, dit « Artur voiture » (par certains), est un exemple pour tous. Petit, alors qu'il vivait encore au Tatarstan en Russie, il est tombé sur une pub de Shell à la TV qui contenait leur fameux slogan, « Go well, go Shell », auquel il a directement adhéré. A partir de là, Artur a su qu'il ferait n'importe quoi pour être heureux. Parti de sa région natale, il a étudié la chimie à Moscou, puis il s'est rendu en Suisse à EPFL pour réaliser son projet de master et sa thèse au GGRC. Il y a rencontré sa femme, Irina, qui y faisait son projet de master. Pour finir de l'impressionner et la séduire, il a acheté une Ford Focus. Il vit désormais avec celle qui selon ses propres mots « a changé sa vie », aux Pays-Bas. Là, il travaille pour l'une des plus puissantes entreprises de la planète, Shell. Artur était sans doute l'un des plus drôles du GGRC et celui, de mon point de vue, ayant les meilleurs goûts cinématographiques, film et séries confondus. Merci donc à

Artur, qui m'a beaucoup inspiré. Merci à Julien de m'avoir fait découvrir que jouer au frisbee peut être un sport : l'Ultimate (qu'est-ce qu'on ne ferait pas pour paraître plus cool) ! Julien est également drôle et polyglotte. Alors que j'étais encore étudiant, Julien m'a fait une solide impression lorsqu'il s'est présenté à ma classe durant la première journée des travaux pratiques de génie chimique, arborant sa jolie mèche et son T-shirt rose. Désormais « rangé » depuis son mariage avec Véronica, Julien a un grand passé de séducteur, et c'est avec joie qu'il prodigue des conseils dans ce domaine. Merci à Mica pour la correction de mon projet de master, ses explications de lectrice assidue de Game of Thrones sur la série du même nom et de sa passion affichée pour World of Warcraft. Merci à Fernando de m'avoir proposé un projet de semestre passionnant sur la réduction du *para*-chloronitrobenzene avec un catalyseur à base d'or. Il est l'un de ceux à m'avoir donné goût à ce sujet passionnant. Fernando, brillant chercheur, a été pour moi un modèle en termes de dévouement à la recherche scientifique. Visiter Saint-Petersbourg en sa compagnie et celle de James a été un véritable plaisir, tout comme de participer ensemble à la conférence internationale de catalyse à Kazan. Un grand merci à Anne-Laure, artiste à ses heures, qui a participé à mon éducation, en sa qualité d'assistante pour le cours « théorie des réacteurs ». Anne-Laure aura également été l'experte de mon projet de master et de celui de Pauline, ma dernière étudiante en projet de master.

Je tiens à remercier les étudiants qui ont collaboré à la réalisation de ce travail. Merci à Alex, pour tout son travail sur les catalyseurs à base de cobalt, utilisés en hydrogénation catalytique par transfert. Félicien Muriset est le premier étudiant en projet de master que j'ai eu l'opportunité de superviser. Grâce aux excellents résultats avec des catalyseurs à base de nickel qu'il a produit, ma compréhension de ces derniers s'est grandement affinée. Partager mon bureau avec lui a été une superbe expérience. Sa gentillesse et son professionnalisme dans l'art de faire la fête m'auront marqué. Boire des bières en sa compagnie a été un plaisir. Vivement la prochaine. Quant à Pauline, qui a été ma deuxième et dernière étudiante en projet

de master, elle a non seulement fourni un travail fourni de qualité sur les sujets qui lui ont été attribué mais elle a également été la pâtissière en cheffe du laboratoire durant près de 5 mois. La pause-café, faisant suite à la pause de midi, a été « pimpée » du jeu du pendu grâce à Pauline et Carine.

Merci à Loïc Obserson et Saeed Mohammadi Siyani qui ont produit d'incroyables images de microscopie électronique de mes catalyseurs durant, respectivement, leur projet de semestre et de master. Merci à Sebdiel Reyes pour les résultats obtenus durant ses trois mois de stage, entre avril et juin 2014.

Les deux apprentis que j'ai eu la chance de côtoyer ont fourni une quantité folle de résultats. J'ai été plus d'une fois saisi par leurs impressionnantes connaissances en chimie. Merci à Ivan Cornu, expérimentateur de talent, pour les nombreuses expériences qu'il a su mener avec brio et le partage scientifique que nous avons eu durant sa période au GGRC. Merci à Bryan Dousse pour son immense travail à réaliser et planifier des expériences utiles à ma thèse de mars 2015 à août 2016. Il a repris la place de Félicien dans mon bureau avec maestria car il m'a branché sur d'excellentes chaînes Youtube, tant scientifiques que culturelles. Outre la chimie et la science en général, son intérêt pour la culture japonaise, l'escrime, la musique ou encore les jeux vidéo est marquant.

Je remercie également l'équipe de l'atelier mécanique et électronique pour leur fréquent support sur des installations défectueuses et dans certains cas l'amélioration de celles-ci. Je tiens également à remercier les gens de magasin de chimie, Jacky et Marie, pour leur assistance et leur ouverture à tchatcher 5–15 min après mes achats. Un grand merci à Sandra, Madeleine, Rachel et Anne Lene pour leur aide soutenue du côté administratif.

Enfin il me reste à remercier mes amis et ma famille, sans qui, je ne serais pas parvenu au terme de cette aventure. Greg, Dimi, Thùý Chàu, sont mes amis de longue date qui m'ont

grandement aidé à relativiser la situation. J'ai hâte de boire des verres en votre compagnie tout en visionnant la saison 7 de GoT. Merci à Amaël, Falouz, Jules, Baur et Greg pour tous les moments incroyables passés en Suisse ou à l'autre bout du monde, sobres ou enivrés.

Enfin un merci sans limite à ma famille, d'abord mon frère Gregory (qui fût un jour Diamant sur « League ») et sa copine Titi, et bien sûr mes parents, Sonia et Richard, qui m'ont soutenu, encouragé et apporté bien plus que ce dont j'avais besoin, et ce depuis le tout début. Grâce à vous, je suis finalement arrivé au bout !

Big up à ceux que j'ai volontairement oublié !

Abstract

The industrial production of aromatic amines, essential intermediates for the synthesis of several drugs, dyes, pigments and agrochemicals, requires the use of heterogeneous catalysis. These molecules were formerly produced by the Béchamp reduction, a non-catalytic batch process requiring costly downstream separation steps. Catalytic approaches afford the implementation of continuous processes producing less waste. While it is generally not the primary goal when improving processes to make them more environmentally friendly, it is often one of the consequences, thereby improving the image of the chemical industry. The development of new catalysts is one of the major axes for optimizing industrial production of chemicals. Often multidisciplinary, it involves a better understanding of existing systems, advances in characterization and modelling techniques for the discovery of new catalytic materials.

This thesis aims at designing new catalysts based on non-noble metals (*e.g.* Fe, Co, Ni) for the chemoselective hydrogenation of nitroaromatics in the liquid phase. The use of activated carbon fibres (ACFs) as a structured support has been at the centre of the strategy applied during this work in order to develop new catalysts capable of surpassing the best systems based on Fe, Co or Ni. The high porosity of ACFs, composed of very thin pores (~ 2 nm) and a high specific surface area, has been exploited to generate and stabilize highly dispersed crystallites of active phase.

The formation of ~ 2 nm metal oxides (MO_x) nanoparticles (NPs) resulting from the impregnation/pyrolysis of Fe, Co or Ni precursors within the ACFs was performed. The reduction of nitroaromatics with different functional groups was carried out by catalytic hydrogenation with molecular hydrogen and by catalytic transfer hydrogenation (CTH) with

hydrazine as reducing agent. The MO_x/ACF catalysts were shown to be active and selective under mild conditions in the CTH of *para*-chloronitrobenzene (*p*-CNB) to *para*-chloroaniline (*p*-CAN). The FeO_x/ACF was tolerating many substituents of nitroarenes during the $-\text{NO}_2$ hydrogenation. The $\text{CoO}_x/\text{ACF}_{\text{HNO}_3}$ catalyst was less active compared to the Fe-based catalyst but afforded a *meta*-vinylaniline (*m*-VA) yield above 99% during the reduction of the *meta*-nitrostyrene (*m*-NS), exceeding, to the best of our knowledge, the best performance reported to date.

The very low activity of the NiO_x/ACF catalyst in CTH has prompted us to test Ni-based catalyst in the hydrogenation of nitroarenes with gaseous hydrogen. Raney Nickel is a well-known catalyst used in industry for this reaction. First, the existence of particles size effects was evaluated using unsupported Ni PVP-stabilized NPs (2–14 nm). An antipathetic structure sensitivity of the *meta*-dinitrobenzene (*m*-DNB) hydrogenation to *meta*-nitroaniline (*m*-NAN) was demonstrated, showing a 4.6-fold increase in the turnover frequency over the 14 nm NPs. Once supported on ACFs and cleaned from PVP by a UV-ozone treatment, the 2 nm Ni NPs afforded an increase of selectivity towards *m*-NAN from 34 to 96% at close to full conversion ($X_{m\text{-DNB}} = 99\%$). The selective transformation favouring *m*-NAN has been attributed to reactions taking place at the edges and vertices of the NPs. The Langmuir-Hinshelwood two-site kinetic model was consistent with the experimental data. The incorporation of gold to form Ni-Au (1:1) bimetallic NPs led to a significant increase in the selectivity (99%), possibly by mimicking the electronic properties of the edges/vertices of the monometallic Ni NPs. Moreover, the catalytic activity of the Ni-Au NPs was increased by supporting them on ACFs and cleaning them from PVP.

The next step in our work was devoted to the simplification of Ni/ACF catalysts preparation targeting formation of small (< 2 nm) NPs by impregnation/pyrolysis followed by an *in-situ* activation under the reaction conditions. The creation of additional surface oxygen-

containing groups on the ACFs prior to impregnation by Ni precursor resulted in 3-fold increase of the transformation rate during the conversion of *p*-CNB to *p*-CAN, while maintaining the *p*-CAN selectivity above 99%. The increase in activity was ascribed to an electronic contribution of the surface O-containing groups on the nickel catalytic surface.

The careful nanocatalysts design, guided by detailed structural characterization and mechanistic study, has led to highly selective catalysts of industrial relevance. Finally, the excellent hydrodynamic properties of the catalytic bed with structured ACF-based materials, as compared to randomly packed powders or pellets, make them highly suitable for the continuous reactors used in multi-phase processes.

Keywords: Activated carbon fibres (ACFs), Fe, Co, Ni, nanoparticles, catalytic reduction, hydrazine, hydrogen, nitroaromatics, structured catalysts

Version Abrégée

La production industrielle d'amines aromatiques, intermédiaires essentiels à la production de nombreux médicaments, colorants, pigments ou produits chimiques, repose sur l'utilisation de la catalyse hétérogène. Ces molécules étaient autrefois produites par la réduction Béchamp, un procédé non-catalytique discontinu nécessitant des étapes de séparation coûteuses. Les approches catalytiques permettent l'implémentation de procédés continus produisant moins de déchets. Si l'amélioration des procédés n'a généralement pas pour but premier de les rendre plus respectueux de l'environnement, elle en est souvent l'une des conséquences, améliorant ainsi l'image de l'industrie chimique.

Cette thèse vise à concevoir des nouveaux catalyseurs basés sur des métaux non-nobles (*e.g.* Fe, Co, Ni) pour l'hydrogénation chemoselective de nitroaromatiques en phase liquide. L'utilisation de fibres de carbone activé (ACFs), comme support structuré, a été au centre de la stratégie employée durant ce travail afin de développer des nouveaux catalyseurs en mesure de surpasser les meilleurs systèmes à base de Fe, Co ou Ni. La porosité élevée des ACFs, composés de pores très fins (~ 2 nm) et d'une grande surface spécifique, a été exploitée pour générer et stabiliser des cristallites de phase active hautement dispersés.

La création de nanoparticules (NPs) d'oxydes de métal (MO_x) d'environ 2 nm, obtenues par imprégnation en voie sèche/pyrolyse des précurseurs de Fe, Co ou Ni au sein des ACFs, a été réalisée. La réduction catalytique de nitroaromatiques avec différents substituants a été menée par hydrogénation avec de l'hydrogène moléculaire et par hydrogénation par transfert (CTH) avec de l'hydrazine comme agent réducteur. Les catalyseurs MO_x/ACF se sont révélés actifs et sélectifs lors de l'hydrogénation par transfert (CTH) du *para*-chloronitrobenzene en *para*-chloroaniline. Le catalyseur FeO_x/ACF s'est montré tolérant vis-à-vis de plusieurs

groupes fonctionnels de nitroarènes durant la réduction du groupe $-NO_2$. Le catalyseur CoO_x/ACF_{HNO_3} a été moins actif que son analogue à base de fer mais a permis un rendement en *m*-nitroaniline (*m*-NAN) supérieur à 99% durant la transformation du *m*-nitrostyrene (*m*-NS), surpassant, à notre connaissance, les meilleures performances reportées à ce jour.

L'activité très faible du catalyseur NiO_x/ACF en CTH nous a poussé à tester des catalyseurs reposant sur du nickel dans l'hydrogénation de nitroarènes avec de l'hydrogène moléculaire. Dans un premier temps, l'existence d'effets de taille a été évaluée en utilisant des NPs (2–14 nm) non-supportées de Ni stabilisées par du PVP. Une sensibilité à la structure antipathétique de l'hydrogénation partielle du *m*-dinitrobenzene (*m*-DNB) en *m*-nitroaniline (*m*-NAN) a été démontrée, le nombre de cycles catalytiques ayant augmenté par un facteur 4.6 sur les NPs de 14 nm. Une fois supportées (ACFs) et nettoyées de leur PVP par un traitement aux UV-ozone, les NPs de 2 nm de nickel ont permis une augmentation de la sélectivité vis-à-vis du *m*-NAN de 34 à 96% à conversion quasi complète ($X_{m-DNB} = 99\%$). La transformation sélective favorisant le *m*-NAN a été attribuée aux arêtes et vertex des nanoparticules. Le modèle cinétique de Langmuir-Hinshelwood s'est bien adapté aux données expérimentales, en admettant un mécanisme à deux sites. L'incorporation d'or pour former des NPs bimétalliques Ni-Au (1:1) a permis une augmentation significative de la sélectivité (99%), plausiblement en imitant les propriétés électroniques des arêtes/vertex des NPs monométalliques de Ni. Finalement, l'activité catalytique des NPs bimétalliques de Ni-Au a été augmentée en les supportant sur des ACF et en les nettoyant de leur PVP.

La prochaine étape de ce travail a été dédiée à la simplification de la préparation des catalyseurs Ni/ACF, en visant la formation de petites (< 2 nm) NPs par imprégnation en voie sèche/pyrolyse suivie d'une activation *in-situ* sous conditions réactionnelles. La création de groupes supplémentaires contenant de l'oxygène sur la surface des ACFs, avant l'étape d'imprégnation, a augmenté par un facteur trois la vitesse catalytique durant la transformation

du *p*-CNB en *p*-CAN. La dispersion n'ayant pas changé, ce changement d'activité a été imputé à une contribution électronique des groupes de surface contenant de l'oxygène sur la surface catalytique de nickel.

La conception minutieuse des nanocatalyseurs, orientée par une caractérisation détaillée, couplée à une étude mécanistique, a mené à des catalyseurs très sélectifs et d'importance industrielle. Enfin, les excellentes propriétés hydrodynamiques des lits catalytiques composés de matériaux structurés à base d'ACFs, plutôt que des poudres ou granules arrangées de façon aléatoire, les rendent parfaitement adaptés à des réacteurs continus utilisés dans des réactions multi-phases.

Mots-clés: Fibres de carbone activé (ACFs), Fe, Co, Ni, nanoparticules, réduction catalytique, hydrazine, hydrogène, nitroarènes, catalyseurs structurés.

Contents

Remerciements.....	i
Abstract.....	vii
Version Abrégée	x
Contents	xiii
List of Symbols	xvi
1 Introduction.....	1
1.1 Motivation and Objectives.....	1
1.2 Structure of the work	3
2 State of the Art.....	5
2.1 Methodologies for the reduction of nitroaromatics	5
2.1.1 Importance of functionalized anilines.....	5
2.1.2 First industrial process: the Béchamp reduction.....	5
2.1.3 Mechanism.....	6
2.1.4 Catalytic hydrogenation of nitroarenes	8
2.1.5 Latest Research	10
2.1.6 Catalytic Transfer hydrogenation (CTH) of nitroarenes.....	20
2.2 Structured supports for catalytic applications	23
2.2.1 Types of structured supports.....	23
2.2.2 Activated carbon fibres (ACFs) as supports	25
2.2.3 ACFs surface modifications.....	25
2.3 Catalyst Optimization for Hydrogenation Reactions.....	27
2.3.1 Role of the Support in Catalytic Hydrogenation (catalyst promotion)	27
2.3.2 Effect of Metal Particle Size on Catalyst Performance	30
3 Experimental.....	33
3.1 Preparation of catalysts.....	33
3.1.1 Unsupported Ni, Au and Ni-Au NPs	33
3.1.2 Preparation of Structured ACFs-based Catalysts.....	36
3.1.3 Raney Nickel catalyst	39
3.2 Liquid-phase hydrogenation of nitroaromatic compounds.....	39
3.2.1 Semi-batch reactor set-up	39
3.2.2 CTH over structured MO _x /ACF (M = Fe, Co, Ni).....	40
3.2.3 Hydrogenation with H ₂ over unsupported Ni, Au and Ni-Au NPs.....	41

3.2.4	Hydrogenation with H ₂ over ACFs-supported Ni and Ni-Au NPs catalysts ..	42
3.2.5	Hydrogenation over structured Ni/ACF catalysts.....	42
3.2.6	Model reactions.....	43
3.3	Analytical method.....	46
3.4	Characterization techniques.....	47
3.4.1	Atomic absorption spectroscopy (AAS).....	47
3.4.2	N ₂ physisorption.....	47
3.4.3	X-ray diffraction (XRD).....	48
3.4.4	X-ray photoelectron spectroscopy (XPS).....	49
3.4.5	Scanning electron microscopy.....	49
3.4.6	Transmission electron microscopy (TEM).....	50
3.4.7	Temperature-programmed reduction in hydrogen (TPR).....	51
3.4.8	Temperature-programmed decomposition (TPD).....	51
4	Highly Dispersed Non-Precious Metal Oxides Nanoparticles on Activated Carbon Fibres as Efficient Structured Catalysts for the Transfer Hydrogenation of Nitroarenes	53
4.1	Introduction	55
4.2	Experimental.....	57
4.3	Results and Discussion	58
4.3.1	Characterization of the MO _x /ACF catalysts	58
4.3.2	Catalytic testing of the MO _x /ACF catalysts.....	64
4.3.3	Reduction of <i>m</i> -nitrostyrene	74
4.4	Conclusions	84
5	Highly Selective Immobilized Bimetallic Ni-Au Nanoparticle Catalyst for the Partial Hydrogenation of <i>m</i> -dinitrobenzene	87
5.1	Introduction	89
5.2	Experimental.....	90
5.3	Results and Discussion	91
5.3.1	Preparation and characterization of the Ni NPs.....	91
5.3.2	Evaluation of the Ni NPs in the catalytic partial hydrogenation of <i>m</i> -DNB ..	93
5.4	Conclusions	111
6	Ni-based Structured Catalysts for Selective 3-Phase Hydrogenation of Nitroaromatics.....	113
6.1	Introduction	115
6.2	Experimental.....	117
6.3	Results and Discussion	118
6.3.1	Catalyst Characterization.....	118

6.3.2	Temperature Programmed Decomposition (TPD) and reduction (TPR)..	119
6.3.3	Catalytic results.....	126
6.4	Conclusions	133
7	General Conclusions and Outlook	135
7.1	Achieved results	135
7.2	Outlook	137
8	Appendix.....	141
9	References.....	145
10	Curriculum Vitae	155

List of Symbols

Abbreviations

AAS	Atomic absorption spectroscopy
AC	Activated carbon
ACF	Activated carbon Fibre
ALD	atomic layer deposition
BE	Binding energy
BET	Brunauer, Emmet and Teller
CCVD	Catalytic chemical vapour deposition
CNF	Carbon nanofibre
CNS	Carbon nanosphere
CNT	Carbon nanotube
CSTR	Continuous stirred tank reactor
EDX	Energy dispersive X-ray spectroscopy
EQ	Equivalents
GC	Gas chromatography
HAADF	High-angle annular dark-field imaging
HRSEM	High resolution scanning electron microscopy
HRSTEM	High resolution scanning transmission electron microscopy
M	Metal
MS	Mass spectrometer
<i>m</i> -EA	<i>meta</i> -ethylaniline
<i>m</i> -ENB	<i>meta</i> -ethylnitrobenzene
<i>m</i> -NS	<i>meta</i> -nitrostyrene
<i>m</i> -VA	<i>meta</i> -vinylaniline
<i>m</i> -DNB	<i>meta</i> -dinitrobenzene
<i>m</i> -NAN	<i>meta</i> -nitroaniline
<i>m</i> -PDA	<i>meta</i> -phenylenediamine
NA	Non-available

NC	Nitroaromatic compounds
NP	Nanoparticle
<i>p</i> -CAN	<i>para</i> -chloroaniline
<i>p</i> -CNB	<i>para</i> -chloronitrobenzene
PSD	Particles size distribution
PVP	Poly(N-vinyl-2-pyrrolidone)
RA	Reducing agent
RaNi	Raney nickel
RDS	Rate determining step
RT	Room temperature
SEM	Scanning electron microscopy
SMSI	Strong metal-support interactions
SSA	Specific surface area
STEM	Scanning transmission electron microscopy
SBR	Signal-to-background ratio
STM	Scanning tunneling microscope
STP	Standard temperature and pressure
TCD	Thermal conductivity detector
TEM	Transmission electron microscopy
TOF	Turnover frequency
TPD	Temperature-programmed desorption
TPR	Temperature-programmed reduction
UVO	Ultraviolet-ozone
v/v	Volume/volume
wt. %	Percentage by weight
XPS	X-ray photoelectron spectroscopy
XRD	X-ray diffraction

Greek symbols

θ_i	Surface coverage of compound i
------------	--------------------------------

Roman symbols

C	BET constant	(-)
---	--------------	-----

C_i	Concentration of compound i	($\text{mol}\cdot\text{m}^{-3}$)
d	Diameter	(nm)
D	Dispersion	(-)
EA	Activation energy	($\text{kJ}\cdot\text{mol}^{-1}$)
I	Intensity	
k_i	Kinetic constant of reaction i	
K_i	Adsorption constant of compound i	($\text{cm}^3\cdot\text{mol}^{-1}$)
m	Equivalent edge atoms	(-)
n_i	Amount of compound i	(mol)
P	Pressure	(bar)
r_i	Reaction i	
R_i	Transformation rate of compound i	($\text{mol}\cdot\text{mol}^{-1}\cdot\text{s}^{-1}$)
R	Gas constant	($\text{J}\cdot\text{mol}^{-1}\cdot\text{K}^{-1}$)
S_i	Selectivity towards compound i	(%)
t	Time	(s) or (min)
t	thickness	(nm)
T	Temperature	(K)
V	Volume	(cm^3)
V_m	N_2 monolayer volume	(cm^3)
V_p	Pore volume	($\text{cm}^3\cdot\text{g}^{-1}$)
x_i	Fraction of types of surface atoms	(-)
X_i	Conversion of compound i	(%)
Y_i	Yield in compound i	(%)
Z	Atomic number	(-)

Subscripts

ΔT	Cleaned by pyrolysis
D	<i>meta</i> -dinitrobenzene
i	Generic compound
H_2	Hydrogen
HNO_3	Treatment by nitric acid
N	<i>meta</i> -nitroaniline
P	<i>meta</i> -phenylenediamine

σ_1	Plane atoms sites
σ_2	Edge and vertex atoms sites
tot	Total
UVO	Cleaned by UV-ozone

Chapter 1

Introduction

This chapter presents the context, the motivations and objectives of this work.

1.1 Motivation and Objectives

The role of heterogeneous catalysis in chemical industry is ubiquitous as 90% of all processes rely on solid catalysts. The higher selectivities achieved with catalytic processes compared non-catalytic syntheses reduces the amount of waste generated and the number of downstream separation steps. In a competitive environment, manufacturers constantly seek to make their processes more efficient. On the other side, they are bound to comply with the legislative constraints implemented to protect the public and environment from the potential danger of industrial activities. The existence of these two driving forces, economic and legislative, explains the perpetual commitment of industries to optimize their processes. The development of catalysts is an integral part of the optimization. It benefits from technological advances in the synthesis and characterization of catalysts combined with improvements in theory and modelling of catalytic phenomena. Academia can play an important role in the improvement of industrial production by helping find new viable solutions, which not only meet industrial standards, but also are in line with the goal of producing goods in a sustainable manner.

The present thesis focuses on an important reaction performed by the chemical industry, *i.e.* the hydrogenation of functionalised nitroarenes into their corresponding anilines. Drugs, dyes and pigments are examples, among many others, of end products that are synthesized from these molecules.

The difficulty of this reaction lies in the ability to selectively reduce the nitro group without affecting other functionalities attached to the aromatic ring. For instance, during the hydrogenation of *meta*-nitrostyrene and *para*-chloronitrobenzene the reduction of the vinyl group and cleavage of the C-Cl bond should be avoided.

The catalysts employed in the liquid phase for this reaction are generally based on powders with supported metals like palladium and platinum. Mass transfer, separation and recycling limitations are the main drawbacks associated with these catalysts. We therefore decided to develop structured catalysts as they are easy to handle and reuse. Regarding the dispersion and structure of the active phase, the porosity, morphology and surface chemical properties of supports are of the highest importance. Activated carbon fibres (ACFs) have very thin micropores (< 2 nm) and a large surface versatile towards chemical composition, allowing the generation of small tuneable crystallites. Therefore, we decided to use them as the support. Iron, cobalt and nickel were the metals of choice as they are much less expensive and more abundant than noble metals but are usually poor catalysts for the hydrogenation of nitroarenes. However, iron oxide was reported to transform nitro aromatics into anilines by catalytic transfer hydrogenation (CTH) in high yield using hydrazine as the hydrogen donor. Therefore, we synthesized small Fe, Co and Ni nanoparticles (~2 nm) supported on ACFs and evaluated them in the CTH of aromatic nitro-compounds.

For the H₂-assisted hydrogenation of nitroaromatics, Ni-based catalysts (like Raney nickel) have been reported. They suffer from separation and recycling issues and they usually require additives to ensure good selectivities. Therefore, we decided to develop structured

Ni/ACF catalysts for this reaction. First, the use of unsupported nanoparticles (NPs) of different sizes was performed to examine the existence of possible size effects in the hydrogenation of *meta*-dinitrobenzene. The small Ni NPs, measuring around 2 nm, were found active and selective. Subsequently, the optimized preparation by conventional methods has been addressed.

In summary, this thesis demonstrates the rational design approach for the development of structured catalysts based on non-precious metals effective in the selective hydrogenation of nitroarenes using molecular hydrogen or hydrazine.

1.2 Structure of the work

The current state-of-the art in connection to this thesis is reviewed in **Chapter 2**. **Chapter 3** comprises the experimental details which includes the protocols employed for preparing the catalysts, characterization techniques and analytic methods. **Chapters 4, 5 and 6** contain the main results obtained.

Chapter 4 is devoted to the Fe, Co and Ni oxide NPs supported on ACF (MO_x/ACF) for the liquid-phase catalytic transfer hydrogenation (CTH) of nitroarenes into their corresponding anilines. The catalysts were consisting of ~2 nm metal oxides NPs prepared by the incipient wetness impregnation method and tested in the reduction of *para*-chloronitrobenzene (*p*-CNB) using hydrazine as reducing agent. The catalysts stability and their versatility towards functional groups was demonstrated. The reduction of *meta*-nitrostyrene (*m*-NS) exclusively into *meta*-vinylaniline (*m*-VA) was achieved with the CoO_x/ACF_{HNO3} catalyst ($Y_{m-VA} > 99\%$) by adding oxygen-containing groups on the ACFs surface.

Chapter 5 describes the development of nickel-based catalysts for the partial hydrogenation of *meta*-dinitrobenzene (*m*-DNB) into *meta*-nitroaniline (*m*-NAN). The catalytic response of poly(N-vinyl-2-pyrrolidone) (PVP)-stabilized unsupported Ni NPs (2–14 nm), prepared *via* colloidal method, led to the establishment of a structure sensitivity. To minimize the creation of the unwanted phenylenediamine (*m*-PDA) product, the NPs were subsequently stabilized on ACFs. The deposited NPs were cleaned from the PVP, either by a UV-ozone treatment (UVO) or by pyrolysis, as PVP was believed to affect the *m*-NAN selectivity. To further improve the *meta*-nitroaniline selectivity, bimetallic nickel-gold NPs were prepared.

Chapter 6 is concerned with the preparation of small ACF-supported Ni nanoparticles (< 2 nm) by incipient wetness impregnation for the hydrogenation of nitroaromatics. Oxidation of the catalysts stored in the open air was evaluated and the experimental procedure adjusted to maximize the transformation rate of *p*-CNB into *p*-CAN. The influence of ACF support functionalization by nitric acid on the catalytic response of Ni/ACF catalysts is also discussed.

Chapter 7 summarizes the main findings and conclusions of this study and provides an outlook for future research.

Chapter 2

State of the Art

2.1 Methodologies for the reduction of nitroaromatics

2.1.1 Importance of functionalized anilines

Industrial organic chemistry plays a major role for providing various materials important for modern life. Aryl amines are widely used in the chemical industry as ubiquitous building blocks and intermediates for producing bio-active compounds (pharmaceuticals, vitamins, food additives), fine (agrochemicals, dyes, and pigments) and bulk chemicals (polymers).¹ They are also precursors for many intermediates like imines, amides, and diazonium salts which are further used for the synthesis of products with different functional groups. One of the final products requiring aniline as a starting material is polyurethane, a component used for the production of foams, adhesives, surface coatings, elastomers, synthetic fibres, etc. Bayer *MaterialScience* has recently negotiated with DuPont a strategic purchase, the acquisition of an aniline plant, demonstrating the importance of this molecule.

2.1.2 First industrial process: the Béchamp reduction

The majority of the aryl amines syntheses have been carried out in the past *via* non-catalytic routes like the Béchamp reduction of nitroarenes, which is a century-old process.² Introduced in 1854, the Béchamp reduction was the first industrial synthesis of aniline. The reaction is performed in an acid medium (*e.g.* hydrochloric or formic acid) and in presence of iron

(cf. (2.1)).²



The process has been solely run to manufacture aryl amines until 1960, when catalytic more advantageous processes have begun to be commissioned. Despite limited aniline yields ($Y = 90\text{--}95\%$), the generation of large amount of wastes and the requirement of expensive separation methods, the whole process remained economically viable thanks to the iron oxide (Fe_3O_4) as valuable co-coproduct.³ Nowadays, two Bayer plants still operate this process producing the Fe_3O_4 used as pigments.¹

2.1.3 Mechanism

In 1898, Fritz Haber proposed an elaborated reaction pathway for the reduction of nitroarenes to the corresponding anilines by molecular hydrogen.⁴ Three moles of molecular hydrogen are necessary to fully hydrogenate the nitro group. The network consists of two possible reaction routes: a *Direct route* comprising two intermediates, nitrosobenzene and phenylhydroxylamine, and a *Condensation route* comprising in addition to these intermediates, three more: azoxybenzene, azobenzene and hydrazobenzene (cf. **Figure 2.1**). Formation and accumulation of the intermediates depends on the reaction conditions. For example, the azoxybenzene was shown to accumulate with Pd/SiO₂ as catalyst,⁵ whereas hydrazobenzene can also accumulate when reaction is performed at room temperature.

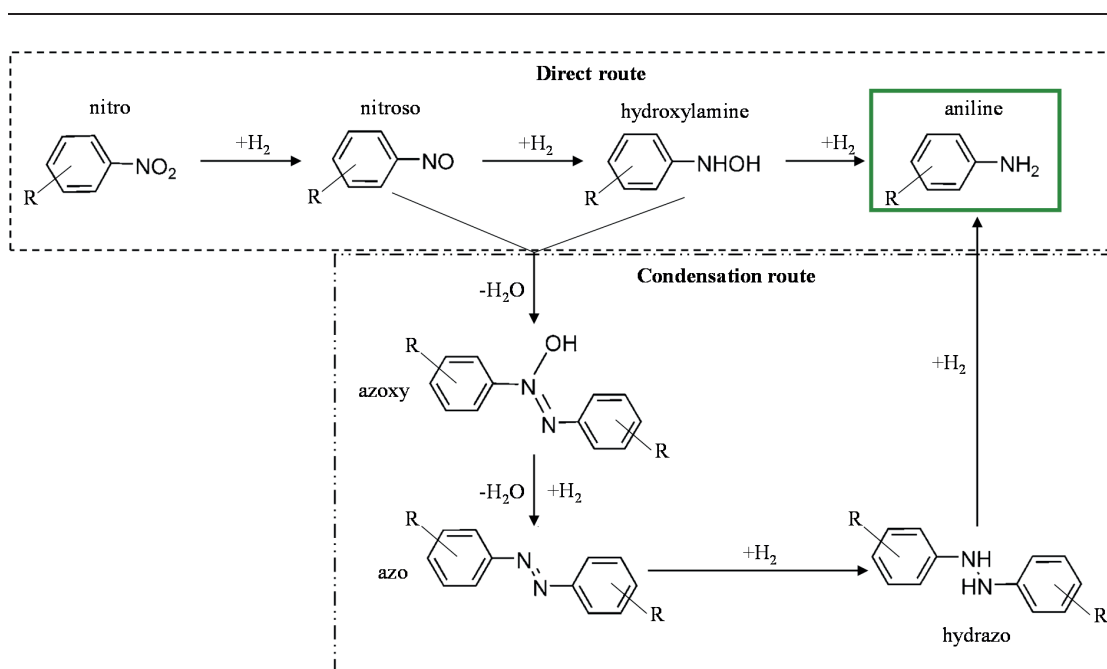
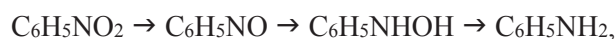


Figure 2.1. Reaction network for the reduction of nitroaromatic compounds.

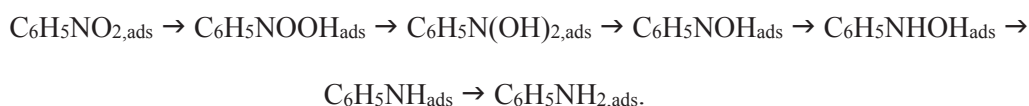
In view of aniline derivatives production on an industrial scale, accumulation of intermediates is a big concern.⁶ These intermediates are explosive and present health issues, *i.e.* irritant, harmful and mutagenic.⁷ Moreover, the Haber's reaction scheme was sometimes doubted due to observed reaction kinetics which do not fit the above network. Wisniak *et al.* suggested that some surface intermediates were not identified.⁸

The veracity of the pathways was addressed by Gelder *et al.* who employed palladium and Raney nickel catalysts.⁴ Very different aniline production rate was measured when employing nitrosobenzene rather than nitrobenzene as starting reactant. Besides, the use of deuterium for the reduction of nitrobenzene showed that its consumption was less rapid than hydrogen. Opposite isotopic effects were observed when nitrosobenzene served as the substrate. Rather than being an inevitable intermediate to reach aniline, the following the sequence was proposed:



where nitrosobenzene can be formed from a direct intermediate produced after several reactional steps. Adsorbed C_6H_5NOH was speculated.

Density functional theory (DFT) modelling applied to nitrobenzene reduction over Pt(111) confirmed these findings,⁹ also including C_6H_5NOH as a direct intermediate for reaching the sequence:



2.1.4 Catalytic hydrogenation of nitroarenes

Given the economic, environmental and efficiency advantages offered by catalysis, it is no surprise to observe the omnipresence of heterogeneous catalysts in the chemical industry.¹⁰ Raw materials can be transformed into a wide variety of products, ranging from building blocks to fine chemicals. In the early 90s the chemical products and processes relying on catalysis were estimated in the USA to represent 60% and 90%, respectively.¹¹ Worldwide, it is estimated that 10–20% of the reactions performed to produce chemicals are catalytic hydrogenations.¹² Also, roughly 10% of all chemical steps to produce pharmaceuticals, vitamins and fine chemicals in *Roche* are catalytic three-phase hydrogenations, demonstrating the importance of hydrogenations held in the liquid phase.¹³

In general, key properties for catalysts are high activity and selectivity, stability over reuse and ease of separation. The difficulty in obtaining the desired product, while suppressing the formation of unwanted by-products depends on the complexity of the substrate, the reaction and its conditions and the choice of catalyst.

The production of nitroarenes has also benefited from the advances in industrial catalysis. The next paragraphs review the major industrial processes.

2.1.4.1 Gas-phase industrial processes

The first industrial catalytic hydrogenation process was introduced by *American Cyanamid* in 1958.³ Except for petrochemicals intermediates, this continuous process performed in the gas-phase was one of the first to involve a fluidized-bed. The hydrogenation is performed between 473–573 K over a silica-supported copper catalyst promoted with chromium, zinc and barium.^{1,3} When deposited on pumice, copper is also used in the fixed-bed of the *Lonza* process operated by *First Chemical Corporation*. Similarly, aniline production by *Bayer* involves a fixed-bed reactor but composed of a palladium-on-alumina catalyst modified by vanadium and lead. These industrial processes require hydrogen to be present in excess in the gas stream in order to reach high yield ($Y > 99\%$) of aniline.

2.1.4.2 Liquid-phase industrial processes

Around the same period, in 1964, *Imperial Chemical Industries* launched a new continuous liquid-phase process for manufacturing aniline based on catalytic hydrogenation of nitrobenzene. Interestingly, aniline itself serves as the solvent. The operated temperature (433–448 K under 1 atm) close or equal to the aniline boiling point (457.3 K), combined with the heat generated by the reaction results in the evaporation of aniline, part of which is recycled back to the reaction vessel.¹⁴ Consequently, the steady-state is ensured. Among the nickel, palladium, cobalt or copper based catalysts suitable for the reaction, nickel-on-kieselguhr or nickel deposited on silica are mentioned as the catalysts of choice. Shortly after, *DuPont* patented their own continuous liquid-phase based on a carbon-supported platinum–palladium catalyst promoted by iron.¹⁵ About 99% yields are claimed during the hydrogenation of a variety of aromatic nitrocompounds, including, notably, nitrobenzene, dinitrobenzenes, nitrotoluenes, nitronaphthalenes and nitrodichlorobenzenes.

The next section is devoted to the current state-of-the art regarding the reduction of nitroarenes to their corresponding anilines and notably *p*-chloronitrobenzene, and *m*-

nitrostyrene. Once reduced, these molecules are of crucial importance for the chemical industry.

2.1.5 Latest Research

2.1.5.1 Chloronitrobenzene hydrogenation

Blaser *et al.* identified in their latest review the benchmark catalysts used in 1998 for the hydrogenation of the main classes of aromatic nitro compounds.¹⁶ Raney nickel with N-based additives, Cu/Fe-doped Ir/C and Pt/C are the catalysts of choice for nitroarenes with chloride substituents. The following sections discuss these systems and the latest developments. Homogeneous systems are excluded from this review due to their low industrial potential for the hydrogenation of nitroarenes.¹⁶

Pt and Ir based catalysts

After modification (not specified) of a charcoal-supported Pt catalyst, Johnson Matthey was able to produce 4-chloroaniline in high yield (98.8%).¹⁷ Interestingly, no additives were necessary to suppress from dehalogenation. It is noteworthy that 3 orders of magnitude higher specific reaction rates over this catalyst are achieved as compared to RaNi. The superior activity of noble metals as compared to non-noble ones, typical for hydrogenation reactions, is tarnished by their high price. On the 28th October 2016, the price per ounce for purchasing platinum was 971 \$ versus 0.3 and 0.002 \$ for nickel and iron, respectively. The use of these two categories of metals in the industrial production of substituted anilines highlights the difficulty to establish the optimal trade-off. Latter is complex because it includes multiple interrelated parameters such as the activity, selectivity and the cost of the catalyst and high pressure installations.

Auer *et al.* from Degussa silver showed that among precious metals, Iridium doped by non-noble metals (0.1–0.3 wt.%) can be used as an alternative to Pt for the selective reduction

of halogenated nitro compounds. A high 2-chloroaniline yield (~99.9%) was reached over a Mn-Fe-doped Ir/C catalyst.¹⁸

Au and Ag-based catalysts

Gold- and silver-based catalysts now rarely mentioned as catalysts of choice for hydrogenations. It is not surprising that the first publications showing gold in 2006 being active during hydrogenation of nitroaromatics compounds created a sensation.^{19,20} Despite the selectivity being very high towards various products, harsh conditions are required to circumvent the low activity exhibited by gold catalysts.

Under optimized conditions (T = 413 K; P = 20 bar), dehalogenation was inhibited over a Ag/SiO₂ catalyst, affording the creation of various chloroanilines in quantitative yield. The selectivity decreased to 80% (X = 35.9%) at 377 K with the formation of nitrobenzene, demonstrating the extent of halogen bond rupture to be temperature dependent.²¹ For instance, *para*-chloronitrobenzene (*p*-CNB) was successfully converted into *para*-chloroaniline (*p*-CAN) (X = 100%; S = 100%) over Au/Al₂O₃ but under harsh conditions (T = 413 K; P = 40 bar) compared to Pt catalysts. However no dechlorination was observed.²²

Au 2–5 nm NPs supported on zirconia were shown to be effective (Y = 99.4%), providing excellent yield while ensuring the absence of any C-Cl bond hydrogenolysis.²³

Nickel-based catalysts

In comparison with cobalt or iron the use of nickel is far more prominent despite its higher toxicity. Interestingly, the first reported use of nickel for hydrogenating haloaromatic nitro compounds dates back in 1904 when Sabatier and Mailhe studied the direct reduction of halogenated aromatic compounds using fine nickel powder and hydrogen.²⁴ Starting the reaction with *ortho*- or *meta*-chloroanilines they rapidly observed the formation of aniline hydrochloride, adsorption of chlorine on the nickel surface and free aniline in the reaction

suspension. The dechlorination and amino group reduction occurred simultaneously when chloronitrobenzenes were used instead. Based on these findings Winans employed a Raney nickel catalyst to reduce several halogen-containing nitroarenes ($X = I, Br, Cl$).²⁵ He succeeded in avoiding mostly the dehalogenation during *p*-CNB reduction ($Y = 97\%$) by adjusting the reaction temperature and catalyst loading. His experimental procedure, as well as that of Sabatier, does not allow precise evaluation of the dechlorination reaction before and after completion of the nitro group reduction. Nevertheless, the morphological nature of nickel is likely to play a role in C-X bond cleavage.

Baumeister *et al.* resorted to the use of additives to the reaction medium rather than tailoring a standard or commercial catalyst. The addition of formamidine acetate (designated as a “N-modifier”) to a Raney nickel (RaNi) catalytic system suppressed the dehalogenation taking place after full reduction of the NO_2 group.²⁶ Furthermore, the time of reaction was greatly diminished. The hydrolysis of the modifier by water formed during hydrogenation entails the use of significant concentrations to ensure its effectiveness (~5% of the substrate). This system was considered as a benchmark catalyst for the hydrogenation of chloronitrobenzenes in the late 90s.

Many groups continued to devote their efforts to optimizing Raney nickel. After leaching out the aluminium, methane decomposition at high temperatures (673 K; 40 h) was applied to simultaneously generate carbon filaments and ~20 nm nickel nanoparticles.²⁷ In addition to their role of support, the filaments were claimed to stabilize the NPs metallic phase. 99%

p-CAN yield was obtained at a modest specific reaction rate ($8.43 \times 10^{-4} \text{ mol} \cdot \text{mol}_{Ni}^{-1} \cdot \text{s}^{-1}$ at 393 K vs the $1.43 \times 10^{-3} \text{ mol} \cdot \text{mol}_{Ni}^{-1} \cdot \text{s}^{-1}$ at 353 K of the benchmark mentioned above).

Softer methane decomposition conditions (668 K; 5 h) over RaNi lead to a catalyst stable in air without exhibiting pyrophoricity. Formation of a fine layer of oxides (Ni, Al)

covering the skeletal porous structure were used to explain the improvement in reaction rate and *p*-CAN yield (97 → 99 %) compared to standard Raney Ni.²⁸

Depositing nickel on different supports afforded nanoparticles with distinct morphologies and electronic properties.²⁹ During the hydrogenation of *o*-CNB, selectivities above 99% were obtained, irrespectively of the catalyst employed. The 6–50 nm NPs of the Ni/SiO₂ catalyst exhibited a turnover frequency (TOF) in the hydrogenation of *o*-CNB significantly lower (0.2 s⁻¹) than the ~22 and ~20 nm NPs of Ni/ZrO₂ (1.4 s⁻¹) and Ni/TiO₂ (34.9 s⁻¹), respectively. The differences in TOF, despite similar dispersion (D), confirmed the promotion effect by TiO₂ the support. Enhancement of catalytic performance through support interaction will be addressed in **section 2.3.1**.

The properties of TiO₂ (SSA, rutile/anatase phase ratio, pore volume, etc.) were modified after a calcination treatment (773–1173 K), performed prior impregnation by the Ni precursor.³⁰ The optimum TOF (2.4 s⁻¹) during the production of *o*-CAN was measured over the catalyst prepared with the support calcined at 973 K. The Ni-TiO₂ interactions were once more used to explain the variations in catalytic response. Moreover, the pre-treatment of TiO₂ does not affect the resulting TOF or specific reaction rate relative to an untreated support.

The same applies to the Ni/TiO₂ catalysts prepared using the sol-gel method. For similar *o*-CAN yields (~98%), the activity remained inferior to the catalyst prepared by incipient wetness impregnation (without any support pre-treatment). An advantage of this system is its stability, *i.e.* conversion and selectivity remained during 9 recycles.³¹ Overall, TiO₂-supported Ni catalysts were found to be more active than Raney nickel with or without additive. Compared to the 99.4% *o*-CAN yield obtained with Raney nickel in the presence of formamidine acetate, yields greater than 98% were achieved with the Ni/TiO₂ catalyst.

The use of carbonaceous supports generally allows greater dispersion (> 10%) to be obtained compared to TiO₂ but without benefiting from the interactions mentioned above. Thus, the reported turnover frequencies are significantly inferior and specific reaction rate do not approach the performance exhibited by benchmark catalysts. Ni nanoparticles (11 nm) supported on commercial carbon nanotubes (CNFs) were prepared by the deposition-precipitation method in ethylene glycol.³² In comparison, Ni/CNFs obtained by impregnation showed lower dispersion (0.7% vs 6.0%) and lower specific reaction rates (6.9×10^{-3} vs 1.5×10^{-2} mol_{o-CNB}·mol_{Ni}⁻¹·s⁻¹). The Ni/CNFs exhibited ~97% yield of *o*-CAN at 99% conversion.

Using the same preparation method with ethylene glycol, magnetically recoverable Ni NPs (9 nm) supported on carbon were prepared.³³ Specific rates of TiO₂-supported catalysts could only be attained at higher temperatures (413 K). The selectivity to chloroanilines (< 86%) being low, the prime advantage of the system is that it is too easy to handle.

In-situ catalytic chemical vapour deposition (CCVD) was used to produce NiC-Ni/CNFs. The presence of nickel carbide did not lead to a significant increase of the catalytic performance, with specific reaction rates, TOF and selectivities comparable to those reported for Ni/CNFs.³⁴

Beller *et al.* impregnated Vulcan XC72R with a Ni-1,10-phenanthroline complex and then pyrolysed it at a high temperature (1073 K).³⁵ The resulting catalyst is composed of 10–50 nm NiO-Ni⁰ NPs surrounded by N-doped graphene layers (Ni-NiO/NGr@C). Several functionalized anilines were produced selectively (69–99%) under moderate temperature and high pressure (T = 383 K; P = 50 bar). Besides the addition of triethylamine as additive (1:1 molar ratio with substrate), the reaction rate was 2 to 10 times lower than conventional RaNi catalysts for this type of reaction.

Iron-based catalysts

Aside from their role as supports for precious metal NPs,^{36,37} iron and cobalt were only very rarely reported as active catalysts for the synthesis of functionalized anilines, most often combined with carbonaceous supports. In addition, Fe₃O₄ powder (15–25 nm) prepared from α -Fe₂O₃ which was utilized for hydrogenating aromatic nitro compounds.³⁸ Although it exhibited the lowest catalytic activity relative to the other Fe-based catalysts, some interesting features were found. The descending order of activity measured over Fe₃O₄, FeO, γ -Fe₂O₃, and α -Fe₂O₃ was explained by higher concentration, on the surface of Fe₃O₄, of oxygen vacancies which favour the dissociation of H₂.

Beller *et al.* applied the same protocol used for the Ni-based catalysts, but with iron and cobalt.^{39,40} Large NPs (20–80 nm) surrounded by nitrogen-doped graphene layers (NGr@C) were obtained from appropriate precursor complexes. It should be noted that if the iron-based catalyst allows similar conversion as Ni-NiO/NGr@C, cobalt surprisingly exhibits an order of magnitude higher specific rates than the reference catalysts (RaNi + additive). The yields are comparable between the 3 systems, varying between 96 and 99% depending on the position of the Cl- group on the aromatic ring.

Cobalt-based catalysts

All of the Co-based catalysts reported to date involve the use of carbon as a support. Except for the catalyst developed by the Beller group, they show rates 3 to 500 times lower than the RaNi with additives with slightly inferior *o*-CAN yields (Y = 95-99%). Nitrogen-doped catalysts, such as N-doped carbon supported Co NPs (Co/CN-600)⁴¹ or Co-Co₃O₄ NPs deposited on N-doped carbon nanotubes,⁴² demonstrate higher activities than the N-free catalysts: carbon layers encapsulated Co⁰ NPs with portions of CoO_x,^{43,44} and Co/C microspheres.⁴⁵ Among the several ways nitrogen influences the active phase or the

carbonaceous support, the electronic influence at the metal-support interface seems the most plausible to explain the present catalytic promotion by nitrogen.⁴⁶

Summary

The main parameters of the catalysts mentioned above for their catalytic performance in the hydrogenation of chloronitrobenzenes are summarized in the following table (cf. **Table 2.1**).

Table 2.1. Summary of the latest catalytic systems reported for the hydrogenation of chloronitrobenzenes.

N°	Catalyst	d^d (nm)	P _{tot} /P _{H₂} / Solvent	T (K)	-R _{average} ^B (mol _p -CNB·mol _M ⁻¹ ·s ⁻¹)	X _p -CNB (%)	S _p -CAN (%)	Y _p -CAN (%)	Ref.
1 ^C	Pt/C	-	NA/12/ none	363	3.28	100	99.5	99.5	17
2 ^C	Mn-Fe-Ir/C	< 5	10/NA/ Toluene	363	6.0x10 ⁻¹	100	99.9	99.9	18
3	Ag/SiO ₂	5–15	NA/20/ EtOH	413	5.7x10 ⁻³	100	100	100	21
4	Au/Al ₂ O ₃	7–9	NA/40/ EtOH	413	5.8x10 ⁻²	100	100	100	22
5	Au/ZrO ₂	2–5	NA/40/ EtOH	423	2.3x10 ⁻²	100	99.4	99.4	23
6	RaNi	-	NA/100/ EtOH	373	3.8x10 ⁻³	-	-	97.0	25
8	RaNi+N- modifier ^D	-	NA/12/ MeOH	353	1.4x10 ⁻³	100	99.7	99.7	26
9	NiFC1	19	NA/15/ MeOH	393	8.4x10 ⁻⁴	100	99	99.0	27
10	NiC-3	-	NA/15/ MeOH	393	4.3x10 ⁻³	-	> 99	-	28
11	Ni/TiO ₂	20	15/NA/ EtOH	363	1.4x10 ⁻²	99.1	99.2	98.3	29
12	Ni/TiO ₂ (T773)	18	15/NA/ EtOH	353	1.4x10 ⁻³	> 98	> 98	96.0	30
13	Ni/TiO ₂ (SG- 673)	34	NA/10/ EtOH	348	3.0x10 ⁻³	> 98	> 99	> 97.0 ^E	31
14 ^C	Ni/CNFs	11	20/NA/ EtOH	413	3.3x10 ⁻³	99	98	97.0	32
15	Ni/C (magnetic)	5–15	20/NA/ EtOH	413	2.2x10 ⁻²	100	84.5	84.5	33
16	NiC-Ni/CNFs	20 ^F	NA/20/	413	3.0x10 ⁻³	100	99.5	99.5	34

2.1 Methodologies for the reduction of nitroaromatics

N°	Catalyst	d^A (nm)	P _{tot} /P _{H₂} / Solvent	T (K)	-R _{average} ^B (mol _{p-CNB} ·mol _M ⁻¹ ·s ⁻¹)	X _{p-CNB} (%)	S _{p-CAN} (%)	Y _{p-CAN} (%)	Ref.
			EtOH						
17 ^G	Ni- NiO/NGr@C	10–50	NA/50/ THF:H ₂ O (1:1)	383	6.9x10 ⁻⁴	-	-	99	35
18	Fe ₃ O ₄ powder	15–25	NA/30/ EtOH	423	1.7x10 ⁻⁵	90	100	90.0	38
18	Fe-phen/C-800	20–80	NA/50/ THF:H ₂ O (1:1)	393	5.1x10 ⁻⁴	100	96	96.0	39
21 ^G	Co-phen/C-800	20–80	NA/50/ THF:H ₂ O (1:1)	383	4.6x10 ⁻³	-	-	95	40
22 ^G	Co/C-N-600	9	NA/10/ MeOH	373	6.2x10 ⁻⁴	-	-	99.0	41
23	CoO _x @NCNTs	13	NA/30/ EtOH	383	1.7x10 ⁻³	100	99	99.0	42
24	Co@C	20–150	NA/10/ Toluene	413	3.6x10 ⁻⁵	99	97	96	43
25 ^G	Co/CoO@C	25 ^H	NA/30/ THF:H ₂ O (1:0.05)	393	7.0x10 ⁻⁴	-	-	97	44
28 ^C	Co/C(W+EG) 700	3.5	NA/20/ EtOH	413	1.8x10 ⁻³	98	97	95.1	45

^A The diameter d corresponds to the average diameter given in the references or the approximate observed range.

^B The average transformation rate was calculated with equation (3.4) for the reaction time required to reach the conversion associated the highest yield given in the references.

^C *o*-CNB was tested rather than *p*-CNB.

^D The N-modifier refers to formamidine acetate.

^E Based on available kinetic data, the yield could be higher.

^F Estimated from the TEM published images. The authors mentioned bigger NPs (40–60 nm) being present.

^G The average specific transformation rate was calculated assuming X = 100%.

^H From only 1 nanoparticle.

2.1.5.2 Nitrostyrene Hydrogenation

The development of catalysts for reducing C=C bond-containing nitroarenes has not received equal attention to halonitroarenes. C=C is an easily reducible functionality, and so, the selective reduction of the nitro group is challenging. The 1998 benchmark catalyst is a Pt-based catalyst supported by carbon with H₃PO₂ and VO(acac)₂ (or NH₄VO₃) designated as “modifiers”.⁴⁷ A *m*-vinylaniline (*m*-VA) yield of 95% was achieved using this system under moderate conditions (T = 373 K; P_{H₂} = 5 bar). The detailed mechanism and role of H₃PO₂ is

speculation. The behaviour of phosphorus based compounds was already described as involving their decomposition on the surface of catalysts during hydrogenation, thereby blocking some surface while leaving uncovered active atoms.⁴⁸ It has been hypothesized that reduction of C=C bonds involves adsorption on sites consisting of multiple atoms. Thus, the only mono-atom sites available favour the hydrogenation of -NO₂. As for *p*-chloronitrobenzene, Pt is found to be the most active for reducing *m*-nitrostyrene, by 10–1000 times, compared to the non-precious metal-based catalysts.

Rather than using additives for optimization of the selectivity, catalytic efficiency has been optimized by choosing appropriate support and preparation conditions. Most studies on platinum catalysts reported small nanoparticles as the active species, varying between a single atom and 5 nm. Yarulin *et al.* deposited platinum NPs (2.5 nm) on ZnO.⁴⁹ The selectivity improvement towards *m*-VA was obtained by setting the temperature during thermal activation at 573 K which led to the formation of Pt-Zn alloy. The strong metal-support interactions (SMSIs) were considered to facilitate the near-exclusive formation of *m*-VA.

Wei *et al.* went further in the downsizing of Pt nanoparticles by using FeO_x as a support, a very low metal loading (0.08%) and a lower temperature (473 K).⁵⁰ The high *m*-VA yield (95.1%) and TOF (0.42 s⁻¹) measured over the only present Pt single atoms were attributed to the strong interactions taking place between the Fe-based support and active metal.

Gold was found to be an active metal in the reduction of aromatic nitro compounds in the mid-2000s.¹⁹ Nitrostyrene was hydrogenated successfully ($Y_{m-VA} = 95\%$) without any use of reaction modifier. The 3.8 nm Au NPs competed with the Pt/C-H₃PO₂-VO(acac)₂ system, most likely because the (unspecified) dispersion of the latter was lower or that, as the authors speculated, the high selectivity is obtained by means of isolated atoms at the expense of lost parts of the surface. The 2.5 nm Pt crystallites supported on ZnO mentioned earlier⁴⁹ were significantly more active in comparison.

Non-noble transition metals, like Co and Fe, were successfully used for producing vinylaniline (VA) from nitrostyrene (NS). For instance, the N-doped carbon supported Co NPs (Co/CN-600) also protected the C=C bond in *p*-NS ($Y = 96$).⁴¹ Carbon was used as support and nitrogen was often incorporated during the catalyst preparation, to achieve high efficiency. A catalyst developed by Chen *et al.* was an exception regarding the use of nitrogen to boost the catalytic potential.⁴⁴ A 95% *m*-VA yield was obtained using the Co/CoO_x NPs covered by graphene layers acting as a protective coating. An equivalent performance was attained with cobalt supported on carbon nanotubes doped with nitrogen, while the Co-1,10-Phenanthroline/C catalyst gave a *m*-VA yield only of 91%.⁴⁰ Its Fe equivalent afforded *m*-VA with a yield of 96%.³⁹ In spite of the fact that multiple parameters vary from one study to another (solvent, temperature, pressure, etc.), it seems that the exclusive conversion to vinylaniline does not depend on the Fe active phase dispersion as the nanoparticle diameter in all the mentioned studies ranged from 9 to 50 nm.

Summary

The main parameters of the catalysts mentioned above for their catalytic performance in the hydrogenation of nitrostyrenes are summarized in the following table (cf. **Table 2.2**).

Table 2.2. Summary of the latest catalytic systems reported for the hydrogenation of nitrostyrenes.

N°	Catalyst	d^A (nm)	P _{tot} /P _{H2} / Solvent	T (K)	-R _{average} ^B (mol _m -NS·mol ⁻¹ ·s ⁻¹)	X _{m-NS} (%)	S _{m-VA} (%)	Y _{m-VA} (%)	Ref.
1	Pt/C-H ₃ PO ₂ - [VO(acac) ₂]	-	NA/5/ Toluene	373	-	100	95	95	47
2	Pt/ZnO	2.5	NA/10/ MeOH	348	2.1x10 ⁻¹	100	98	98.0	49
3	Pt/FeO _x (R250)	Single atom	3/NA/ Toluene	313	4.0x10 ⁻¹	96.5	98.6	95.1	50
4	Au/TiO ₂	3.8	NA/9/ Toluene	393	2.0x10 ⁻²	98.5	95.9	94.5	19
5	Fe-phen/C-800	20–80	NA/50/ THF:H ₂ O (1:1)	393	4.6x10 ⁻³	-	-	96	39

N°	Catalyst	d^A (nm)	P _{tot} /P _{H₂} / Solvent	T (K)	-R _{average} ^B (mol _{m-NS} ·mol _M ⁻¹ ·s ⁻¹)	X _{m-NS} (%)	S _{m-VA} (%)	Y _{m-VA} (%)	Ref.
6	Co-phen/C-800	20–80	NA/50/ THF:H ₂ O (1:1)	383	^C 3.9x10 ⁻⁴	-	-	91	40
7 ^D	Co/C-N-600	9	NA/10/ MeOH	373	6.1x10 ⁻⁴	99	97	96.0	41
8	Co/CoO@C	25 ^E	NA/30/ THF:H ₂ O (1:0.05)	393	^C 7.0x10 ⁻⁴	-	-	95	44

^A The diameter d corresponds to the average diameter given in the references or the approximate observed range.

^B The average transformation rate was calculated with equation (3.4) for the reaction time required to reach the conversion associated the highest yield given in the references.

^C The average specific transformation rate was calculated assuming $X = 100\%$.

^D *p*-NS was tested rather than *m*-NS.

^E From only 1 nanoparticle.

2.1.6 Catalytic Transfer hydrogenation (CTH) of nitroarenes

An alternative to molecular hydrogen is the use of organic molecules able to donate hydrogen to the substrate to be reduced, referred as transfer hydrogenation and was already reported at the beginning of the 20th century by Knoevenagel and Bergdolt.⁵¹ In presence of palladium black, dimethyl-1,4-dihydroterephthalate disproportionates into dimethyl terephthalate and *cis*-hexahydroterephthalate. This process corresponds to the second type of hydrogen transfer according to Braude and Linstead classification.⁵² The first and third types correspond to the migration of hydrogen occurring within the same molecule and the transfer between two different molecules (a donor and an acceptor), respectively. Transfer hydrogenation can be categorized depending on the means employed to achieve the reaction, *i.e.* by heating, photochemically, using homogeneous or heterogeneous catalysts.

Herein we will focus catalytic transfer hydrogenation (CTH) relying on heterogeneous catalysts. The production level based on CTH is incommensurable compared to catalytic hydrogenation which represents 10–20% of the reactions used to produce chemicals.¹² The reasons why CTH presence in industry is marginal were addressed by Johnstone et al in his 1985 review.⁵³ He mentions the inconclusive results first reported, in particular by Braude,

and the high efficiency of processes based on molecular hydrogen successfully run at the same time. The advantages of this method indeed exist. The absence of gas igniting easily avoids the risk of explosion and allows the use of equipment much less sophisticated. Sanfilippo described hydrogenation and dehydrogenation catalytic processes in which higher yields can be reached using CTH.⁵⁴ Unsurprisingly, a significant number of studies involving heterogeneous catalytic transfer hydrogenation have been conducted in the last two decades¹.

When looking specifically into the CTH of nitroarenes, hydrazine and cyclohexane are among the few hydrogen donors that are suitable. Hydrazine is compatible with various metal catalysts and substrates in the production of aminoarenes. Commonly handled in its hydrated form ($\text{N}_2\text{H}_4 \cdot \text{H}_2\text{O}$), because it is toxic and unstable in its pure state. Hydrazine is already used in industrial processes for the production of plastic foams, polymerization initiators, pesticides and pharmaceuticals.⁵⁵ Formic acid⁵⁶⁻⁵⁹ and 2-propanol⁶⁰⁻⁶⁶ are also used for CTH and were employed successfully in many different reactions.

2.1.6.1 Chloronitrobenzene reduction

Previously we have seen the minor role of non-noble metals in the hydrogenation of nitroarenes using molecular hydrogen. The situation is different in CTH because the mechanism is completely different. Thus, the high catalytic potential of iron has been rapidly demonstrated. Hirashima *et al.* proposed a reaction system including hydrazine hydrate as a reducing agent, Fe(III) chloride and activated carbon.⁶⁷ The majority of the tested nitroaromatic compounds were transformed into the corresponding anilines in excellent yield (> 90%) under mild conditions ($T = 353 \text{ K}$; $P = 1 \text{ bar}$). Later, Lauwiner *et al.* used $\text{Fe}_3\text{HO}_8 \cdot 4\text{H}_2\text{O}$ (ferrihydrite) derived from FeCl_3 to reduce nitroarenes.⁶⁸ Among the almost 40

¹ 471 found when searching in <https://webofknowledge.com/> with the terms “heterogeneous”, “catalytic” and “transfer hydrogenation” as topic fields. (30.12.2016)

tested substrates, *p*-CNB isolated yield of 98% was achieved without any sign of dehalogenation.

The novelties introduced later by the new systems most often concern practical aspects. Based on a $\text{Fe}_3\text{HO}_8 \cdot 4\text{H}_2\text{O}$ catalyst, Shi *et al.* proposed polymer-supported hydrazine hydrate for the reduction of nitroarenes to avoid any excess of the reducing reagent in the liquid phase. A *p*-chloroaniline yield of 99% was obtained.⁶³

To facilitate the ulterior separation, Kim *et al.* tested colloidal superparamagnetic Fe_3O_4 nanoparticles (Sigma Aldrich, < 50 nm) with hydrazine as a reducing agent. With the exception of the ethyl acrylate functionality, all other nitroarenes including *p*-CNB were hydrogenated in excellent yield (99%).⁶⁹

The same concept was applied by Cantillo *et al.* using iron oxide nanocrystals generated *in-situ*.⁷⁰ The functionalized nitroarene, hydrazine hydrate, iron oxide precursor ($\text{Fe}(\text{acac})_3$) and EtOH as a solvent were heated in a microwave oven. Fast (< 8 min) and efficient reduction of nitroarenes ($Y_{p\text{-CAN}} = 99\%$) has been obtained. Cobalt was used in the CTH of *p*-CNB in the form of complexes^{71,72} or salt.^{73,74}

(110) planes in CeO_2 nanorods (~10 x 150 nm) were found to selectively convert various nitroaromatics with hydrazine hydrate as reducing agent under mild conditions, and the yield of halonitrobenzenes was modest (*e.g.* $Y_{p\text{-CAN}} = 76\%$).⁷⁵

2.1.6.2 Nitrostyrene reduction

A limited number of studies focusing on the CTH of nitroarenes include nitrostyrene in their reaction scope. Except for a few papers using noble metals such as ruthenium,⁷⁶ most rely on catalysts based on Cu, Co or Fe.

Over a catalytic system consisting in Cu NPs stabilized by ionic liquid (imidazolium) with ammonium formate as hydrogen donor, a modest *p*-VA yield of 84% was achieved.⁷⁷ Beller *et al.* used heterogeneous catalysts prepared from Fe or Co complexes. The Fe catalyst

was reported before the two papers published in 2013.^{39,40} Regardless of the metal used the formulation to prepare the catalyst was systematically applied, *i.e.* carbon black (Vulcan XC72R) is impregnated by a $M(\text{OAc})_2$ -1,10-phenanthroline complex and subsequently pyrolyzed at 1073 K for 2 hours.⁷⁸ A 96% yield of *m*-VA was obtained with hydrazine (4 equivalents) as hydrogen source. At that time there was no mention of the supposed role of nitrogen from phenanthroline on the catalytic performance. With the cobalt version of this catalyst *m*-NS was converted less selectively into *m*-VA ($Y_{m\text{-VA}} = 93\%$) employing formic acid-triethylamine ($\text{HCOOH-Et}_3\text{N}$) as the reducing agent rather than hydrazine hydrate.⁵⁷ Except for 2,6-methyl-3-nitropyridine, all the ten common substrates among the two scopes paper have been converted in higher yield over the Fe-based catalyst. Interestingly, the latter catalyst was tested a few years later with the $\text{HCOOH-Et}_3\text{N}$ complex.⁵⁸ Lower yields were obtained for the 8 common substrates compared to when hydrazine was used as H-donor, indicating that the choice of reducing agent played a crucial role, to a greater extent than the catalyst metal (Fe or Co). Additionally, higher reaction times (~ 2 X), the amount of active phase (5 X) and temperature (393 K instead of 373 K) were required with the $\text{HCOOH-Et}_3\text{N}$ complex rather than hydrazine hydrate. However, it should be noted that despite triethylamine having safety disadvantages (flammable, acutely toxic and corrosive) of the same order as hydrazine hydrate, only corrosive dangers are linked to the complex formed with formic acid.

2.2 Structured supports for catalytic applications

2.2.1 Types of structured supports

Industrial catalysts are mostly supported in order to offer the required dispersion and properties to the active phase while ensuring its stability, in particular by minimizing sintering and aggregation phenomena. They are manufactured in different shapes in the form of pellets

to meet the reaction conditions specific to each process. Once randomly arranged in packed beds within the reactors, batch or continuous reactions the void fraction is roughly 0.5. Optimum performance can be limited by pressure losses, heat transfer and maldistributions, inherent to the morphology of the pellets and random packing. A higher void fraction (0.7 to 0.9) and degree of organization diminish these limitations,⁷⁹ and can be obtained over structured catalysts. Catalytic hydrogenation of substituted nitro aromatic compounds performed over monolith,⁸⁰ foams^{81,82} and fibres^{83,84} have been reported. The following paragraph give an overview of the general characteristics of each type of structured catalyst.

Monoliths

Reminiscent of a honeycomb, monoliths are made up of parallel channels that can adopt various forms (circular, square, hexagonal, etc.). The catalytic active phase is present within a thin layer (washcoat) deposited on the reactor walls. The open structure area ensures lower pressure drop and minimized external transport limitations relative to conventional powder catalysts. Furthermore, monoliths benefit from high specific surface areas, low axial dispersions and their scale-up is simple to achieve. Low radial heat transfer, non-uniform fluid distribution and high price are disadvantages.⁸⁵

Foams

Catalytic foams consist of interconnected cells defined by solid edges which provide a high degree of porosity. Despite the greater extent of randomness with respect to monoliths, low pressure drops are observed while exhibiting excellent radial heat transfer properties.^{86,87}

Fibres

Similarly to monolith or foams, fibrous catalysts are designed to have open macrostructures which guarantee reduced pressure drops. In contrast to other structured catalysts, they possess flexible structures facilitating handling. Depending on the reaction or

active phase morphological requirements, metal, glass or carbon fibres are employed as supports. If the diameter of a single fibre is 5–20 μm the internal mass transfer limitations can be avoided.

2.2.2 Activated carbon fibres (ACFs) as supports

Carbon nanofibers (CNFs) and activated carbon fibres (ACFs) are typical examples of structured carbon supports. The former have a graphitic mesoporous nature characterized by diameters and lengths in the range of 10–100 nm and 0.1–1000 μm , respectively. The specific surface areas range from 10 to 200 m^2/g . The high production cost of CNFs restricts their use in large scale applications.^{88,89}

Activated carbon fibres (ACFs) possess similar intrinsic characteristics of activated carbon (AC) while having a 3D open macrostructure which provides enhanced fluid permeability. As for AC, the macro-, meso- and micropores distribution defining the porous structure is highly dependent on the choice of raw material and physical-chemical treatment.⁹⁰ ACFs are characterized by higher specific surface areas (1000–3000 $\text{m}^2\cdot\text{g}^{-1}$) and narrower pore distributions compared to AC.

High rates of adsorption from the gas and liquid phases are enabled in ACFs due to the network arrangement: slit-shaped micropores (< 2 nm) are directly connected to the external surface.^{91,92}

2.2.3 ACFs surface modifications

The slightly acidic nature of activated carbon or ACFs is linked to the concentration and types of surface functional groups which can be modified by various chemical or physical treatments. For instance, oxidative treatments increase the number of surface oxides.⁹³ The phase in which the treatment is carried out determines the type of groups created. Creation of

carboxylic acid groups is favoured in the liquid phase while hydroxyl and carbonyl groups are mostly generated in the gas phase. The contribution to the surface acidity varies for each group, *e.g.* carboxyl groups are strongly acidic while the phenolic groups are weakly acidic (cf. **Figure 2.2**).⁹⁴

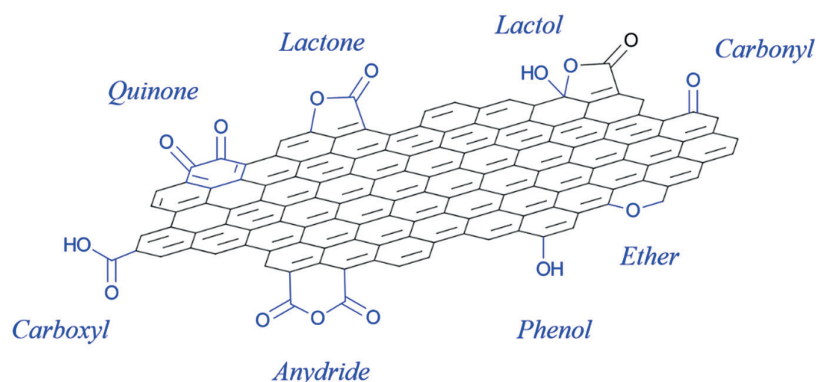


Figure 2.2. Surface oxygen-containing groups on carbon.

It is well known that oxygen-containing groups act as hydrophilic sites on the carbonaceous surface, greatly affect the adsorption capacity towards adsorbates in the gas-phase. In the field of catalysis, such surface modifications have been shown to improve the Pt dispersion by facilitating the access of the precursor to micropores during the impregnation step due to lowered hydrophobicity (strong acid groups) and decreasing sintering during the reduction step by increasing surface-precursor interactions (weak acid groups).^{95,96} A striking example of surface modifications leading to improved activity introduced by Nieto-Márquez *et al.* for the hydrogenation of nitrobenzene. Ni NPs supported on CNFs, carbon nanospheres (CNSs) or AC, all pre-treated with HNO₃ and H₂SO₄, demonstrated a proportional increase in activity with respect to the surface acidity. Size-effects were ruled out.⁹⁷ Similar effects were observed in the transformation of *p*-CNB to *p*-CAN using Pd NPs supported on oxidized carbon nanotubes (CNTs).⁹⁸

2.3 Catalyst Optimization for Hydrogenation Reactions

2.3.1 Role of the Support in Catalytic Hydrogenation (catalyst promotion)

The support for catalytic active phases should allow the appropriate dispersion and ensure catalyst stability by avoiding agglomeration or leaching phenomena. The structure is essential in order to prevent transport influence on the reaction rate. Beyond its primary roles, supports sometimes influences the catalytic active phase. The electronic properties of the metallic phase may be modified due to interactions with the support known as strong metal-support interactions (SMSIs).

In some cases, the catalytic action is due to the sites located at the interface with the support. The influence of the support on the catalysis may also be designated as geometrical since the orientation of the substrate during the adsorption is conditioned by the space formed at the metal-support edge.

TiO₂ is undoubtedly the best known example of support which can lead to SMSIs influencing the catalytic response.⁹⁹ Tauster *et al.* demonstrated that by increasing the reduction temperature from 473 to 773 K of Pt/TiO₂, the adsorption of hydrogen or CO on Pt could be hindered. They explained this phenomenon by the creation of bonds between Pt and TiO₂, hence forming TiPt₃ species, which cannot form on non-reducible metal oxides such as SiO₂ or Al₂O₃.¹⁰⁰

Later, it was specified that a strong increase in the interfacial area takes place in parallel with the creation of the new phase. This type of catalyst whose structure and electronic properties have been altered is no longer described as consisting of a support and an active phase and the term “fused catalyst” is used.

SMSIs do not necessarily require the creation of a new phase. In the context of the hydrogenation of *m*-nitrostyrene, Boronat *et al.* showed that SMSIs were present between the TiO₂ support and the gold nanoparticles.¹⁰¹ The sites responsible for the selective formation of

m-vinylaniline were located at the interface leading to the conclusion of simultaneous electronic and geometric contributions on the catalytic response.

Carbonaceous supports do not induce SMSIs in catalysts, but such systems are not completely devoid of interactions, which are weak in the absence of surface functional groups. Based on a model system comprising one to three Ni (111) layers deposited on top of a graphite layer the density of states (DOS) for each scenario (1, 2 or 3 layers) at the contact point with the next layer was calculated.¹⁰² Beyond two Ni layers, no noticeable difference in the density of states could be appreciated with and without the graphite layer. The fraction of surface atoms influenced by the support as a function of the dispersion was finally estimated. For instance, when the NP diameter is 2 nm ($D = 50.6\%$) this fraction varies between 4 and 22% depending on the form of the particle tested, *i.e.* spherical or hemispherical. Due to the localized nature of the electronic influence in carbonaceous supports, effects on the metallic electronic properties and consequently the catalytic response are significant only when the particles are small.

Previously, it was shown that the properties of carbon can be modified by chemical treatments that results in the creation of groups containing atoms like oxygen, nitrogen and hydrogen. The activity and selectivity can be indirectly affected by these groups because of their influence on the metal precursor-carbon surface interactions, during the catalyst preparation, and *de facto* on the NPs size distribution. Their direct influence on catalytic performance during the reaction was also reported.

A very early example of catalysed reaction influenced by treating the carbon support was reported by Derbyshire *et al.* The oxidation of carbon black and carbon derived from polymer used for supporting a MoS₂ phase increased and decreased the catalytic activity in the hydrogenation of coal asphaltene, respectively.¹⁰³ An indirect influence was suggested where the treatment would create or destroy sites having a chemical affinity with the metal

precursor, consequently favouring higher or lower dispersion compared to non-treated supports. Shortly after, the study of Pt/C catalysts with varying amount of oxygen-containing groups showed that they influenced both the dispersion and resistance to sintering (in H₂).⁹⁶ More recently, the adjustment of AC chemical composition by oxidative and thermal treatment resulted in different sizes of Pd NPs (< 3 to > 20 nm) using atomic layer deposition (ALD). Size effects (antipathetic) were observed in the hydrogenation of nitrobenzene with the < 3 nm, 4–5 nm and > 6 nm particles and attributed to steric restrictions inside the AC pores.¹⁰⁴

The partial removal of oxygen containing groups on the CNF surface by thermal treatment at 973 K, with an accompanying decrease of polarity, enhanced by 25-fold the initial specific activity in the hydrogenation of cinnamaldehyde with Pt NPs compared to non-treated CNF. Modification of the substrate mode of adsorption was proposed for explaining these results.¹⁰⁵ Gold nanoparticles of the same size and similar appearance were generated on AC, treated at different temperatures to remove the surface groups. The catalyst with the least surface oxygen exhibited the highest activity without any significant effect on the selectivity. The enhancement was explained by the greater mobility of π -electrons on the carbon surface which could increase the electron density of the Au NPs.¹⁰⁶ The parameter of surface functional groups was also varied in vanadium oxide catalysts supported on CNTs used in the gas-phase catalytic reduction of NO with ammonia. Very interestingly, surface carboxyl groups in presence of SO₂ or hydroxyl groups alone were capable of changing the valence state of vanadium from which in turn favoured enhanced conversions.¹⁰⁷ HNO₃ or HCl treatments were performed to modify the surface chemistry of AC using as support for Ni catalysts. The addition of carboxyl and lactone due to HNO₃ treatment favoured monodispersed NPs and enhanced the redox cycle during N₂O reduction by increasing the adsorption of the Ni precursor.¹⁰⁸ A dual action of surface groups was also observed in the

gas-phase hydrogenation of nitrobenzene over Ni particles deposited on carbon-based supports. An activity boost was observed during the reaction after the pre-oxidation of CNFs, CNSs or AC supports with nitric acid. It should be noted that no change of dispersion was observed with the chemical treatment. Keane *et al.* explained that the catalytic activity rise was attributable to the increase in surface acidity, while specifying that the acid groups worked as an anchoring sites for the nickel precursors.⁹⁷

In summary, the modifications of the surface of carbon supports can lead to different effects, impacting the dispersion or even the catalysis itself which tends to complicate the results interpretation. It is not surprising to find so many different interpretations given the many parameters that can be impacted simultaneously by these treatments.

2.3.2 Effect of Metal Particle Size on Catalyst Performance

Several types of reaction rates are commonly used to quantify the activity of a catalyst: the moles of substrate converted per unit of time per unit of active metal (specific rate) or the number of catalytic cycles per active site (turnover frequency, abbreviated TOF).¹⁰⁹ The latter is preferable because it allows the best comparison of two different catalytic materials irrespective of their nature under the conditions employed. It is also the most arduous to establish because the determination of what constitutes an active site is not straightforward. It is not surprising that most studies present TOF where a surface atom corresponds to an active site. However, since it is possible to measure rates in moles of substrate per active metal surface (rather than referred to total quantity of metal), the size effects on the TOF can be determined. These reactions are referred to as “structure sensitive”, specifically sympathetic or antipathetic if the TOF decreases or increases with particle size, respectively. One of the first reasons for this phenomenon is the variation in proportions of atoms of different types as a function of size. For instance, three types of surface atoms are present when considering a

cubic particle, *i.e.* the atoms at the vertices, edges and faces. As the level of coordination varies among the latter, resulting in different reactivities with respect to the substrates it is clear that the TOF may vary according to the size.

Hardeveld and Hartog have determined for several structures of nanoparticles the variation with sizes of the different types of surface atoms,¹¹⁰ each type having a distinct coordination number. Except for studies where crystallites are meticulously generated in ultrahigh vacuum on model surfaces, those produced by the usual preparation methods contain almost systematically various types of defects on their surface. Beyond the factor of preparation conditions, it is statistically likely that within a large set of NPs most will not have the required number of atoms, values that are discrete, to be regularly shaped. For instance, an octahedron-shaped nanoparticle with, 2, 3 or 4 atoms lying on an equivalent edge (vertex atoms included), should have precisely 6, 19 and 44 atoms to have the probability of being well defined. For each of the structures previously considered, they reiterated their calculations but this time with a greater number of types of surface atoms, in order to take into account these defects and get closer to the catalysts used under real conditions. **Figure 2.3** shows, *e.g.*, the fraction variation of a type of edge atom (one is shown in red on the NPs) with particle size, depending on whether the ideal or non-ideal (with additional surface atoms, shown in dark grey) statistics were applied. The addition of atoms on a regularly shaped crystallite results in the modification of the surface atoms fractions and the creation of new types of surface atoms (with different coordination number). The established statistics have been extensively used since they provides a good basis for identifying some types of atoms that exhibit higher activities. For instance, the structure sensitivity of alkynol hydrogenation over Pd NPs was successfully studied using these statistics of surface atoms. The high degree of uniformity of each set of studied NPs (cubic, octahedral, and cuboctahedral) was a strong asset for linking the catalytic results (activity and selectivity) to given types of surface atoms.

Regarding this aspect, Bond and Thompson noted that Hardeveld and Hartog statistics are inadequate when the NPs analysed are too distributed in size because the number of surface atoms with a given coordination number varies significantly with size.¹¹¹

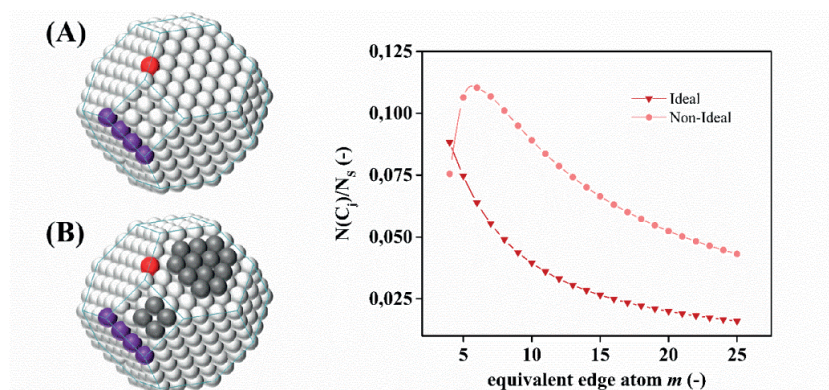


Figure 2.3. Variation of a type of edge atoms (in red on the NP) fraction as a function of NP size (calculated with the equivalent edge atoms m , in purple) with (A) ideal statistics or (B) non-ideal statistics.

The dependence on the structure of a reaction was mentioned above to be related to the variation of each type of atoms fraction with the NPs size. Each type of surface atoms is characterized by a coordination number and an electronic structure, which differ from that of the other types. Therefore, the surface interaction between a reactant and a nanoparticle may vary depending on the type of atom on which it adsorbs and an increase or decrease in crystallite size will affect the turnover frequency.¹¹² These size-effects are said to be induced by electronic effects. In contrast to electronic factors leading to structure-sensitivity, geometric effects have also been shown in catalysed reactions to influence the TOF. Groups of atoms on the NPs surface, rather than single atoms, play the role of active sites, the prevalence of which would depend on the NP size. These two types of factor inducing size effects have been theorized in order to facilitate the interpretation of structure-sensitive reactions but their actual interdependence must be underlined and only their relative contribution varies from case to case.

Chapter 3

Experimental

The present chapter describes the procedures used to prepare the catalysts and test them, with the most important experimental data being summarized in **Table 3.1**. The characterization techniques employed throughout this work and associated details are presented. Finally, the details of the recurring calculations are given in an analytical part.

3.1 Preparation of catalysts

All the gases (Ar, He, N₂, H₂, 10% v/v H₂/He) (> 99.99%) used during the preparation of the catalysts were purchased from Carbagas Switzerland.

3.1.1 Unsupported Ni, Au and Ni-Au NPs

Materials

Nickel (II) sulfate hexahydrate (Fluka, ≥ 98.0%), Sodium tetrachloroaurate(III) dihydrate (Sigma-Aldrich, 99.9%), polyvinylpyrrolidone (PVP, Mw = 10'000/29'000, Sigma-Aldrich), ethylene glycol (Sigma-Aldrich, 99.8%), sodium hydroxide (Sigma-Aldrich, ≥ 98.0%), sodium borohydride (Sigma-Aldrich, ≥ 96.0%), hydrazine (Sigma-Aldrich, 1 M in THF), tetraethylene glycol (Sigma-Aldrich, 99.0%), hydrogen peroxide (Reactolab SA, 30%) and ethanol (EtOH, Sigma-Aldrich, 99.8%) were used as received.

Procedure

3.1.1.1 2 nm Ni NPs (Ni2)

NiSO₄·6H₂O (0.053 g, 0.20 mmol) was dissolved in ethylene glycol (100 cm³) and PVP (0.22 g, Mw = 10'000) was added. The mixture was stirred for 15 min and cooled to 273 K. NaOH (1 M in MiliQ, 5 cm³) was added and the resulting solution was stirred for 90 min at 413 K. Acetone (1000 cm³, 10:1 relative to the ethylene glycol) was used to precipitate the NPs (max. 240 min). After precipitation of the NPs, the supernatant was decanted and the remaining suspension was centrifuged. Following removal of the solvent layer the precipitate was re-dispersed in EtOH (15 cm³).

3.1.1.2 4 nm Ni NPs (Ni4)

NiSO₄·6H₂O (0.26 g, 0.99 mmol) was dissolved in ethylene glycol (50 cm³) and PVP (2.2 g, Mw = 29'000) was added. Freshly dissolved NaBH₄ in water (0.53 M in MiliQ, 5 cm³) was added, leading to instantaneous particle nucleation (indicated by a change of color to black/brown). Then, the solution was stirred for 240 min at 293 K. Acetone (500 cm³, 10:1 relative to the ethylene glycol) was used to precipitate the NPs (max. 240 min). After precipitation of the NPs, the supernatant was decanted and the remaining suspension was centrifuged. Following removal of the solvent layer the precipitate was re-dispersed in EtOH (15 cm³).

3.1.1.3 11 nm Ni NPs (Ni11)

NiSO₄·6H₂O (0.26 g, 0.99 mmol) was dissolved in ethylene glycol (120 cm³). PVP (2.2 g, Mw = 29'000), NaOH (1 M in MiliQ, 4 cm³) and hydrazine hydrate (1 M in MiliQ, 2 cm³) were added. The solution was then brought to reflux for 240 min. Acetone (1000 cm³, 10:1 relative to the ethylene glycol) was used to precipitate the NPs (max. 240 min). After precipitation of the NPs, the supernatant was decanted and the remaining suspension was

centrifuged. Following removal of the solvent layer the precipitate was re-dispersed in EtOH (15 cm³).

3.1.1.4 14 nm Ni NPs (Ni14)

NiSO₄·6H₂O (0.26 g, 0.99 mmol) was dissolved in tetra-ethyleneglycol (120 cm³). PVP (2.2 g, Mw = 29'000) and NaOH (1 M, 5 cm³) were added to that solution which was finally brought to reflux for 240 min. Acetone (1000 cm³, 10:1 relative to the tetra-ethylene glycol) was used to precipitate the NPs (max. 240 min). After precipitation of the NPs, the supernatant was decanted and the remaining suspension was centrifuged. Following removal of the solvent layer the precipitate was re-dispersed in EtOH (15 cm³).

3.1.1.5 7 nm Au NPs (Au7)

NaAuCl₄·2H₂O (0.010 g, 0.025 mmol) was dissolved in water (MiliQ, 5 cm³) and combined with PVP (0.010 g, 0.0875 mmol) dissolved in ethylene glycol (90 cm³). The mixture was stirred for 120 min at 353 K and cooled down to 273 K. and the pH was adjusted to *ca.* 9 by adding NaOH (1 M in MiliQ water, 5 cm³). The mixture was then stirred for 90 min at 373 K, yielding a crude NP dispersion. Acetone (1000 cm³, 10:1 relative to the ethylene glycol) was used to precipitate the NPs (max. 240 min). The supernatant was decanted and the remaining suspension was centrifuged. Following removal of the solvent layer the precipitate was re-dispersed in EtOH (15 cm³).

3.1.1.6 3 nm Ni-Au NPs (Ni-Au)

NaAuCl₄·2H₂O (0.08 g, 0.20 mmol), NiSO₄·6H₂O (0.05 g, 0.20 mmol) and PVP (Mw = 10000, 0.222 g,) were dissolved in ethanol (150 cm³). The mixture was stirred for 60 min at 293 K. Freshly dissolved NaBH₄ in EtOH (0.12 M, 10 cm³) was added, leading to the instantaneous particle nucleation (indicated by a change of color to black/brown). The solution was stirred for a further 2 h. Acetone (500 cm³, 10:1 relative to the ethylene glycol)

was used to precipitate (max. 240 min) the NPs. Following precipitation of the NPs, the supernatant was decanted and the remaining suspension was centrifuged. Following removal of the solvent layer the precipitate was collected and washed twice with hexane:EtOH (1:1, 10 cm³) then water (MiliQ, 3X 10 cm³) and finally re-dispersed in EtOH (15 cm³).

3.1.2 Preparation of Structured ACFs-based Catalysts

All supported catalysts were prepared using activated carbon fibres (ACFs) purchased from Kynol Europa GmbH. They are produced from novoloid phenolic precursor fibres by a one step process combining carbonization and chemical activation. They were employed for supporting Fe, Co and Ni oxide NPs (**Section 3.1.2.1**) and metallic Ni NPs (**Section 3.1.2.3**) using the incipient wetness impregnation. **Section 3.1.2.2** describes the steps performed for supporting Ni, Au and Ni-Au NPs prepared in liquid-phase.

3.1.2.1 MO_x/ACF (M = Fe, Co, Ni) catalysts for CTH

Materials

Fe(III) nitrate nonahydrate (> 98%, Fluka), Co(II) nitrate hexahydrate (> 99%, Acros), Ni(II) nitrate hexahydrate (> 98%, Fluka) and nitric acid (VWR chemicals, 65%) were used as precursors in the catalysts preparation.

Procedure

The incipient wetness impregnation method was first applied. ACFs were immersed into an ethanol solution of Fe(NO₃)₃·9H₂O, Co(NO₃)₂·6H₂O or Ni(NO₃)₂·6H₂O to ensure a homogeneous filling of the pores. The excess of the solution was removed and impregnated fibres were then dried in air at room temperature (RT) over-night. Prior to impregnation, some ACFs were pre-treated in a 15 wt.% HNO₃ aq. solution at 373 K for 15 min in order to increase the concentration of oxygen-containing groups on the carbon surface.^{93,113} The

excess of nitric acid was removed by washing the supports with water (2X). The catalysts prepared from these pre-treated supports are referred as $\text{MO}_x/\text{ACF}_{\text{HNO}_3}$. The concentration of a precursor solution was adjusted to reach a desired metal loading. Thermal treatment of the impregnated ACFs was performed in a horizontally fixed tubular quartz reactor (50 cm x 3 cm i.d.) at 623 K (temperature ramp - $6 \text{ K}\cdot\text{min}^{-1}$) in an Ar flow ($280 \text{ cm}^3\cdot\text{min}^{-1}$) for 1 h. The oven was then cooled to room temperature. The resulting pyrophoric MO_x/ACF materials were passivated by an exposure to a 2.8% v/v air/Ar flow ($145 \text{ cm}^3\cdot\text{min}^{-1}$) for 1 h. Gas flows were controlled using an *Agilent Technologies* ADM1000 Universal Gas Flowmeter, values are given in IUPAC STP.

The desired metal loadings of the MO_x/ACF catalysts were reached by adjusting the precursor concentration in the impregnation solutions (step 1). The chemical composition of the catalysts was confirmed by atomic absorption spectroscopy (AAS).

3.1.2.2 ACFs-supported Ni and Ni-Au NPs for hydrogenations with H_2

Materials

Ethanol (EtOH, Sigma-Aldrich, 99.8%) and nitric acid (VWR chemicals, 65%) were used as received.

Procedure

Supported catalysts were prepared by deposition (impregnation) of the Ni and Ni-Au NPs on a structured support of activated carbon fibres (ACFs). Prior to deposition, the ACFs were activated in 15% nitric acid (20 min, 363 K) to increase the surface concentration of oxygen-containing groups. Treated ACFs were impregnated with an ethanolic suspension containing the appropriate NPs (0.03 g of ACFs were impregnated by 0.7 cm^3 of 0.01 M Ni, Au or Ni-Au NPs solutions) and then dried for 2 h. Next, the Ni/ACF and Ni-Au/ACF were subjected to either a UV-ozone (UVO) or thermal treatment to remove the PVP stabilizer. For

PVP removal by UVO the catalyst was placed for 4 h under an UV lamp in air ($\lambda = 185$ nm and 257 nm, which generates ozone). PVP removal by thermal treatment involved pyrolysis in a flow of $100 \text{ cm}^3 \cdot \text{min}^{-1}$ 20% v/v H_2/Ar at $2 \text{ K} \cdot \text{min}^{-1}$ to 873 K (2 h), followed by a passivation at room temperature in 1% v/v O_2/Ar .

3.1.2.3 Structured Ni/ACF for hydrogenations with H_2

Materials

Nickel(II) nitrate hexahydrate (Fluka, $\geq 98.0\%$), nitric acid (VWR chemicals, 65%), and hydrogen peroxide (reactolab SA, 30%) were used for the catalysts preparation.

Procedure

The preparation of the nickel-based catalysts supported on ACFs is very similar to the MO_x/ACF catalysts. Differences have been implemented to favour a greater extent of metallic Ni in the resulting nanoparticles during the thermal treatment.

The incipient wetness impregnation method was first applied. Commercial ACFs were pre-treated in 15 wt.% HNO_3 aq. solution for 3 min at 298 K or for 15 min at 373 K. The catalysts prepared from these pre-treated supports are referred as $\text{Ni}/\text{ACF}_{\text{HNO}_3-298}$ and $\text{Ni}/\text{ACF}_{\text{HNO}_3-373}$, respectively. The catalysts prepared from supports not pre-treated and used as received were denoted as Ni/ACF. The ACFs were impregnated with an ethanolic solution of the Ni precursor ($\text{Ni}(\text{NO}_3)_2 \cdot 6\text{H}_2\text{O}$) ensuring the filling of the pores and dried at room temperature (RT) overnight. The desired Ni loading was obtained by varying the precursor concentration. The precursor decomposition was performed via thermal treatment in a flow reactor (50 cm x 3 cm i.d.) from RT to 673 K, $6 \text{ K} \cdot \text{min}^{-1}$ under Ar flow ($280 \text{ cm}^3 \cdot \text{min}^{-1}$), maintained at 673 K (1 h) under 17% v/v H_2/Ar flow ($340 \text{ cm}^3 \cdot \text{min}^{-1}$) and cooled to RT under Ar. The resulting pyrophoric MO_x/ACF s materials were passivated for 1 h at RT in 2.8% v/v

air/Ar flow ($145 \text{ cm}^3 \cdot \text{min}^{-1}$). Gas flows were controlled using an Agilent Technologies ADM1000 Universal Gas Flowmeter, values are given in IUPAC STP.

3.1.3 Raney Nickel catalyst

Ni-Al (1 g, 50:50 wt.% alloy, Alfa Aesar) was treated with an aq. solution of KOH (10 wt.%) and stirred at RT until bubbling (H_2) stopped ($\sim 1 \text{ h}$), then at 333 K for 0.5 h. The resulting solid (Raney Ni) was decanted, washed with distilled water (100 cm^3) and ethanol (100 cm^3).

3.2 Liquid-phase hydrogenation of nitroaromatic compounds

All the gases (N_2 , H_2) ($> 99.99 \%$) used during the liquid-phase hydrogenation of nitroaromatics were purchased from Carbagas Switzerland.

3.2.1 Semi-batch reactor set-up

Liquid-phase reductions were carried out in a commercial semi-batch stainless steel stirred reactor (150 cm^3 , Büchi AG, Uster, Switzerland) equipped with 6 wall baffles (**Figure 3.1A**). The reaction temperature was controlled using an oil heating bath Ministat 125 (Huber Kältemaschinenbau GmbH, Germany)² connected to a reactor jacket. A 6-blade disk turbine impeller ensured intensive mixing. The catalyst, when supported, was fixed on 4 wire-mesh blades attached directly to the stirrer shaft (**Figure 3.1B**). For the unsupported catalysts, a stirrer devoid of the 4 wire-mesh blades was employed. The stirrer was driven by a magnetic drive and equipped with a speed controller (cyclone 075/cc 075, Büchi AG, Uster,

² Colora K4 (Lorch, Germany) for the nickel study.

Switzerland). The reactor temperature, pressure and stirring speed were monitored *via* a control unit (bpc 6002/bds mc, Büchi AG, Uster, Switzerland).

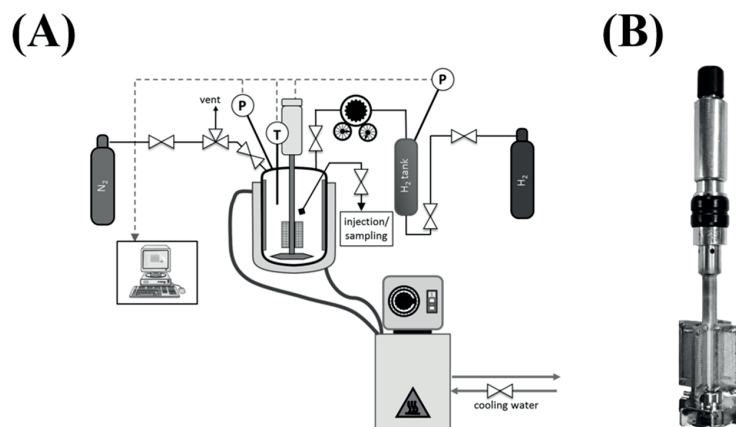


Figure 3.1. (A) Scheme of the 3-phase semi-batch reactor and (B) picture of the stirrer on which the structured catalysts were fixed.

3.2.2 CTH over structured MO_x/ACF (M = Fe, Co, Ni)

Materials

p-nitroanisole (97%, Alfa Aesar), *p*-nitrotoluene (> 98%, Fluka), *m*-nitrostyrene (97%, stabilized, Acros), nitrobenzene (99%, Acros), *p*-chloronitrobenzene (99%, Sigma Aldrich), *m*-xylene (> 98%, Fluka) and hydrazine monohydrate (~100%, Merck) were used as received without further purification.

Procedure

Prior to each experiment the reactor was charged with 0.3 g of the catalyst and 100 cm³ of an ethanol solution of nitroarenes (0.12 M) and 1 g of *m*-xylene (internal standard for GC analyses). After flushing (4 times) with N₂ under agitation (~2000 rpm) to remove air, the reactor was heated to 333 K and equilibrated for 5 min. Injection of 1.8 cm³ of the reducing agent (3 equivalents), *i.e.* hydrazine monohydrate, defined the start of the reaction. A typical reaction was performed at T = 333 K, under an initial differential pressure equivalent to vapour pressure of ethanol at this temperature. An agitation speed of 2000 rpm was applied.

The initial substrate to metal molar ratio of 50 was used by adjusting the mass of catalyst introduced in the reactor. A 1 cm³ syringe (Codan Medical AG) connected to the sampling valve allowed the controlled non-invasive withdrawal of small aliquots (~0.2 cm³) from the reactor during the reaction. In a series of blank experiments, no conversion of the substrates was detected in the absence of the catalyst or in the presence of the ACFs support only.

3.2.3 Hydrogenation with H₂ over unsupported Ni, Au and Ni-Au NPs

Materials

Methanol (Sigma-Aldrich, ≥ 99.8%), ethanol (Sigma-Aldrich, 99.8%), 1-propanol (Acros Organics, 95.5%), 1-butanol (Acros Organics, 95.5%), 2-hexanol (Sigma-Aldrich, 99%) and *m*-DNB (Tokyo Chemical Industry, ≥ 99.0%) were used as received.

Procedure

The reactor was charged with 80 cm³ of a methanol solution of *m*-DNB (3.7×10⁻³ M) and 0.4 g of 1-butanol (internal standard for GC analyses). The NPs were introduced by injection into the reactor as ethanolic solutions (0.08–0.38 cm³) to reach the desired *m*-DNB to Ni molar ratio. After flushing (4 times) with N₂ under agitation (~2000 rpm) to remove air, the reactor was heated to 423 K and equilibrated for 5 min. H₂ was introduced into the reactor to a total pressure of 20 bars (sum of the partial pressures of MeOH and H₂). An initial substrate to metal molar ratio ranging 28–58 was used by adjusting the mass of catalyst introduced in the reactor. A 2.5 cm³ gas-tight syringe (Hamilton Bonaduz AG, Switzerland) connected to the sampling valve allowed the controlled withdrawal of small aliquots (~0.2 cm³) from the reactor during the reaction. In a series of blank experiments, no conversion of the substrates was detected in the absence of the catalyst or in the presence of the ACFs support only.

3.2.4 Hydrogenation with H₂ over ACFs-supported Ni and Ni-Au NPs catalysts

Materials

Methanol (Sigma-Aldrich, $\geq 99.8\%$) and *m*-dinitrobenzene (Tokyo Chemical Industry, $\geq 99.0\%$) were used as received.

Procedure

Prior to each experiment the reactor was charged with 0.015–0.03 g of the catalyst and 80 cm³ of a methanol solution of *m*-DNB (3.7×10^{-3} M) and 1 g of 1-butanol (internal standard for GC analyses). The next steps of the procedure are the same than for the H₂-assisted reduction over the unsupported Ni, Au, Ni-Au NPs.

3.2.5 Hydrogenation over structured Ni/ACF catalysts

Materials

Nitrobenzene (99%, Acros Organics), *p*-chloronitrobenzene (99%, Acros Organics), *m*-dinitrobenzene (Tokyo Chemical Industry, $\geq 99.0\%$), dodecane (99%, Acros Organics) and technical ethanol (95% + 5% MeOH, 99.8%, Brenntag) were used as received.

Procedure

Prior to each experiment the reactor was charged with 0.3 g of the catalyst and 100 cm³ of an ethanol solution of *m*-xylene (1 g, internal standard for GC analyses). After flushing (4 times) with N₂ under agitation (~2000 rpm) to remove air, the reactor was heated up 353 K and stabilized for 5 min. H₂ was introduced into the reactor to a total pressure of 10 bars (sum of the partial pressures of EtOH and H₂). The catalyst was reduced *in-situ* for 30 min. The substrate (0.012 mol) was subsequently injected (time $t = 0$) *via* a 5 cm³ gas-tight syringe (Hamilton Bonaduz AG, Switzerland) under the same agitation, temperature and pressure conditions used during the *in-situ* activation. An initial substrate to metal molar ratio of 50

was used by adjusting the mass of catalyst introduced in the reactor. A 2.5 cm³ gas-tight syringe (Hamilton Bonaduz AG, Switzerland) connected to the sampling valve allowed the controlled withdrawal of small aliquots (~0.2 cm³) from the reactor during the reaction. In a series of blank experiments, no conversion of the substrates was detected in the absence of the catalyst or in the presence of the ACFs support only.

3.2.6 Model reactions

The prepared structured catalysts were tested in 3 model reactions (cf. **Table 3.1**). *Para*-chloronitrobenzene (*p*-CNB) is commonly reduced industrially into *para*-chloroaniline (*p*-CAN) which is used as an intermediate for the production of dyes, pigments, pharmaceuticals and agricultural chemicals.¹ Its substituent is a chloro-group whose bond to the benzene ring can easily be cleaved during the hydrogenation (cf. **Figure 3.2**).

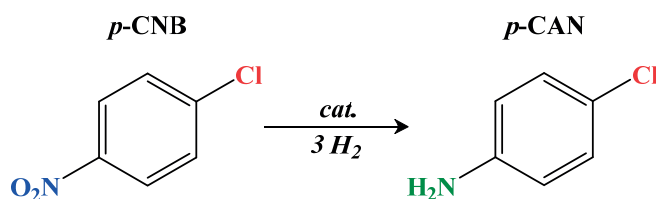


Figure 3.2. Reduction of *para*-chloronitrobenzene (*p*-CNB) into *para*-chloroaniline (*p*-CAN). The chloro-, nitro- and amino- groups are highlighted in red, blue and green, respectively.

The reduction *meta*-nitrostyrene (*m*-NS) into *meta*-vinylaniline (*m*-VA) is challenging due to the high sensitivity of the vinyl group towards. Therefore, high *m*-VA yields are difficult to achieve.

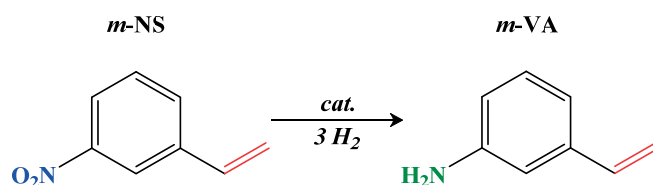


Figure 3.3. Reduction of *meta*-nitrostyrene (*m*-NS) into *meta*-vinylaniline (*m*-VA). The vinyl, nitro- and amino- groups are highlighted in red, blue and green, respectively.

The last model reaction was the partial reduction of *meta*-dinitrobenzene (*m*-DNB) into *meta*-nitroaniline (*m*-NAN) where the over-hydrogenation in *m*-PDA was undesired. The transformation of only one of the two nitro groups represents above all a technical challenge. There is no specific application in view since the industries rather use the over-hydrogenated product (*m*-PDA).

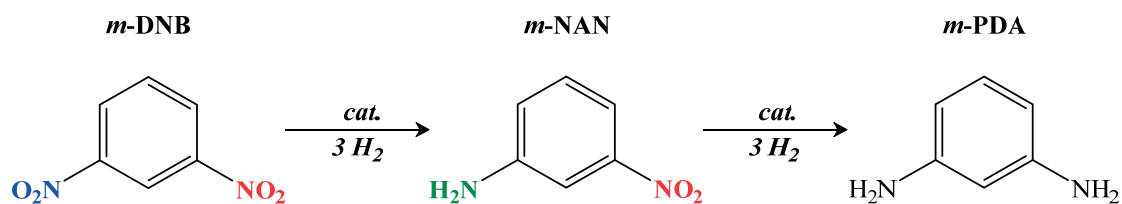
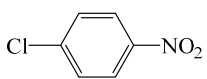
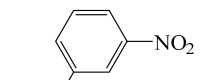
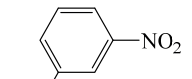
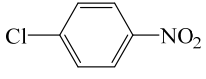


Figure 3.4. Reduction of *meta*-dinitrobenzene (*m*-DNB) into *meta*-nitroaniline (*m*-NAN).

Summary**Table 3.1.** Main experimental conditions and information per chapter.

Section	Chapter 4	Chapter 5	Chapter 6
Main substrates	 <i>para</i> -chloronitrobenzene  <i>meta</i> -chloronitrobenzene	 <i>meta</i> -dinitrobenzene	 <i>para</i> -chloronitrobenzene
Temperature (K)	333	423	353–423
Reducing agent (RA)	N ₂ H ₄ ·H ₂ O	H ₂	H ₂
RA/substrate molar ratio (-)	3	-	-
Total differential pressure (bar)	-	20	10
H ₂ partial pressure	-	6–7	8–9
Agitation (rpm)	2000	2000	2000
Mass of catalyst (g)	0.3	0.015–0.03	0.3
Initial substrate concentration (M)	0.12	3.7×10 ⁻³	0.12
Substrate/Metal molar ratio (-)	50	28–58	50
V _{bulk} (cm ³)	100	80	100
Solvent	EtOH	MeOH	EtOH

3.3 Analytical method

The composition of the reaction mixture was determined using a gas chromatograph (AutoSystem XL or Clarus 500, Perkin–Elmer, USA), equipped with a programmed split/splitless injector, flame ionization detector and Elite-35MS 35% phenyl(methylpolysiloxane) capillary column (i.d. = 0.32 mm, length = 30 m, film thickness = 0.25 μm) with *m*-xylene as an internal standard. During the method applied for the hydrogenation of nitroaromatic compounds, the oven temperature was maintained 0.75 min at 273 K, increased successively to 413 K at 20 K·min⁻¹ and eventually augmented to 538 K at 45 K·min⁻¹ (dwell of 1 min at 538 K).

The conversion of the substrate A is defined as:

$$X_A (\%) = \frac{C_{A_0} - C_A}{C_{A_0}} \times 100 \quad (3.1)$$

where C_{A_0} and C_A represent the molar concentrations of the product A at the start of the reaction and at time t , respectively. ν_A is the stoichiometric coefficient of the product A.

The selectivity of product B with respect to substrate A is defined as:

$$S_{BA} (\%) = \frac{C_{B_0} - C_B}{C_{A_0} - C_A} \cdot \frac{\nu_A}{\nu_B} \times 100 \quad (3.2)$$

where C_{B_0} and C_B represent the molar concentrations of the product B at the start of the reaction and at time t , respectively; ν_A and ν_B are the stoichiometric coefficients of products A and B, respectively.

The yield towards the product B with respect to substrate A is defined as:

$$Y_{BA} (\%) = X_A \cdot S_{BA} = \frac{C_{B_0} - C_B}{C_{A_0}} \times 100 \quad (3.3)$$

The catalyst activity response was evaluated measuring the initial transformation rate, R_0 - the number of moles of substrate converted in the reactor per unit of time referred to the

number of moles of metal. The initial activity was calculated for the reaction time required to reach a conversion of 20% from:

$$-R_0 \left(\text{mol}_A \cdot \text{mol}_M^{-1} \cdot \text{s}^{-1} \right) = \frac{C_{A_0} - C_A}{t \cdot n} \cdot V \quad (3.4)$$

where V is the volume of the reaction mixture, t is the time and n is the number of moles of metal.

Alternatively, the turnover frequency (TOF):

$$\text{TOF} (\text{s}^{-1}) = \frac{-R_0}{D} \quad (3.5)$$

where D is the average NP dispersion, defined by the ratio of surface atoms to the total number of atoms.

3.4 Characterization techniques

3.4.1 Atomic absorption spectroscopy (AAS)

Determination of the catalysts metal content was achieved using a Shimadzu AA-6650 spectrometer with an air-acetylene flame. All ACFs-based samples were burnt in air with a Bunsen burner and subsequently calcined in an oven Thermicon P (Heraeus, Germany) at 873 K for 2 h. The remaining solid (metal oxide) was dissolved in aqua regia ($\text{HNO}_3:\text{HCl}$ v/v = 1:3) and diluted in demineralized water. The wavelengths used for Fe, Co, Ni and Au were 240.7, 248.3, 232.0 and 242.8 nm, respectively.

3.4.2 N_2 physisorption

The specific surface areas (SSA) of the support and prepared catalysts were measured by adsorption–desorption of N_2 at 77 K using a Sorptomatic 1990 (CE instruments, UK) or a 3Flex (Micromeritics, USA). Prior to analysis, samples were outgassed at 523 K for 2 h under

vacuum (7×10^{-2} bar). N₂ adsorption/desorption isotherms were recorded over the range $0.0005 \leq P/P_0 \leq 0.98$. The SSA and the total pore volume were calculated using the BET method with the following equation:¹¹⁴

$$\frac{P}{V(P_0 - P)} = \frac{1}{V_m C} + \frac{C - 1}{V_m C} \frac{P}{P_0} \quad (3.6)$$

where P is the partial pressure of the adsorbed gas, here N₂, P_0 is the saturation pressure, V is the volume of gas adsorbed at STP conditions, V_m is the volume adsorbed in one complete unimolecular layer and C is a constant linked to enthalpy of adsorption of the adsorbate on the sample. The N₂ monolayer volume (V_m) is obtained by the linearization of equation (3.6). The pore volume was calculated with the N₂ volume adsorbed at $P/P_0 = 0.98$.

3.4.3 X-ray diffraction (XRD)

X-ray diffraction (XRD) patterns were recorded on a Bruker/Siemens D500 incident X-ray diffractometer using CuK α radiation ($\lambda = 0.154$ nm). The samples were scanned at 0.004°s^{-1} over the range $20^\circ \leq 2\theta \leq 90^\circ$ (scan time = $5 \text{ s}\cdot\text{step}^{-1}$). If different the range is specified in the text. The diffractograms were compared to JCPDS-ICDD reference standards, *i.e.* Fe₂O₃ (00-033-0664), Fe₃O₄ (01-071-6336), Co (15-0806), CoO (43-1004), Co₃O₄ (74-1656), Ni (89-7129), NiO (89-5881) and NiO₂ (89-8397).

In-situ XRD was performed on Ni(NO₃)₂/ACF_{HNO3-373}, to study the evolution of active phase on impregnated fibres during thermal treatment in N₂ or N₂ + H₂ flows. The specimen was placed in the heating chamber (XRK 900, Anton Paar) and N₂ gas was applied through the mass flow controller (5850 TR, Brooks instrument). About 0.03 g of sample was heated under a $60 \text{ cm}^3 \text{ min}^{-1}$ flow of N₂ up to 723 K with a heating rate of 2 K min^{-1} . Long scans ($30^\circ \leq 2\theta \leq 85^\circ$) were acquired on the fresh sample, directly after heating to 723 K. In a separate experiment on a sample of the same batch, the procedure was modified by replacing

the N₂ by 10% v/v H₂/N₂. A long scan was performed at the end of the procedure. Peak fitting was performed using the *EVA (DIFFRAC.Suite)* software.

3.4.4 X-ray photoelectron spectroscopy (XPS)

XPS analyses of catalysts used in CTHs were conducted on an Axis Ultra instrument (Kratos analytical). The source power was maintained at 150 W and the emitted photoelectrons were sampled from a 750 μm × 350 μm area at a take-off angle = 90°. The analyser pass energy was 80 eV for survey spectra (0–1100 eV) and 40 eV for high resolution spectra (Fe 2p_{3/2} and Fe 2p_{1/2}, Co 2p_{3/2} and Co 2p_{1/2}). The adventitious C (284.6 eV) and O (530.8 eV) 1s peaks were used as internal standards to compensate for any charging effects.

Spectra of Ni/ACFs catalysts were performed Ni 2p_{3/2} and Ni 2p_{1/2} on PHI VersaProbe II (Physical Instruments AG). The monochromatic Al Kα X-ray source power was maintained at 24.8 W and the emitted photoelectrons were obtained from a 100 μm × 100 μm samples. The spherical capacitor analyser was set at a 45° take-off angle with respect to the sample surface. The analyser pass energy was 188 eV for survey spectra (0–1300 eV) and 47 eV for high resolution spectra (Ni 2p_{3/2} and Ni 2p_{1/2}). For the latter resolution a full width at half maximum of 0.91 eV for the Ag 3d 5/2 peak was obtained. The adventitious C (284.8 eV) 1s peak was used as an internal standard to compensate for any charging effects. Sputtering was realized using a 20 kV Ar₂₅₀₀⁺ cluster source on a 2 nm × 2 nm sample surface at a rate of 0.45 nm·min⁻¹ (referenced to SiO₂). Curve fitting was performed using the CasaXPS software

3.4.5 Scanning electron microscopy

SEM imaging was performed with a Philips FEI XL30-FEG equipped with an Everhart-Thornley secondary-electron (SE) detector using an accelerating voltage between 10–13 kV, or with a Carl Zeiss MERLIN FE-SEM equipped with two annular and Everhart-Thornley

secondary-electron (SE) detectors operated at an accelerating voltage of 5–30 keV with a beam current of 1.0–3.0 nA and using ZeissSmartSEM software for data acquisition/manipulation.

3.4.6 Transmission electron microscopy (TEM)

High angle annular dark-field scanning transmission electron microscope (HAADF STEM) images were acquired using an FEI Tecnai Osiris instrument for the MO_x/ACF catalysts used in CTH (**Chapter 4**) and ACF-supported preformed Ni and Ni-Au NPs catalysts

(**Chapter 5**) used in *m*-DNB hydrogenation. The measurements were operated at the maximum accelerating voltage of 200 keV. Chemical mappings were obtained using the “Super-X” energy-dispersive X-ray (EDX) spectroscopy detector.

Unsupported Ni, Au and Ni-Au NPs (**Chapter 5**) were visualized by HRTEM using a JEOL JEM-3011 instrument at 200 keV. Energy Dispersive X-Ray (EDX) analysis was performed using a 7 nm beam diameter (note that this does not reflect the true area over which data was collected due to secondary effects), PGT prism Si/Li detector and an Avalon 2000 analytical system.

Specimens of Ni/ACF catalysts (**Chapter 6**) employed in hydrogenations with H₂, were analysed on a FEI Talos F200S instrument. These TEM samples were subjected to mild (10 eV) plasma cleaning for 1 min using a Fischone 8070 plasma cleaner operated with a forward power of 9 W. The measurements were operated at the maximum accelerating voltage of 200 keV.

Specimens of the ACFs-based catalysts were prepared by infiltrating-embedding single fibres into an EPON 812 epoxy resin followed by its polymerization at 333 K for 24 h. Ultramicrotomy (diamond grade) was used to cut 20–60 nm thick fibre cross-sections that

were eventually deposited on a holey carbon/Cu grid (300 Mesh). The particles size distributions (PSD) of the Ni/ACF specimens were obtained by counting up to 1400 individual metal particles. The circular diameter (d_i) was determined from the area measured using imageJ software from images of different magnifications. The mean circular diameter (d) was calculated using equation (3.7):

$$d = \frac{\sum_i n_i d_i}{\sum_i n_i} \quad (3.7)$$

where n_i is the number of particles of diameter d_i .

For the catalysts (unsupported and supported) in **Chapter 5**, the same equation was applied, but the diameter measurement was done manually up to 250 individual NPs.

3.4.7 Temperature-programmed reduction in hydrogen (TPR)

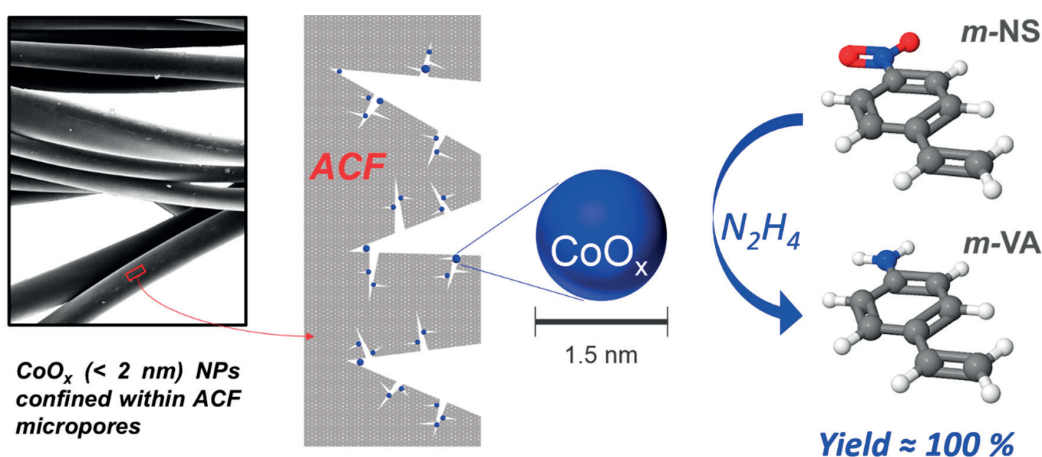
TPR measurements were carried out using an Autochem II 2920 system (Micromeritics, USA). Samples positioned in a U-shaped quartz cell (10 mm i.d.) were heated in a $20 \text{ cm}^3 \cdot \text{min}^{-1}$ 5% v/v H_2/Ar flow at $2 \text{ K} \cdot \text{min}^{-1}$ to 973 K. After passing the outlet gas stream through a cold trap, immersed in a nitrogen/isopropanol, it was monitored by a TCD to determine H_2 concentration variations. Data were acquired/manipulated with TPR WinTM software. NORAN System SIX (version 1.6) was used for data acquisition.

3.4.8 Temperature-programmed decomposition (TPD)

TPD measurements were conducted by heating samples in a He flow ($50 \text{ cm}^3 \cdot \text{min}^{-1}$) at $6 \text{ K} \cdot \text{min}^{-1}$ to 1173 K. The outlet gas flow composition was monitored by a mass spectrometer (Thermostar TM GSD 300 T2, Pfeiffer Vacuum). When quantified, the CO and CO_2 issued from the decomposition of oxygen-containing groups present in ACFs were quantified with diluted calibrated mixtures of 3% v/v CO/He and 2% v/v CO_2/He .

Chapter 4

Highly Dispersed Non-Precious Metal Oxides Nanoparticles on Activated Carbon Fibres as Efficient Structured Catalysts for the Transfer Hydrogenation of Nitroarenes



This chapter is based on the following publications:

Beswick, O., *et al.*, Iron oxide nanoparticles supported on activated carbon fibers catalyze chemoselective reduction of nitroarenes under mild conditions. *Catalysis Today*, 2015. 249: p. 45-51.

And

Beswick, O., *et al.*, Highly dispersed cobalt oxides nanoparticles on activated carbon fibres as efficient structured catalysts for the transfer hydrogenation of m-nitrostyrene. *Catalysis Today*, 2017.

Abstract

The facile preparation of structured catalysts featuring highly-dispersed non-precious metal (Fe, Ni, Co) oxide nanoparticles (~2 nm) stabilized within a super-microporous network of activated carbon fibres (ACFs) is described in this chapter.

The catalyst morphology was controlled over multiple levels from the nano-designed active phase up to the macro-structure of the ACFs support. A range of physicochemical techniques was used to characterize the catalyst and rationalize the catalytic results. The structured iron-based nanocatalyst showed high activity and chemoselectivity in the reduction of different functionalized nitroarenes to the corresponding anilines under mild conditions using hydrazine hydrate as the reducing agent and high yields of the target products (91–100%). The challenging reduction of *m*-nitrostyrene containing an easily reducible vinyl-group was achieved with a near-quantitative yield (99.4%) of *m*-vinylaniline over CoO_x/ACF structured catalyst.

4.1 Introduction

The importance of nitroarenes as key building blocks for the chemical industry was shown in **Chapter 2**. Pharmaceuticals, dyes, pigments, polymers, and agrochemicals are typical examples of finished products which are produced from these intermediates.^{1,115} They are industrially produced by the selective hydrogenation of the corresponding nitroarenes over catalysts based on precious metals (Pt, Pd, etc.) or nickel (*e.g.* nickel-on-kieselguhr) in the presence of gaseous hydrogen. Catalytic transfer hydrogenation relies on hydrogen donors (hydrazine,⁷⁸ formic acid,⁵⁷ isopropanol¹¹⁶) rather than gaseous hydrogen to reduce substrates. While CTH circumvents the dependence on expensive high pressures equipment and safety-related issues by avoiding the use of pressurized H₂, another major interest of this approach is the possibility of achieving better chemoselectivities. To date, only few examples of catalysts based on the inexpensive earth abundant metals, (Fe, Co, Ni, Ce, etc.) and efficient in the CTH of nitroarenes have been reported (**Section 2.1.6.1, 2.1.6.2**).^{57,68}

Catalyst handling, separation and mass transport limitations are associated with the use of catalysts in the form of powder or pellets in liquid-phase processes. Among structured supports, activated carbon fibres (ACFs) materials (tissue, felt, etc.), possess a macrostructure consisting of arranged microfilaments (10–20 μm) and high specific surface area (up to 3000 m²·g⁻¹). The former characteristic enables fast adsorption from gas and liquid phases, high fluid permeability and easy handling while its high-surface-area affords the synthesis of highly dispersed nanoparticles.^{117,118}

This chapter describes the facile preparation of ACF-based structured catalysts with supported-transition metal (Fe, Co, Ni) oxides nanoparticles as an active phase. Fe-oxide NPs supported on activated carbon fibres (FeO_x/ACF) showed up to 100% yield of the desired anilines during hydrazine assisted CTH of variety of a nitroarenes but not for *m*-nitrostyrene (*m*-NS) which transformation yielded *m*-vinylaniline (*m*-VA) below 80%. The creation of

cobalt nanoparticles (< 2 nm) on ACF treated by nitric acid lead to a catalyst (CoO_x/ACF_{HNO3}) able to afford the desired *m*-VA in the CTH of *m*-NS product in near-quantitative yield. Considering the potential applications of these catalytic systems in batch as well as in flow-mode, the results presented in this chapter could offer new avenues for in the sustainable synthesis of arylamines.

4.2 Experimental

Material

All catalysts were prepared according to the procedure detailed in **Section 3.1.2.1**. Co(II, III) oxide nanoparticles (< 50 nm, Sigma-Aldrich) were used as a powder catalyst for comparison with the structured Co-based catalysts. Catalysts prepared using ACFs treated by nitric acid were referred as $\text{MO}_x/\text{ACF}_{\text{HNO}_3}$.

Characterization of the catalysts

Metal content was determined by AAS. The decomposition of metal precursors was studied by TPD. Specific surface area and pore volumes were measured by N_2 isotherm adsorption at 77 K (BET). The morphology of the support and nanoparticles was observed by SEM and STEM-HAADF, respectively. XRD and XPS were used to characterize the composition of the nanoparticles. The experimental conditions and instruments specifications used during these characterizations are described in **Section 3.4**.

Liquid catalytic transfer hydrogenation

The reduction of nitroarenes into their corresponding anilines was conducted following the steps and conditions detailed in **Section 3.2.2**. The main substrates used during this study were *para*-chlorobenzene and *meta*-nitrostyrene (cf. **Table 3.1**). The calculations of conversion, selectivity, yield and transformation rate were realized using the equations presented in **Section 3.3**.

4.3 Results and Discussion

4.3.1 Characterization of the MO_x/ACF catalysts

Temperature-programmed decomposition

The catalysts were prepared by decomposing metal oxide precursors (nitrates) supported on ACFs under an inert atmosphere. In order to optimize the preparation conditions, temperature programmed decomposition (TPD) of the Fe, Co and Ni nitrates supported on ACFs was studied. **Figure 4.1** shows that complete Fe, Co and Ni oxide precursors decomposition takes place in the range 430–600 K. The NO peak corresponds to the decomposition of NO₃⁻ groups. Detected CO and CO₂ (1st broad peak) are produced through oxidation of the ACFs support by generated nitrogen oxides. Therefore, a temperature of 623 K was chosen for standard thermal treatments. The CO and CO₂ peaks at higher temperature, *e.g.* ~980 K for CO signal of the Fe(NO₃)₃/ACF sample, may be ascribed to partial reduction of metal oxide by carbon. It is noteworthy that the position of these peaks and amounts of CO and CO₂ produced during the procedure depends on the metal used and shifts to lower temperatures when passing from Co to Ni (**Figure 4.1B, C**). This indicates, among the 3 metals, different ability to catalyze the reduction of support into CO and CO₂ as well as a different susceptibility to phase transition with respect to temperature.

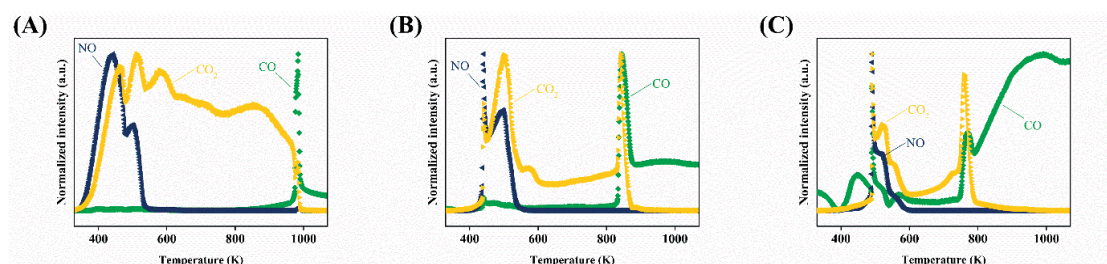


Figure 4.1. TPD profiles of (A) Fe(NO₃)₃/ACF, (B) Co(NO₃)₂/ACF and (C) Ni(NO₃)₂/ACF (◄ CO; ► CO₂; ◆ NO). Metal loading (wt.%) of Fe, Co, Ni = 6.1, 4.3, 4.9, respectively. Ramp = 6 K·min⁻¹; Flowrate = 50 cm³·min⁻¹ of He; masses monitored = 2, 16, 18, 28, 30, 44, 46 (2, 16, 18 and 46 are not shown on the charts).

Characterization of MO_x Nanoparticles

A characterisation of the synthesized MO_x /ACF catalysts by different techniques allowed assessing the catalysts structure and active phase nature. The very low activity of the NiO_x /ACF catalysts prompted us to focus more on iron or cobalt catalysts.

N_2 adsorption

The low temperature (77 K) N_2 adsorption isotherms measured for the ACFs support and MO_x /ACF catalysts have a profile of the type I (according to the IUPAC classification) typical for microporous materials (pore diameter < 2 nm). The SSA and total pore volume (V_p) calculated for the ACFs support are $\sim 2170 \text{ m}^2 \cdot \text{g}^{-1}$ and $\sim 1.01 \text{ cm}^3 \cdot \text{g}^{-1}$, respectively. After deposition of metal oxide (6–10 wt.% of metal) a moderate (4–7 %) decrease of SSA and pore volume was detected. These low changes in the porous structure after deposition of metal oxides are illustrated in **Figure 4.2** which compares the isotherms of initial ACFs and two iron catalysts of different loading.

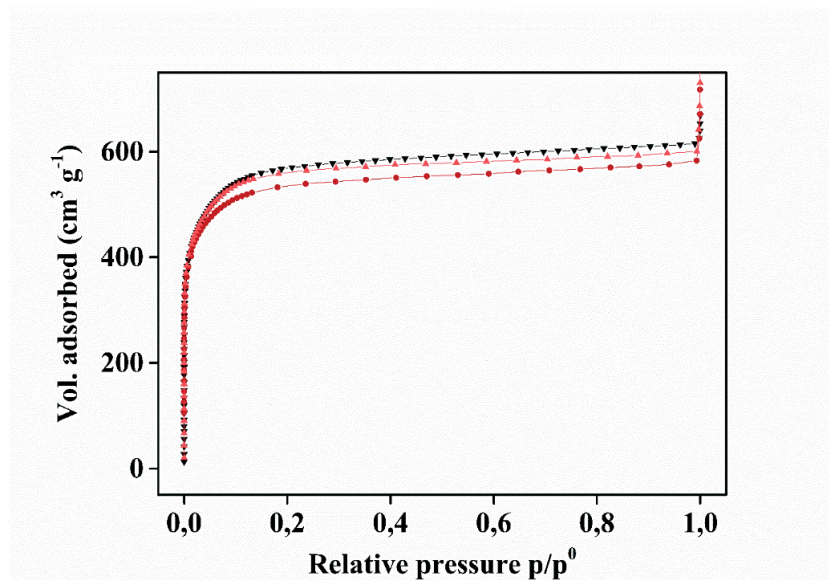


Figure 4.2. N_2 adsorption isotherms of ACFs support (\blacktriangledown) and FeO_x /ACF catalyst containing 2.8 wt.% (\blacktriangle) and 9.8 wt.% (\bullet) of Fe.

The formation of extremely small metal oxide NPs can explain an absence of micropore blocking with a negligible decrease of SSA and V_p . This implies that the porous network comprising the active phase is fully accessible to the reactants.

SEM

The ACFs support consists of uniform micro-sized ($\sim 10 \mu\text{m}$) elementary filaments. A scanning electron microscopy (SEM) at low magnification (30 X) revealed a 3D open regular macrostructure of the FeO_x/ACF catalyst (see **Figure 4.3A**) governed by the structure of the support. Such a structure provides enhanced hydrodynamic properties of the catalyst as compared to conventional micro-sized powdered catalysts due to a lower pressure drop. Moreover, the ACFs structured catalysts are easy to separate from the liquid phase after the reaction.¹¹⁸ At higher magnification (15'000 X), a surface texture (roughness) of the elementary fibre can be observed (**Figure 4.3B**). No particles were detected on the fibre outer surface. Thus, we can conclude that the deposited FeO_x is located within ACFs micropores. Carbon, oxygen and iron were identified by EDX spectroscopy as the main elemental constituents of the catalyst. Traces of Si, Ca, Cl and P were also detected (cf. **Appendix, Figure S4.1 and S4.2**). Their presence is ascribed to the chemicals used for the activation step during the ACFs production. EDX mapping revealed that all elements (except Si) were homogeneously distributed over the carbon fibres.

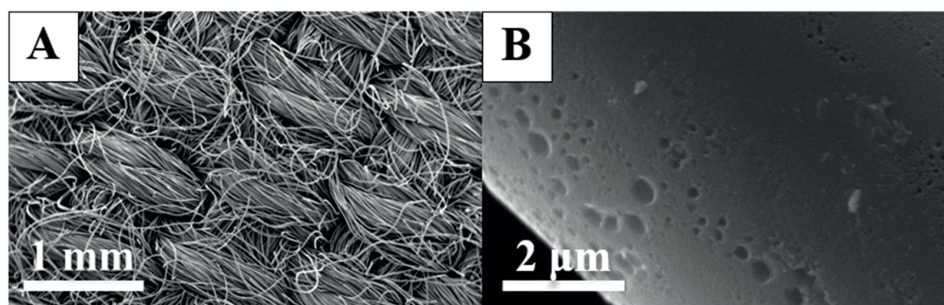


Figure 4.3. SEM images of FeO_x/ACF at (A) low (30 X) and (B) high (15'000 X) magnifications. Fe loading (wt.%): 3.5.

XRD

The MO_x/ACF catalysts were found to be XRD inactive. **Figure 4.4A** contains (as a representative example) the XRD pattern of the CoO_x/ACF catalyst. The fact that no peak is detected suggests that the MO_x particles supported on ACFs are extremely small and/or are amorphous.¹¹⁹ The presence of a highly dispersed phase confirmed by STEM (see below) explains the pyrophoricity of the non-passivated MO_x/ACF catalysts.

For comparison purposes, commercial Co₃O₄ nanopowder was characterized and subsequently tested in the reduction of *p*-CNB into *p*-CAN. The as-received powder was found to consist of a Co₃O₄ (**Figure 4.4B, F**) phase while its reduction afforded metallic Co (**Figure 4.4C, D**).

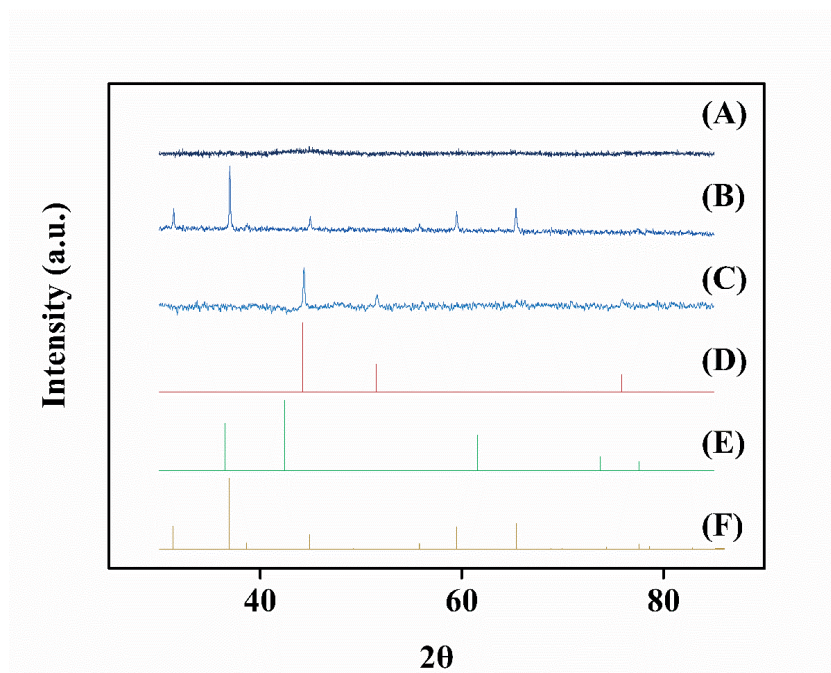


Figure 4.4. XRD patterns of (A) CoO_x/ACF, Co loading: 7.3 wt.%; commercial Co₃O₄ NPs (< 50 nm): (B) as-received and (C) after reduction; JCPDS-ICDD reference diffractograms for (D) Co (15-0806), (E) CoO (43-1004) and (F) Co₃O₄ (74-1656).

XPS

The position of the XPS Fe 2p_{3/2} and Fe 2p_{1/2} peaks (~711 eV and 724 eV, respectively) and the presence in the XPS spectrum of the characteristic satellite peak at ~718 eV (**Figure 4.5A**) indicate that these nanoparticles are composed of Fe₂O₃.^{120,121} In Co 2p XPS spectra of the synthesized CoO_x/ACF (**Figure 4.5B**) a non-symmetric Co 2p_{3/2} peak (780.9 eV) with a satellite (786.0 eV) are observed which does not correspond to metallic Co (Co 2p_{3/2} main peak is at 778.1 eV without any satellite) or Co₃O₄ (Co 2p_{3/2} – 779.6 eV).¹²² It is likely that metal is initially formed on the carbon surface during the precursor decomposition in an inert atmosphere. However, the passivation of the as-synthesized pyrophoric samples followed by exposure in air leads to their oxidation into MO_x NPs. As-received commercial Co₃O₄ NPs are characterized by a Co 2p_{3/2} peak at 780.1 eV (**Figure 4.5C**). In this case, the position and relative intensity of Co 2p_{3/2} satellite peak differ considerably to those of the CoO_x/ACF. The XPS pattern of the CoO_x/ACF is very similar to a spectrum of CoO (and/or Co(OH)₂), indicating Co²⁺ ions in the CoO_x/ACF catalyst.¹²² The XPS spectrum of reduced Co₃O₄ NPs appears to be a superposition of spectra of different phases (**Figure 4.5D**): Co₃O₄ and CoO (and/or Co(OH)₂), presumably due to the slow oxidation of the NPs in air. The higher signal-to-noise ratio of the MO_x/ACF catalysts (**A, B**) compared to the commercial nanoparticles (**C, D**) is linked to the samples metal content.

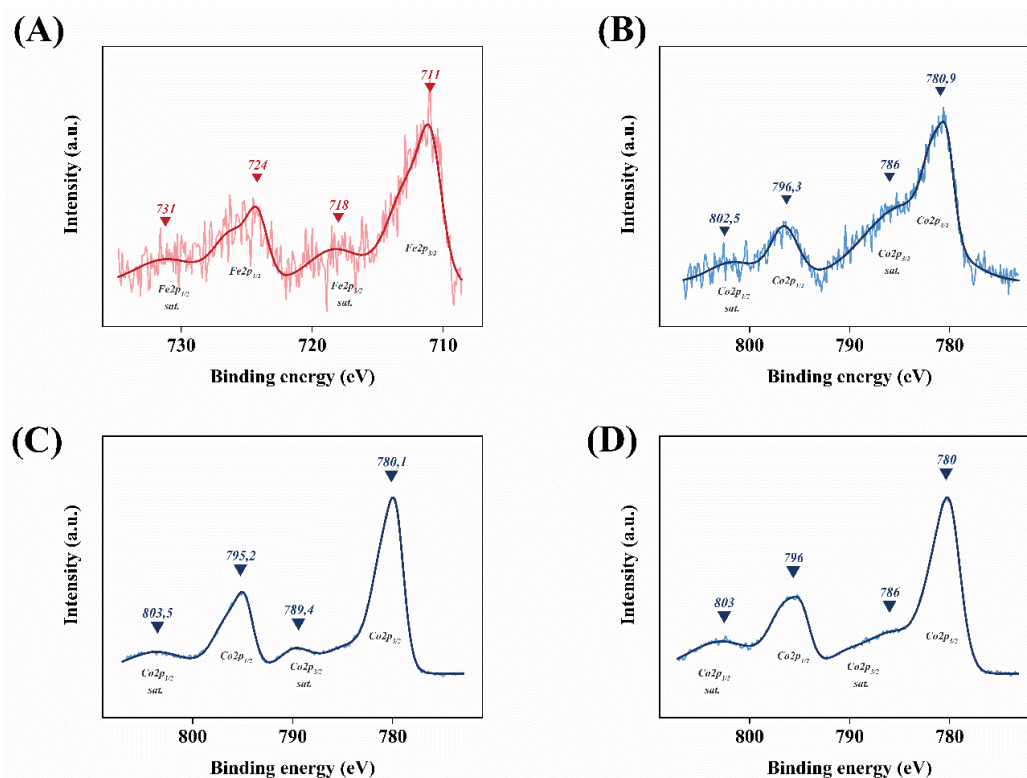


Figure 4.5. XPS profiles of (A) FeO_x/ACF, (B) CoO_x/ACF (both after nitrates decomposition) (Fe, Co loading (wt.%): 9.8, 7.3), commercial Co₃O₄ NPs (< 50 nm): (C) as-received and (D) after reduction.

STEM-HAADF

STEM-HAADF analysis of the catalysts was carried out to visualize the active phase of the MO_x/ACF catalysts. In a typical image (**Figure 4.6A, B1, C**), NPs (bright contrast) with an average size of ~2 nm, homogeneously distributed throughout the microtomed cross-sections of the ACFs support (dark contrast), are observed. **Figure 4.6B2** acquired by TEM-EDX mapping shows that the zones of high intensities correspond to Co-based NPs. Oxygen was found to be distributed over the carbon support with the highest concentrations at the metal locations, confirming that NPs consist in MO_x compound (*e.g.* CoO_x/ACF on **Figure 4.6B3**). The obtained results allow concluding that extremely small metal oxide NPs are formed on the ACFs support by wetness incipient impregnation and are homogeneously distributed through the ACFs pore network.

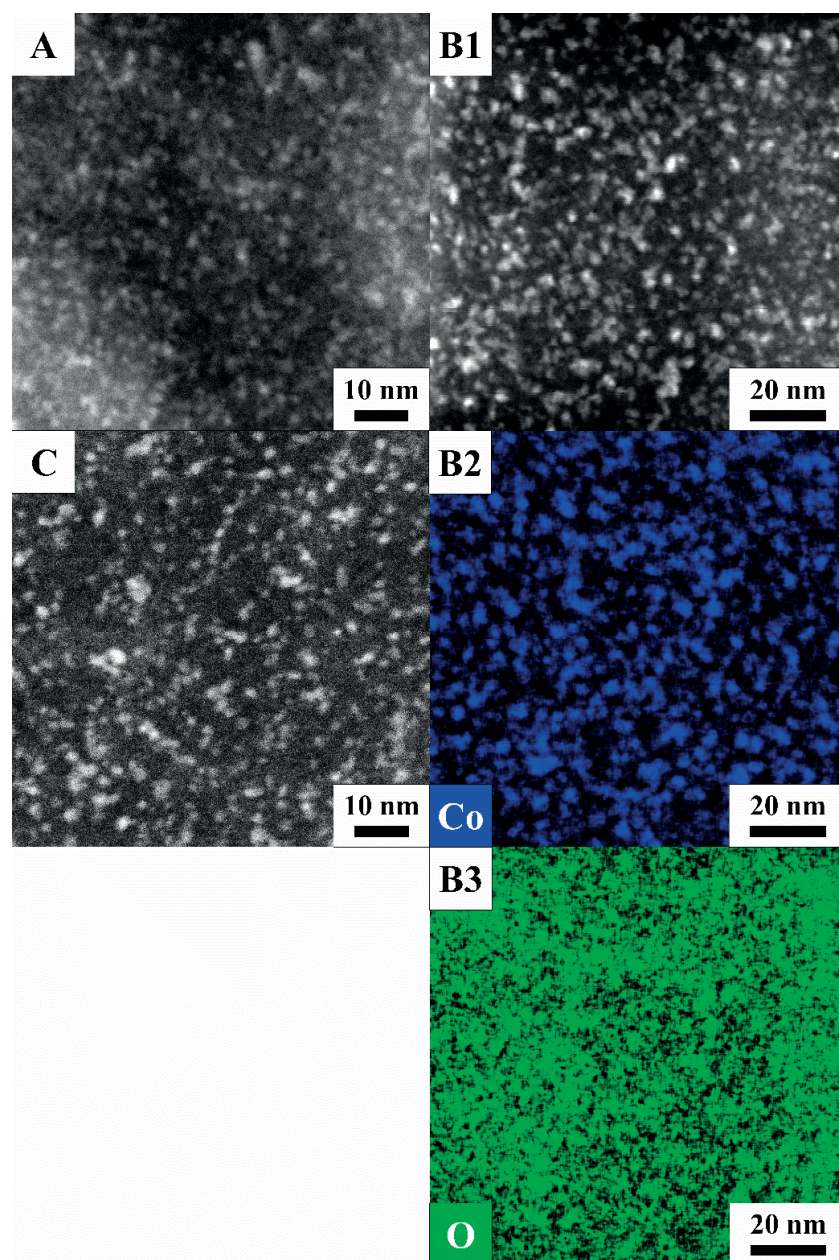


Figure 4.6. Representative STEM-HAADF images of (A) FeO_x/ACF, (B1) CoO_x/ACF and (C) NiO_x/ACF. MO_x NPs appear bright on the dark background (ACFs support). Co (B2) and O (B3) EDX images for CoO_x/ACF. Metal loading (wt.%) for the samples A, B, C = 7.0, 7.3, 9.8, respectively.

4.3.2 Catalytic testing of the MO_x/ACF catalysts

Reduction of p-CNB into p-CAN

The MO_x/ACF catalysts were tested in the CTH of *p*-chloronitrobenzene (*p*-CNB) using hydrazine as a model reaction. The initial specific activities and maximum yields obtained

using the Fe-, Co- and Ni-based catalysts are presented in **Figure 4.7**. The corresponding liquid bulk concentrations as a function of reaction time are presented in **Figure 4.8**.

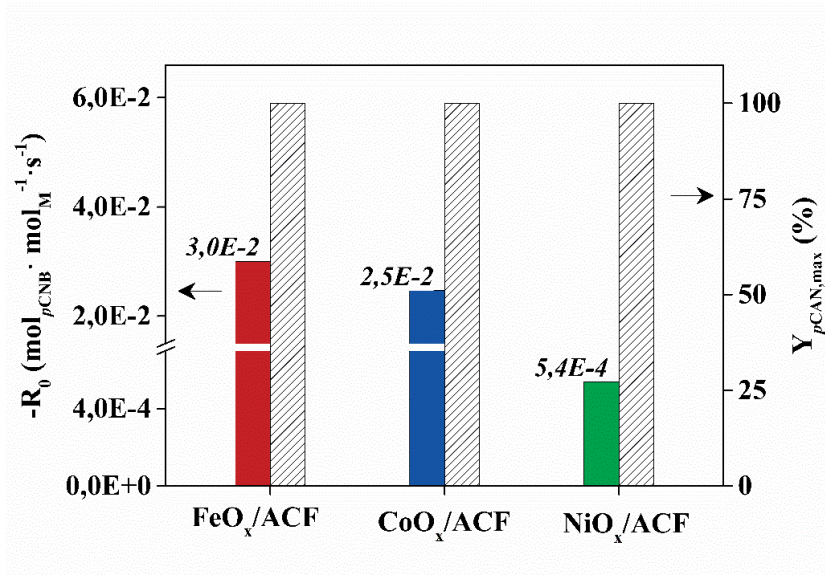


Figure 4.7. CTH of p -CNB with hydrazine: catalyst activity (solid bars) and maximum p -CAN yield (hatched bars) over MO_x/ACF catalysts. *Reaction conditions:* $C_{p\text{-CNB},0} = 1.2 \times 10^{-1} \text{ mol} \cdot \text{l}^{-1}$; 100 cm^3 of EtOH; $T = 333 \text{ K}$; molar ratio $\text{N}_2\text{H}_4:p\text{-CNB} = 3$; molar ratio $p\text{-CNB}:M = 50$. Metal loading (wt.%) of Fe, Co, Ni = 6.1, 6.0, 6.2, respectively.

Under the working conditions, the FeO_x/ACF and CoO_x/ACF catalysts are characterized by ~ 2 orders of magnitude higher activity than the NiO_x/ACF catalyst. Notably, the selectivity and maximum yield of the desired (p -CAN) was close to 100 % in all cases. Blaser *et al.* noted that the comparison of catalytic data of different research groups is arduous due to divergent conditions. Despite this remark being valid for the CTH of p -CNB, we will examine the most relevant results (summarized in **Table 4.1**). The p -CAN yield values spanned from 76 to 99% for the most selective catalysts. The Fe-based catalysts (Fe-phenanthroline/C-800) proposed by Jagadeesh *et al.* and by Kim *et al.* (Fe_3O_4 commercial nanopowder) afforded the highest yield (entry n°1, 3). Despite more favourable conditions (temperature or equivalents of hydrazine) than those we applied, they exhibited lower transformation rates. The low dispersion of these systems is likely the main cause. Even by taking into account the high

temperature of reaction, the system based on tris(acetylacetonato)iron(III) ($\text{Fe}(\text{acac})_3$) complexes and assisted by microwaves, exhibited a high transformation rate and decent *p*-CAN yield (97%). Cobalt complexes (Co (II) Phthalocyanines) (entry n°4) were also among the most active catalysts among non-precious metal-based systems but afforded a lower yield (88%). The industrial potential of this type of catalysts, *i.e.* complexes, could be greatly hampered by practical limitations. Our FeO_x/ACF catalyst has shown to be the most selective and ranks among the best in terms of activity (entry n°7).

Table 4.1. Comparison of the results obtained with the FeO_x/ACF in the CTH of *p*-CNB, to previously reported catalysts.

N°	Catalyst	d^A (nm)	RA ^B /EQ/ Solvent	T (K)	$-\mathbf{R}_{\text{average}}^C$ ($\text{mol}_{\text{NC}} \cdot \text{mol}_{\text{M}}^{-1} \cdot \text{s}^{-1}$)	$\mathbf{X}_{p\text{-CNB}}$ (%)	$\mathbf{S}_{p\text{-CAN}}$ (%)	$\mathbf{Y}_{p\text{-CAN}}$ (%)	Ref.
1	Fe-phen./C-800	20–80	$\text{N}_2\text{H}_4/4/$ THF	373	2.8×10^{-3}	100	99	99	78
2 ^D	$\text{Fe}_3\text{HO}_8 \cdot 4\text{H}_2\text{O}$	< 63 $\times 10^3$	$\text{N}_2\text{H}_4/1.5/$ THF:H ₂ O (1:1)	351	1.0×10^{-3}	100	98	98	68
3	Fe_3O_4	< 50	$\text{N}_2\text{H}_4/6/$ EtOH	353	3.1×10^{-4}	-	-	99	69
4 ^E	$\text{Fe}(\text{acac})_3$	6	$\text{N}_2\text{H}_4/1.8/$ THF:H ₂ O (1:1)	423	1.7×10^{-1}	-	-	97	123
5	Cobalt(II) Phthalocyanin	NA	$\text{N}_2\text{H}_4/2/$ Ethylene glycol	343	2.8×10^{-2}	> 99	~ 88	88	72
6	CeO_2	$\sim 39^F$	$\text{N}_2\text{H}_4/4/$ EtOH:H ₂ O (1:1)	353	8.0×10^{-4}	100	76	76	75
7	FeO_x/ACF	~ 2	$\text{N}_2\text{H}_4/3/$ EtOH	333	1.7×10^{-2}	99.9	100	99.9	This work

^A The diameter *d* corresponds to the average diameter given in the references or the approximate observed range.

^B RA = reducing agent. EQ = equivalents

^C The average transformation rate was calculated with equation (3.4) for the reaction time required to reach the conversion associated the highest yield given in the references.

^D Internal mass transfer limitations were ruled out using NPs of greater size (> 80 , and $> 100 \mu\text{m}$).

^E *o*-CNB was tested rather than *p*-CNB. The microwave method was employed.

^F Equivalent sphere diameter, calculated from cylinder-shaped nanorods of $\sim 10 \times 150 \text{ nm}$.

When looking at the concentration profiles during the CTH of *p*-CNB over the FeO_x/ACF catalyst, the desired *p*-CAN product is formed directly (**Figure 4.8A**) and no intermediates were detected in the course of the reaction. In contrast, intermediates (nitroso-, azo- and azoxyarenes) were found using the CoO_x/ACF catalyst. In the latter part of the reaction, these intermediates are slowly converted to *p*-CAN (**Figure 4.8B**).

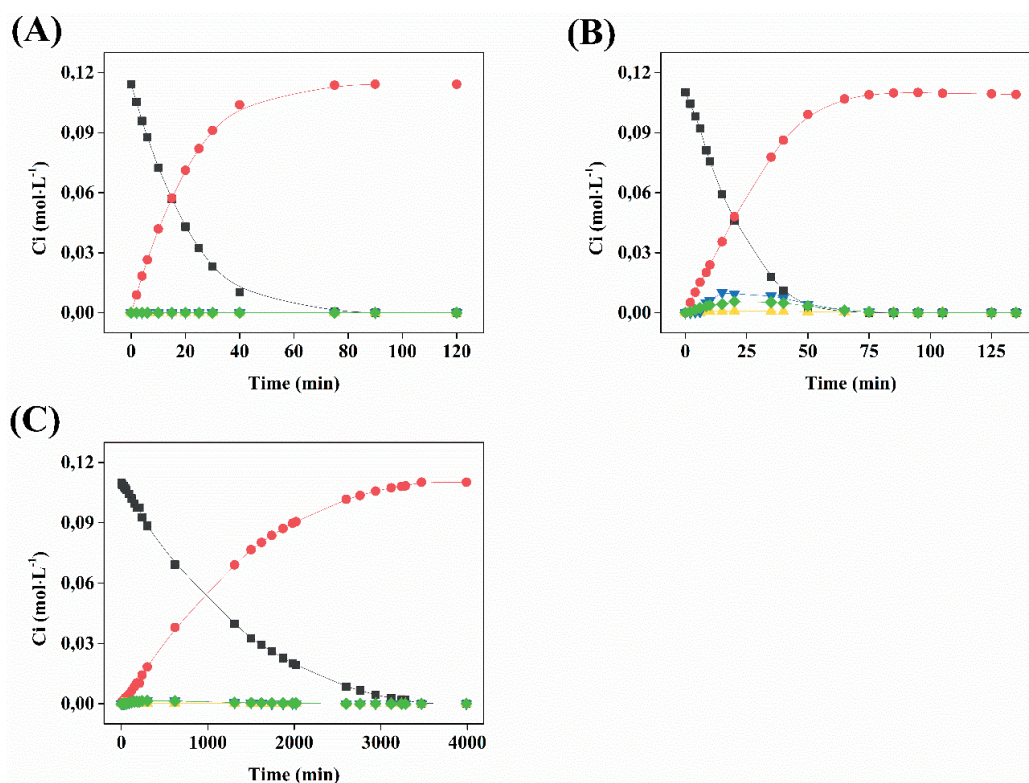
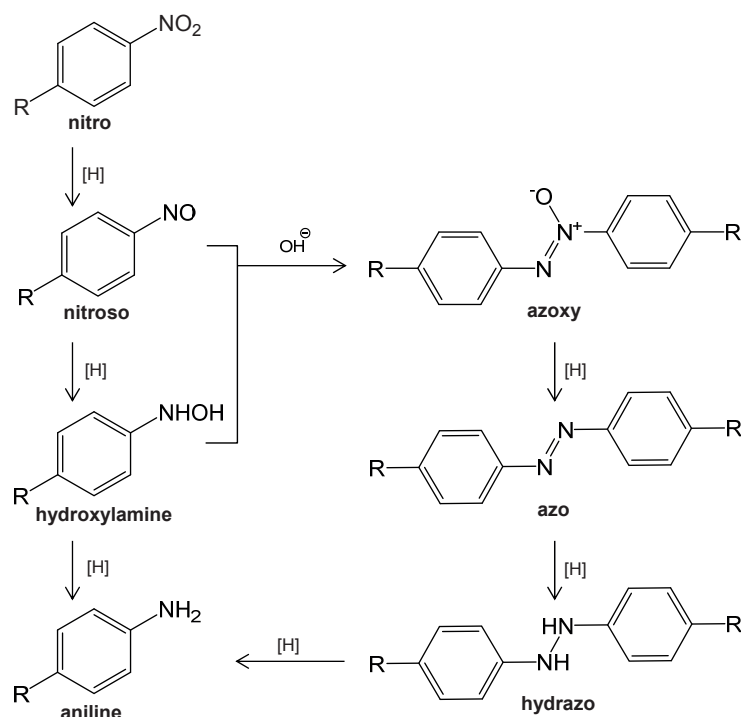


Figure 4.8. Concentration vs reaction time for the CTH of *p*-CNB to *p*-CAN over FeO_x/ACF (A), CoO_x/ACF (B) and NiO_x/ACF (C) (■ *p*-CNB; ● *p*-CAN; ▲ *p*-chloroazobenzene; ▼ *p*-chloroazoxybenzene; ◆ *p*-chloronitrosobenzene; ○ aniline). Reaction conditions: $C_{p\text{-CNB},0} = 1.2 \times 10^{-1} \text{ mol} \cdot \text{L}^{-1}$; 100 cm³ of EtOH; T = 333 K; molar ratio N₂H₄:*p*-CNB = 3; molar ratio *p*-CNB:M = 50. Metal loading (wt.%): (Fe, Co, Ni) = 6.1, 6.0, 6.2, respectively.

These observations are in line with the widely accepted reaction network for nitrobenzene hydrogenation,¹⁶ implying two possible routes, *i.e.* direct and condensation (**Scheme 4.1**).



Scheme 4.1. Reaction network for the reduction of nitroaromatic compounds.

Although the full mechanism of heterogeneous CTH of nitroarenes over transition metal oxides remains unclear, one can affirm that H-transfer from hydrazine to the substrate in a catalytic cycle is associated with metal transition from one oxidation state to another ($\text{Fe(III)} \leftrightarrow \text{Fe(II)}$, $\text{Co(III)} \leftrightarrow \text{Co(II)}$, etc.).^{124,125} Since the most likely redox couple for Ni is $\text{Ni(II)} \leftrightarrow \text{Ni(I)}$, this difference may explain the lower activity of the NiO_x/ACF . We also found that commercial highly crystalline Co_3O_4 ($\text{Co}^{\text{III}}_2\text{O}_3 \cdot \text{Co}^{\text{II}}\text{O}$) NPs are essentially catalytically inactive in the CTH of nitroarenes with hydrazine. A *p*-CNB conversion of $\sim 1\%$ was detected after 3 hours reaction over the as-received Co_3O_4 NPs. Over reduced/passivated Co_3O_4 NPs after the same reaction time, however, result in a conversion of $> 75\%$ of *p*-CNB was obtained despite the loss of surface available during reduction. The SEM and TEM images in **Figure 4.9** demonstrate the occurrence of sintering during the reduction by comparing the commercial NPs before (**A,C**) and after (**B,D**) the procedure.

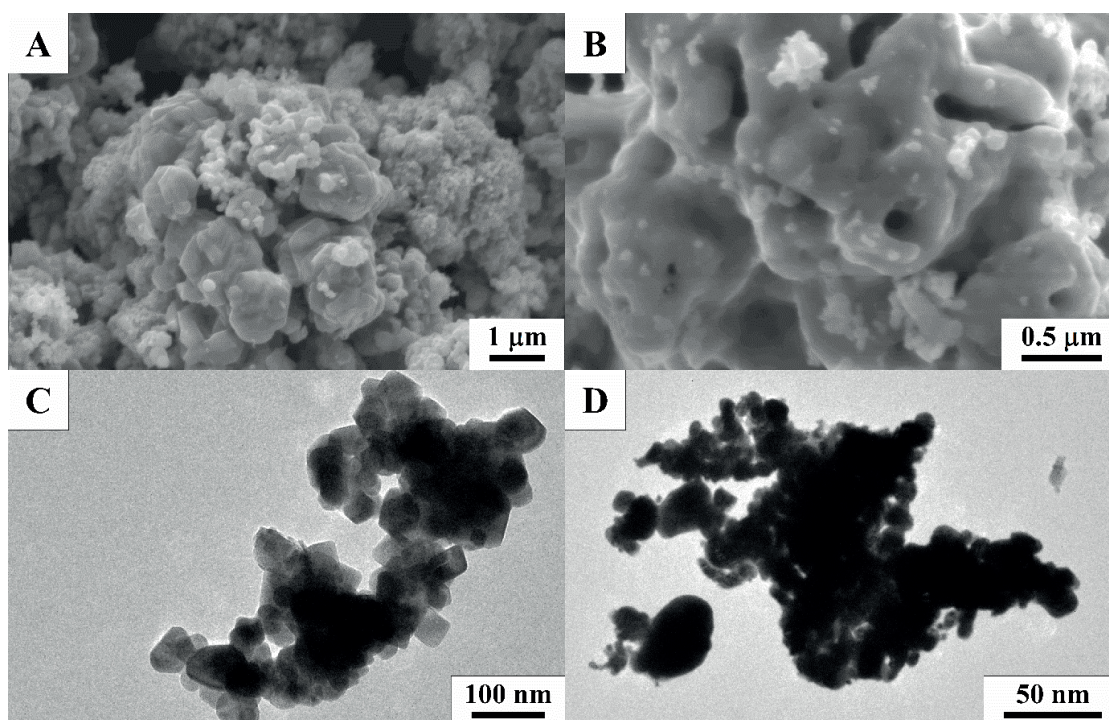


Figure 4.9. SEM images of (A) as-received and (B) reduced Co_3O_4 NPs. TEM micrographs of (C) as-received and (D) reduced Co_3O_4 NPs.

The changes of position and shape of the Co_3O_4 NPs XPS spectrum after reduction (Figure 4.5D) suggest that a mixture of Co_2O_3 and CoO phases is formed under exposure to air. The higher ability of these phases to operate phase transition compared to Co_3O_4 is probably the reason of their higher catalytic activity in the CTH of *p*-CNB. Despite hydrazine is known for being a mild reducing agent, control experiments were performed to verify that metallic cobalt is inactive in the CTH of nitroarenes. The *p*-CNB transformation into *p*-CAN was suppressed during the first 30 minutes of reaction by replacing the CoO_x/ACF catalyst by Co/ACF catalyst. The creation of metallic NPs was ensured by replacing the inert gas by a 17% v/v H_2/Ar mixture during the dwell of the thermal treatment and by the implementation of an liquid in-situ reduction step (1 hour; $T = 423 \text{ K}$; $P_{\text{H}_2} = 10 \text{ bar}$) before the start of the reaction. The activity then raised to a level three times lower than the usual

transformation rate. Moreover, exposing this catalyst to air for 16 hours enabled during a subsequent catalytic test the recovery of an activity closed to the usual transformation rate.

Hydrazine stability

A special experiment was carried out to investigate the influence of hydrazine concentration on the catalytic response. It was found that if stoichiometric amounts of the reactants were used, ~18% of hydrazine was lost due to its catalytic decomposition over FeO_x/ACF (N₂H₄ → N₂ + 2H₂). This value was limited to 7% over the CoO_x/ACF catalyst. Therefore, 3 moles of reducing agent per mole of substrate were normally used through the study. The hydrogen produced via hydrazine decomposition played no role in the reduction of *p*-CNB. The estimated hydrogen bulk concentration in ethanol was 50 times lower than hydrazine concentration. Moreover, a control experiment with the iron oxide-based catalyst and molecular hydrogen at 8.5 bar (P_{tot} = 10 bar) showed the absence of *p*-CNB reduction, despite a *ca.* 10-fold higher concentration of H₂ in ethanol (3.5×10⁻² M, corresponding to 22% of N₂H₄·H₂O initial concentration) compared to the H₂ solubilized after 80% conversion of *p*-CNB (3.7×10⁻³ M) using N₂H₄·H₂O as reducing agent (molar ratio N₂H₄:*p*-CNB = 1.5).

Apparent activation energy and reaction orders

Kinetic data were acquired using FeO_x/ACF, the most active of the MO_x/ACF catalysts. Raising hydrazine concentration from 3 to 6 equivalents resulted in an increase of the transformation rate, indicating a positive partial reaction order with respect to this reactant. The influence of *p*-CNB concentration on the reaction rate was evaluated (T = 333 K) by varying the concentration from 0.008 to 0.06 M in the presence of a large excess of hydrazine (> 10 equivalents). The *p*-CNB partial reaction order was found to be ~0.6. The apparent activation energy, *E_a* was estimated in the temperature range of 313 ≤ T ≤ 353 K (**Figure 4.10**). The obtained result (*E_a* = 67.3 kJ·mol⁻¹) points out the absence of mass transfer

limitations in the system under the applied conditions. This value is consistent with the $E_a = 75.7 \text{ kJ}\cdot\text{mol}^{-1}$ reported for 4-nitrotoluene reduction by hydrazine over Fe(III) oxide hydroxide ($318 \leq T \leq 348 \text{ K}$).⁶⁸

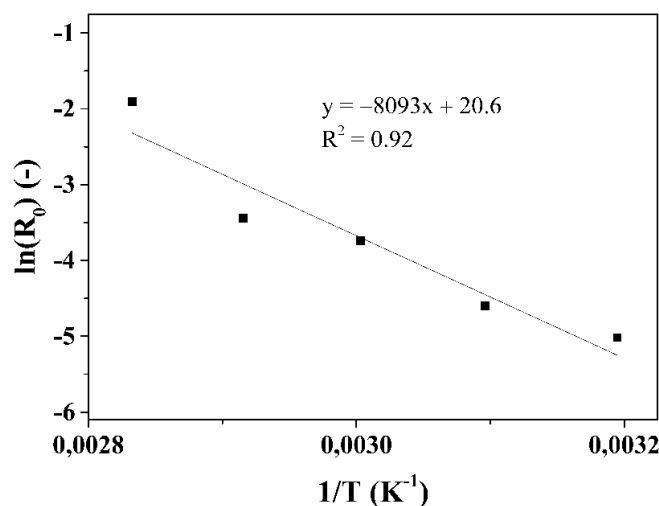


Figure 4.10. Arrhenius plot for the CTH of *p*-CNB by hydrazine to *p*-CAN. Reaction conditions: $C_{p\text{-CNB},0} = 1.2 \times 10^{-1} \text{ mol}\cdot\text{l}^{-1}$; 100 cm^3 of EtOH; $T = 313\text{--}353 \text{ K}$; molar ratio $\text{N}_2\text{H}_4:p\text{-CNB} = 3$; molar ratio $p\text{-CNB}:M = 50$. Fe metal loading (wt.%) = 6.0.

Catalysts stability

The stability of the FeO_x/ACF and CoO_x/ACF catalysts was evaluated. The structured ACFs-based catalysts were fixed on the stirrer and did not require any filtration allowing its easy recovery. The leaching of loosely attached Fe_2O_3 NPs ($\sim 5 \text{ wt.}\%$ of Fe lost) was identified during the first catalytic run with the FeO_x/ACF . This inconvenience could be overcome by catalyst conditioning (placing the catalyst in the reaction mixture for 30 min before the use). After each run, the catalyst was thoroughly washed with ethanol. The activity of the pre-conditioned catalyst (see **Figure 4.11A**) remained over 4 consecutive runs ($-R_0 \approx 0.03 \text{ mol}_{p\text{-CNB}}\cdot\text{mol}_{\text{Fe}}^{-1}\cdot\text{s}^{-1}$), whereas the selectivity to the desired aniline was 100% up to full conversion, the *p*-CNB being exclusively transformed into *p*-CAN. The specific activity

over the CoO_x/ACF catalyst gradually decreased during the stability experiment and finally reached 25% of its initial value (**Figure 4.11B**). The *p*-CAN selectivity at 99% conversion remained at 100%. Treatment of the used catalyst at 473 K and under vacuum afforded the extraction of a yellowish viscous extract. It might indicate the strong adsorption of reactant on the actives, presumably the condensation intermediates. A cumulative TON of 192 $\text{mol}_{p\text{-CNB}} \cdot \text{mol}_{\text{Fe}}^{-1}$ in 3 h was obtained for the 4 runs over the FeO_x/ACF by considering a conversion of 95%.

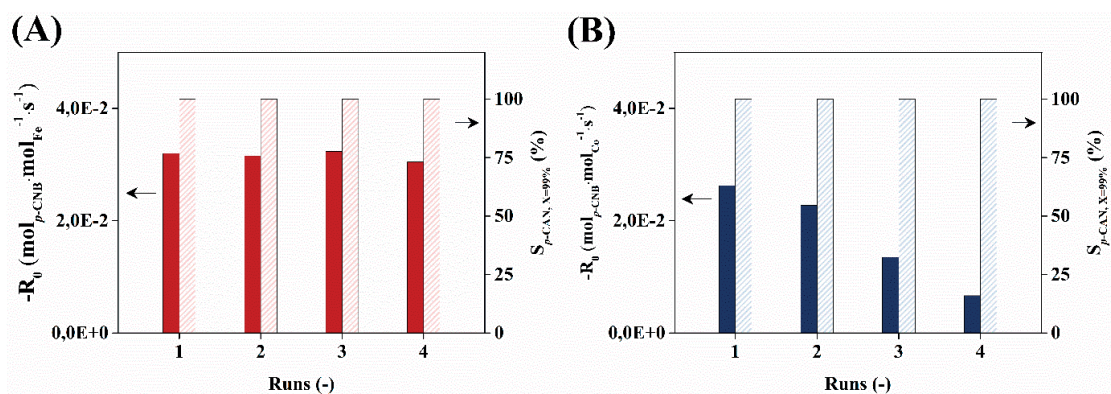


Figure 4.11. CTH of *p*-CNB with hydrazine over (A) FeO_x/ACF and (B) CoO_x/ACF for 4 successive runs (after pre-condition step): catalyst activity (solid bars) and maximum *p*-CAN yield (hatched bars). *Reaction conditions:* $C_{p\text{-CNB},0} = 1.2 \times 10^{-1} \text{ mol} \cdot \text{l}^{-1}$; 100 cm^3 of EtOH; $T = 333 \text{ K}$; molar ratio $\text{N}_2\text{H}_4:p\text{-CNB} = 3$; molar ratio $p\text{-CNB}:M = 50$. Metal loading (wt.%) of Fe, Co = 5.6, 4.0, respectively.

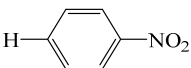

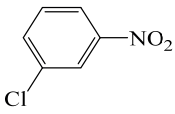
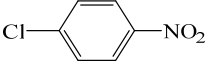
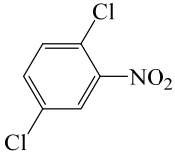
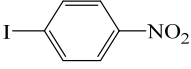
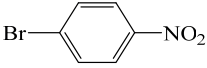
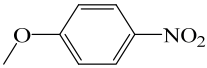
Reaction scope

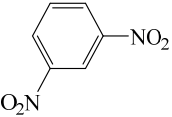
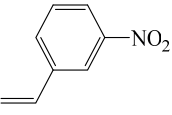
The reaction scope was evaluated over the FeO_x/ACF catalyst using a variety of functionalized nitroarenes (**Table 4.2**). For the majority of the tested substrates the reaction was found to be highly chemoselective ($S = 95\text{--}100\%$). Under the chosen conditions, the time to reach 95% conversion of nitroarene varied from 15 to 155 min depending on the substituent nature and position.

The catalytic reduction by hydrazine could not be applied for substrates containing aldehyde, ketone and carboxylic groups, since they easily react with hydrazine resulting in hydrazones and hydrazinium salts, respectively.⁶³

In the case of *m*-nitrostyrene, the selectivity in *m*-aminostyrene (~82%) at 95% conversion was obtained after 1.1 h. The detected by-products were *m*-ethylnitrobenzene (~4.4%) and *m*-ethylaniline (~13.4%). The lower selectivity in this case can be explained by the formation of intermediate diimide from hydrazine, which is known to be responsible for the reduction of double carbon-carbon bonds.¹²⁶

Table 4.2. CTH of functionalized nitroarenes (NC) over FeO_x/ACF. *Reactions conditions:* C_{NC,0} = 1.2 × 10⁻¹ mol · l⁻¹; 100 cm³ of EtOH; T = 333 K; molar ratio N₂H₄:NC = 3; molar ratio NC:Fe = 50. Fe loading (wt.%) = 5.6.

Substrate (NC)	Formula	Reaction time, X _{NC} = 95% (min)	-R ₀ , ×10 ² (mol _{NC} · mol _{Fe} ⁻¹ · s ⁻¹)	Selectivity, X _{NC} = 95% (%)
nitrobenzene		90	1.6	100
<i>p</i> -nitrotoluene		105	2.2	100
<i>m</i> -chloronitrobenzene		55	2.8	100
<i>p</i> -chloronitrobenzene		40	3.3	100
1,4-dichloro-2-nitrobenzene		15	9.3	100
<i>p</i> -iodonitrobenzene ⁴		155	0.2	95
<i>p</i> -bromonitrobenzene		40	3.7	100
<i>p</i> -nitroanisole		130	1.1	100

Substrate (NC)	Formula	Reaction time, $X_{NC} = 95\%$ (min)	$-R_0, \times 10^2$ ($\text{mol}_{NC} \cdot \text{mol}_{Fe}^{-1} \cdot \text{s}^{-1}$)	Selectivity, $X_{NC} = 95\%$ (%)
<i>m</i> -dinitrobenzene		25	5.7	98
<i>m</i> -nitrostyrene ⁴		68	1.2	82

⁴ Substrate - 0.03 M, *m*-NS:Fe = 20.

4.3.3 Reduction of *m*-nitrostyrene

The excellent results obtained with the FeO_x/ACF during reaction scope prompted us to study further the CTH of *m*-nitrostyrene whose *m*-VA yield was disappointing (~80%). This compound is often taken as a model for hydrogenation of complex nitroaromatics with multiple substituted groups in which the preservation of the C=C double bond, easily reducible, during reduction is the main concern. The results presented in **Figure 4.12** demonstrate that FeO_x/ACF is more active than CoO_x/ACF in the CTH of *m*-nitrostyrene using hydrazine, but is less selective toward desired *m*-vinylaniline (*m*-VA) product.

Considerable improvements in the yield of *m*-VA were obtained using ACFs pre-treated by HNO₃ as supports for the NPs catalysts (**Figure 4.12**). The pre-treatment was found to give more active Fe and Co-based ACFs catalysts by 12 and 29%, respectively. The highest *m*-VA yield of 99.4 % was obtained over the CoO_x/ACF_{HNO3}.

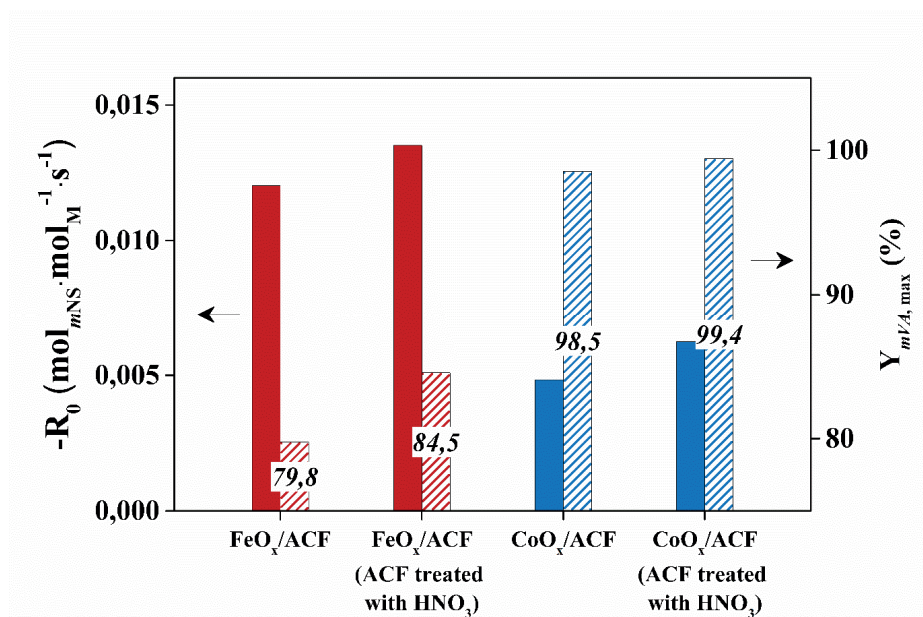


Figure 4.12. CTH of *m*-nitrostyrene (*m*-NS) by hydrazine over FeO_x/ACF and CoO_x/ACF, with and without HNO₃ pre-treatment of the ACFs support: catalyst activity (solid bars) and maximum *m*-vinylaniline yield (hatched bars). *Reaction conditions:* $C_{m-NS} = 0.032 \text{ mol} \cdot \text{l}^{-1}$; 100 cm^3 of EtOH; $T = 333 \text{ K}$; molar ratio $\text{N}_2\text{H}_4/m\text{-NS} = 3$; molar ratio $m\text{-NS}:M = 20$. Metal loading (wt.%): (Fe/ACF, Fe/ACF_{HNO3}, Co/ACF, Co/ACF_{HNO3}) = 6.5, 6.7, 4.3, 5.3, respectively.

The oxygen-containing surface groups of the carbonaceous supports can impact the catalytic performance in several ways. The interaction of the metal precursor with the support (distribution, mobility, resistance to coagulation) vary according to the number of groups, which can affect the dispersion. Moreover, the ability to electronically influence the catalytic properties of active NPs has been attributed to these groups in several studies.^{97,106,107} The changes in activity, although minor, and the increase in selectivity due to the pre-treatment of the ACFs prompted us to characterize the best of the two catalysts, *i.e.* CoO_x/ACF_{HNO3}. To assess possible variation of NPs size or chemical composition within the catalyst, compared to CoO_x/ACF, STEM-HAADF imaging has chosen as a characterization technique.

STEM-HAADF of the $\text{CoO}_x/\text{ACF}_{\text{HNO}_3}$ catalyst

The morphologies of NPs deposited on as-supplied and HNO_3 pre-treated ACF are different. No Co oxide NPs could be observed by STEM in the $\text{CoO}_x/\text{ACF}_{\text{HNO}_3}$ (**Figure 4.13A**) on the FEI Tecnai Osiris, despite EDX mapping showing cobalt being well distributed throughout the carbon surface (**Figure 4.13B**). It is noteworthy that when Ni-based NPs were deposited on pre-treated ACF, they still visible and their dispersion negligibly decreased (1.4 nm \rightarrow 1.3 nm). The absence of discernible particles indicates the formation of NPs below the detection limit (< 0.5 nm) or that consist of a higher oxygen-lattice concentration. The first hypothesis was ruled out on the basis of the supplementary imaging of the $\text{CoO}_x/\text{ACF}_{\text{HNO}_3}$ catalyst performed with an aberration-corrected microscope (FEI Titan Themis). Nanoparticles ranging from ~ 1 – 3 nm were revealed (**Figure 4.13C**).

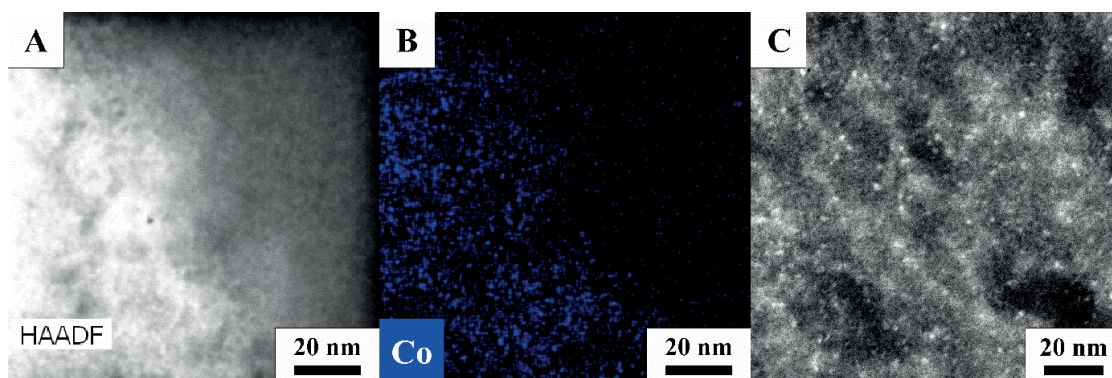


Figure 4.13. STEM-HAADF image of $\text{CoO}_x/\text{ACF}_{\text{HNO}_3}$ (**A**), corresponding Co EDX mapping (**B**) and STEM-HAADF imaging of $\text{CoO}_x / \text{ACF}_{\text{HNO}_3}$ on the FEI Titan Themis (**C**). CoO_x NPs appear bright on the dark background (ACF support). Co loading (wt.%) = 5.3.

Modelling of STEM-HAADF signal of CoO_x NPs

The scattered electrons reaching the HAADF detector are typically incoherent electrons that are elastically scattered via Rutherford's mechanisms from Coulombic interaction with the nuclei of the sample material. As such, the scattering angle and thus intensity of the HAADF STEM images are proportional to the atomic number of species in sample. The contrast in HAADF STEM images arises from regions in the specimen with differing Z (atomic number),

thickness and density. This type of imaging is often referred to as Z-contrast images and a very simplified interpretation of the image intensity (I) is given by the following relation,

$$I \sim Z^2 t \quad (4.1)$$

where t is the thickness. A strong variation in sample thickness or porosity can pose challenges for proper interpretation. Models have been derived from the above relation and discussed by Crozier and Kirland.^{127,128} Also, it is known from the early works of Pennycook *et al.*¹²⁹ that single atoms of heavy metals, *e.g.*, Pt or Au, can be observed on thin, low-Z supports, which is due to the high signal to background ratios of such systems. However, precise quantification of the image intensity using a rigorous multi-slice calculation would not obtain a better understanding of the structure of the NPs in MO_x/ACF catalysts due to the limitations on detectable size as well as fact that there are many unknowns about ACFs support which would perturb the calculation, *e.g.*, density variations, oxides layers, etc. Instead, a simplified model that calculates the signal to background ratio (SBR) for monolayer of Co atoms sitting on a thick carbon support is implemented. Though simple, it provides rough estimates and trends in data and are an effective means to corroborate the catalytic activity data set presented in this chapter. For the analysis, we assume that the SBR for HAADF STEM imaging of catalysts has the following relations,

$$SBR = \frac{I_m}{I_s} \quad (4.2)$$

$$I_x = I_0 N_x \sigma_x \quad (4.3)$$

where I_m is the scattered intensity on the HAADF from the catalyst, I_s is the intensity from the support, N is the number of atoms per unit volume and σ is the scattering cross-section. For high-angle scattering, the scattering cross-sections increase with Z^n , where n is between 1.5 and 2. We can assume that an average Z for the support and catalyst materials

and that the number density of atoms is similar between the support and catalyst layer. Setting $n = 1.7$, we can rewrite the SBR according to Kirkland as,¹²⁸

$$SBR = \frac{1}{t_s N_v^{1/3}} \left(\frac{Z_m}{Z_s} \right)^n \quad (4.4)$$

where Z_m and Z_s are the average Z of the catalyst and support, respectively, t_s is the thickness the support and N_v is the atomic density of the support. We assumed that the ACFs support specimen has a pore volume of $1 \text{ cm}^3 \text{ g}^{-1}$, a true density close to activated carbon (1.6 g cm^{-3})¹³⁰ and is roughly 60 nm thick (average thickness measured experimentally). The apparent density is therefore 0.6 g cm^{-3} . Two different nanocatalyst compositions, pure Co metal and a cobalt oxide with a stoichiometry close to of Co_2O_3 (average $Z \sim 15.6$), were addressed as specific cases. Inputting the experimental parameters for the nanocatalyst composition, we calculate the SBR as 0.069 and 0.026 respectively. These SBR values will be used as an estimate to determine whether the nanoparticles observed in HAADF images are pure Co or a cobalt oxide.

Figure 4.14 shows a HAADF image of the $\text{CoO}_x/\text{ACF}_{\text{HNO}_3}$ catalyst, taken on the Titan 60-300 Themis equipped with a double aberration corrector and high sensitivity energy dispersive spectroscopy system. Numerous circular speckles, with a size of 1–3 nm, are faintly visible over the background of the thick ACFs support. We interpret these small features as being the Co based catalyst nanoparticles.

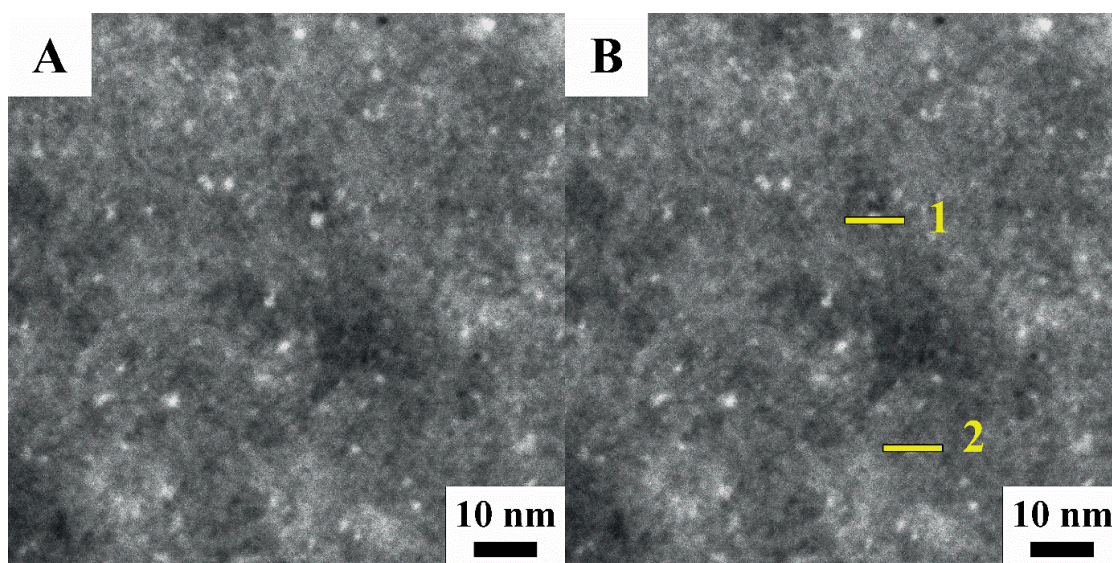


Figure 4.14. (A) High magnification HAADF STEM image of the Co complexes on ACFs of $\text{CoO}_x/\text{ACF}_{\text{HNO}_3}$ catalyst. (B) The same image as (A) with 2 yellow rectangles 1 and 2 across two different nanoparticles indicating the regions used for the intensity line plots shown in Figure 4.16A and B, respectively.

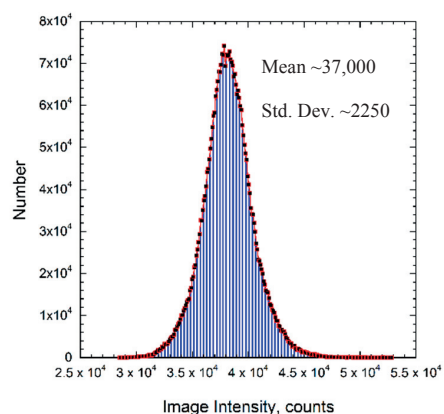


Figure 4.15. Histogram analysis of the HAADF intensity in Figure 4.14. The mean intensity is a rough estimate of the background intensity from the ACFs support and standard deviation estimates the variation in the intensity.

Given the variation in the ACFs support thickness that is apparent in HAADF signal, we can make an estimate of the SBR needed to reliably discern a catalyst particle of over the support with following relation from Crozier,¹²⁷

$$I_{\min} = 2\sigma(B)$$

$$SBR_{\min} = 2\sigma(B)/\mu(B) \quad (4.5)$$

where $\sigma(B)$ is the standard deviation and $\mu(B)$ the mean HAADF intensity of the support. For the TEM samples with 60 nm thick ACFs support used in this study, the minimum SBR is 0.12. This means monolayers, *i.e.* singles of atoms of cobalt and molecules of cobalt oxides, cannot be detected. Furthermore, the minimum cluster sizes of Co and cobalt oxide detectable under these experimental conditions are ~ 0.4 and 1 nm, respectively.

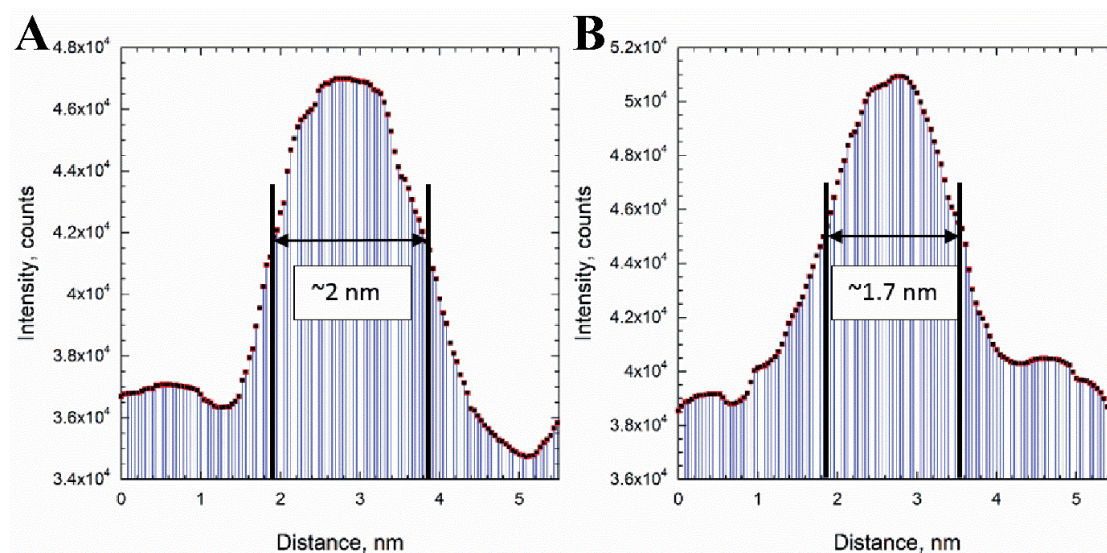


Figure 4.16. Line plots across identified nanoparticles shown in **Figure 4.14B**, identified as **(A)** 1 and **(B)** 2. The diameter the nanoparticles is taken as FWHM of HAADF intensity.

The nanocatalysts in **Figure 4.14** are weakly contrasted over the background intensity of the ACFs support. Even for 1 nm size particles, the heavy metal atoms of Co should have much stronger SBR than observed. Using the line plots in **Figure 4.16** to quantitatively evaluate the intensity of the particles, some notable trends can be observed. The effective SBR for different nanoparticles was determined using equation (4.4) and the SBR was scaled by atomic density and diameter of the nanoparticle. For example, a 2 nm diameter Co NP, having a density of $8.9 \text{ g}\cdot\text{cm}^{-3}$ and atomic density of $91 \text{ atoms}\cdot\text{nm}^{-3}$, would have a SBR of

0.62. While a cobalt oxide particle (Co_2O_3) of the same diameter, having an effective density of $6.11 \text{ g}\cdot\text{cm}^{-3}$ and atomic density of $94 \text{ atoms per nm}^3$, has a SBR of 0.25. By analysing the HAADF image in **Figure 4.14** and the intensity line plots in **Figure 4.16**, the experimental SBR for is on average 0.26. The experimentally observed intensities for the nanoparticles suggest that nanocatalysts are metal oxides rather than pure Co, and possibly Co_2O_3 .

Energy dispersive spectroscopy investigations of the samples also confirms a high concentration of oxygen in the samples. **Figure 4.17** shows a spectrum taken over an area of $200 \times 200 \text{ nm}^2$. The peaks from carbon, sulphur, chlorine and silicon come from the ACFs support which typically comprise these elements in commercial fibres. Fe is a typical impurity in Co containing precursors. Cu and Al peaks come from the TEM grid support and sample holder. The largest peak besides carbon is oxygen. This element is contained in the ACFs as received but not in concentrations large enough to explain the intense peak in the EDX spectrum **Figure 4.17**. The fact that analysis of the HAADF images suggest NPs consisting in cobalt oxide complexes may explain the larger than expected oxygen peak in the EDX spectrum.

To verify that the nanocatalysts contain oxygen, high-resolution STEM-EDX mapping was conducted (**Figure 4.18**). It is clear from comparing **Figure 4.18A** and **C** that the nanoparticles contain Co. However, the correlation of the oxygen EDX map to the nanoparticles is less obvious. The oxygen characteristic X-ray signal in the elemental map appears to be slightly higher over the background in the regions where there are NPs but the signal difference is not significant. Also, the contrast in the HAADF image of **Figure 4.18A** looks quite different from **Figure 4.14A**, the nanoparticles being more prominent and having higher signal-to-background contrast. The images in **Figure 4.18** are an integrated average from a scan acquisition of 45 min at a beam current of 1 nA. The effective dose in the maps and images of **Figure 4.18** is 3 orders of magnitude more than the images shown in **Figure**

4.14. It is likely that beam induced chemistry in TEM altered the material, changing the composition and structure of the NPs. Beam-induced effects may be unavoidable when long acquisition times and intense beams are required for statistically relevant EDX data, and they need to be identified and properly interpreted.

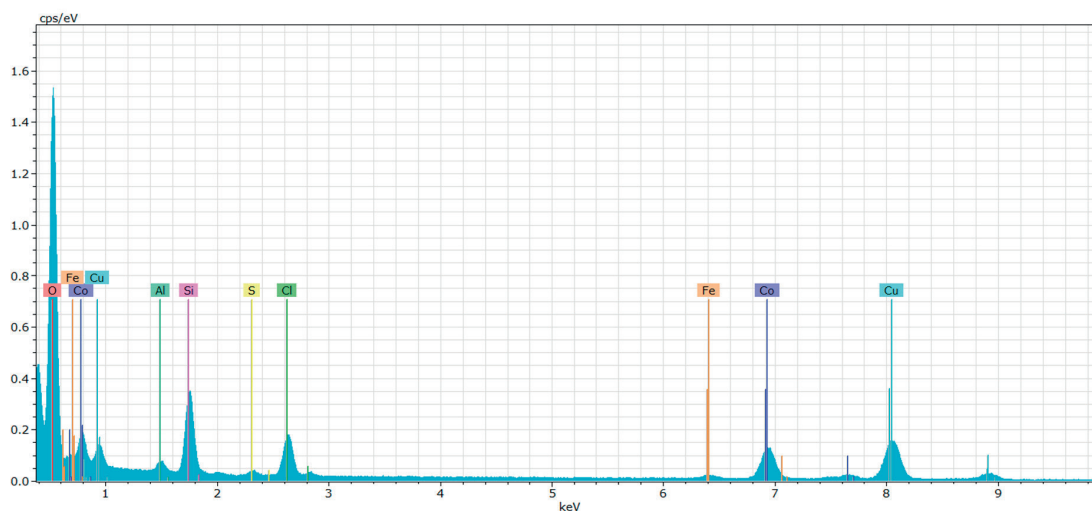


Figure 4.17. EDX spectrum of $\text{CoO}_x/\text{ACF}_{\text{HNO}_3}$ catalyst.

To investigate further the origin of the increased contrast, we analysed the nanoparticles in the HAADF images of **Figure 4.18**. **Figure 4.19** shows the intensity variation across two different nanocatalysts (the catalyst positions are marked by yellow lines in **Figure 4.18B**). The SBR ratios for NPs 1 and 2 are 0.65 and 0.59, respectively. These SBRs correspond to pure Co nanoparticles and are much higher than SBR values prior to the EDX scans.

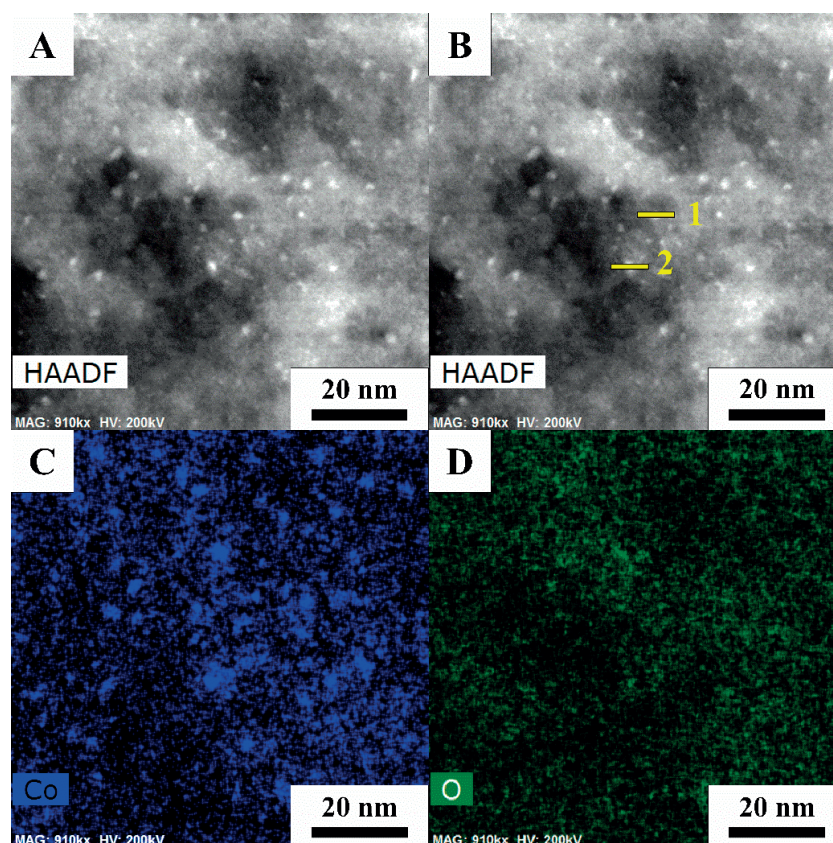


Figure 4.18. (A) HAADF STEM image of $\text{CoO}_x / \text{ACFHNO}_3$ after 45 minutes of EDX scanning using beam current of 1 nA (B) same image as (A) showing the regions used for the intensity line profile plots shown in **Figure 4.19**. EDX elemental mapping of (C) Co and (D) O.

Knock-on damage from the 200 KeV electron beam can displace oxygen atoms from the cobalt oxide nanocatalysts, reducing them. In combination with the beam heating due to the high currents (1 nA) and absorption by thick ACFs support, the reduced nanocrystallites with dispersed Co atom cluster can sinter into the observed dense Co nanocatalysts. Though this alteration in composition and structure is a supposition, it is conceivable to occur under similar mechanisms as thermal treatments under reducing atmosphere. While the EDX data does contain beam induced artefacts, they still give further credence that the nanocatalysts observed in **Figure 4.14** are indeed a cobalt oxide complex.

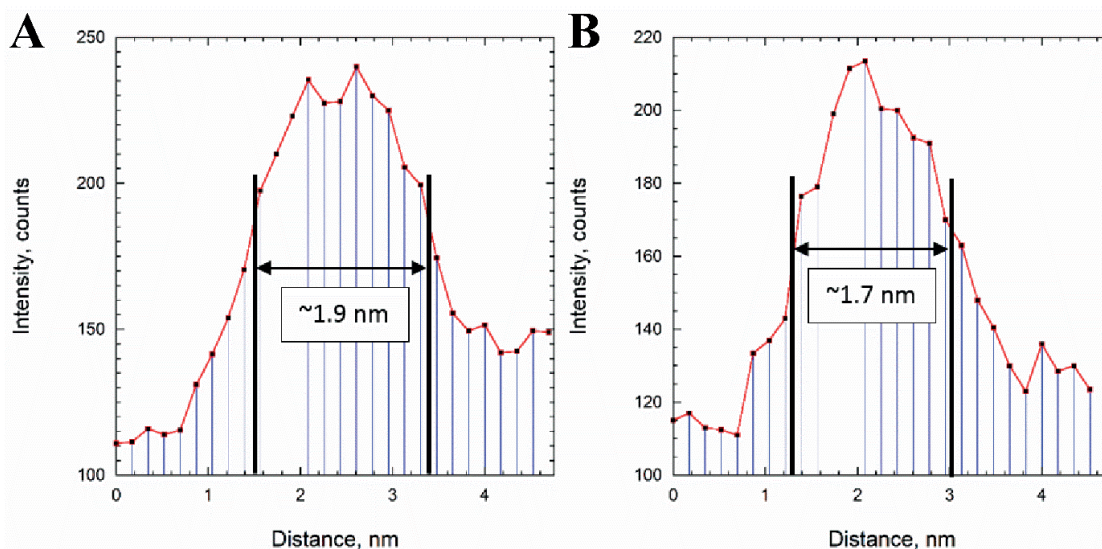


Figure 4.19. Line plots across identified nanocatalysts shown in **Figure 4.18B**, identified as **(A)** 1 and **(B)** 2. The diameter of the nanoparticles is taken as the FWHM of the HAADF intensity. Note that since the image is 8-bit, the HAADF intensity is scaled to 255 counts.

In summary, two specific cases (Co and Co_2O_3) were addressed with a simplified model and compared the experimental data acquired by HAADF-STEM for the $\text{CoO}_x/\text{ACF}_{\text{HNO}_3}$ catalyst. The NPs consist of cobalt oxides, presumably with a higher concentration of lattice oxygen compared to the NPs of CoO_x/ACF catalyst, which explains the higher difficulty to visualize them.

4.4 Conclusions

Structured catalysts featuring highly-dispersed non-precious metal (Fe, Co, Ni) oxide NPs stabilized within a super-microporous network of activated carbon fibres (ACFs) have been developed and used for chemoselective reduction of substituted nitroarenes using hydrazine as a hydrogen source. The catalyst morphology was controlled over multiple levels from the nano-designed active phase up to the macro-structure of the ACFs support.

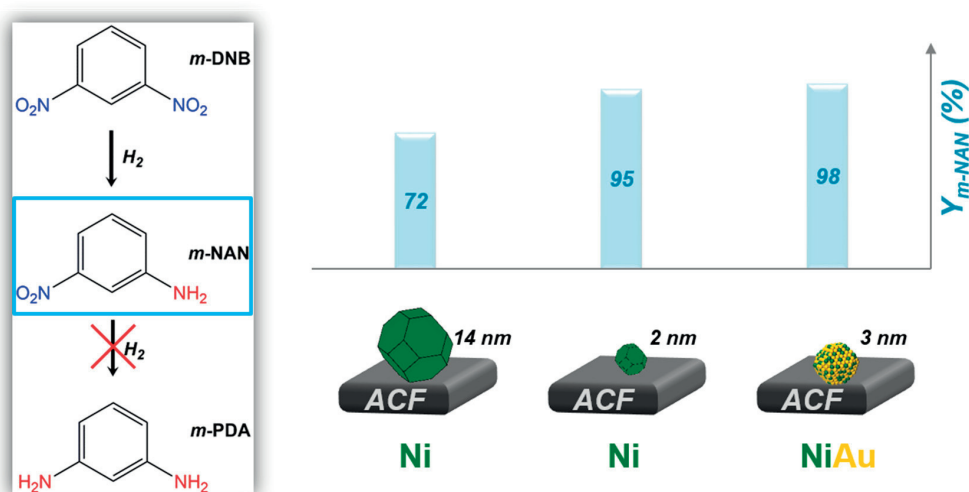
The main advantages of the ACFs structured supports include the facile formation of extremely small (< 2nm) NPs and their stabilization within a micro-porous network which prevents their agglomeration. Moreover, the micro-sized diameters of the carbon filaments in combination with their slit-type short micropores eliminate any mass-transfer limitations allowing a high selectivity.

The FeO_x/ACF catalyst allows almost quantitative transformation of a series of nitroarenes to corresponding anilines.

The challenging reduction of *m*-nitrostyrene containing an easily reducible vinyl-group was achieved under mild conditions (T = 333 K, P = 1 atm) with to a near-quantitative yield (99.4%) of *m*-vinylaniline using hydrazine hydrate and the CoO_x/ACF_{HNO3} catalyst.

This catalytic systems are suitable for batch as well as flow-mode reactors. Therefore, we anticipate that the catalysts presented in this study will offer new approaches for the synthesis of aryl amines containing C=C double bonds.

Highly Selective Immobilized Bimetallic Ni-Au Nanoparticle Catalyst for the Partial Hydrogenation of *m*-dinitrobenzene



This chapter is based on the following publication:

“Highly selective immobilized bimetallic Ni-Au nanoparticle catalyst for the partial hydrogenation of *m*-dinitrobenzene” (Applied Catalysis A: General, submitted in February 2017),

Abstract

Transition metal nanoparticles (NPs) are extensively used as catalysts for a wide and diverse range of organic transformations when immobilized on appropriate solid supports. This chapter describes the development of a highly active and highly selective heterogeneous catalyst based on Ni-Au NPs supported on activated carbon fibres (ACFs) for the partial reduction of *m*-dinitrobenzene (*m*-DNB) to *m*-nitroaniline (*m*-NAN), an important platform

chemical used in the synthesis of dyes and polymers. Initially, monodispersed Ni NPs (ranging from 2 to 14 nm) were prepared with poly-N-vinyl-2-pyrrolidone (PVP) as a stabilizer. Evaluation of the NPs as catalysts in the liquid-phase hydrogenation of *m*-dinitrobenzene led to the establishment of an antipathetic structure sensitivity, *i.e.* the larger NPs displayed a 6-fold higher turnover frequency than the smaller NPs. The selectivity to the target *m*-NAN product is independent of the size of the Ni NPs, possibly due to preferential PVP absorption of the NP edges and vertices. Consequently, monodispersed Ni NPs (2 nm) were supported on ACFs and residual PVP was removed by UVO, rendering a highly selective structured catalyst that affords *m*-NAN in almost 96% yield. A two-site (plane vs. edge Ni-atoms) Langmuir-Hinshelwood kinetic model is consistent with the experimental kinetic data confirming low-coordination atoms (edges and vertices) are responsible for selective reaction. Consequently, we prepared bimetallic Ni-Au NPs (Ni:Au = 1:1) to generate Ni surface sites mimicking the properties of edge and vertex atoms. The resulting UVO-treated Ni-Au NPs (3 nm) immobilized on ACFs afford *m*-NAN with a yield exceeding 98%. Such a high yield appears to be unprecedented and shows how careful nanocatalyst design, guided by detailed structural characterization and mechanistic study, can lead to highly selective catalysts of industrial relevance.

5.1 Introduction

It has been demonstrated in **Chapter 4** that ACFs are suitable as support of catalysts used in the production of functionalized nitroarenes. Unlike iron and cobalt, nickel was found to be very weakly active in the CTH of *p*-CNB to *p*-CAN which might indicate that the use of nickel as an active catalyst in hydrogenations requires it to be in its metallic form, in presence of gaseous hydrogen. Ni NPs have displayed remarkable efficiency in a number of catalytic hydrogenation of nitroaromatic compounds, *e.g.* nitrobenzene,^{131,132} *p*-nitrophenol,¹³³ nitrotoluene, nitronaphthalene and dinitroaniline,¹³⁴ but the influence of the NPs size on these reactions has not been explored.

Reactions taking place on the NP surface can be influenced by the variation of surface structure and electronic properties of the NPs. If present, these effects are usually more pronounced in the low nanometre range.¹³⁵ Differences in reactivity may be connected to the relative amount of plane, edge and vertex surface atoms which vary with NP size¹³⁶ and the size-sensitivity of catalytic reactions has been rationalized on the basis of structural and electronic factors.^{137,138} The electronic and geometric properties of NPs may also be manipulated by the addition of a second metal, *i.e.* to generate bimetallic NPs¹³⁹⁻¹⁴² which often show higher selectivity and reactivity than their monometallic counterparts. Recently, there has been a tremendous growth in interest in the application of bimetallic NPs in catalysis and, in particular, the use of Fe, Ni or Co in combination with noble metals.^{143,144}

This chapter describes a systematic investigation on unsupported and ACF-supported Ni NPs for the partial hydrogenation of *m*-dinitrobenzene (*m*-DNB) to *m*-nitroaniline (*m*-NAN), where the over-hydrogenation to *m*-phenylenediamine (*m*-PDA) should be avoided. The rational development of a highly active bimetallic Ni-Au NP system immobilized on ACFs was subsequently performed.

5.2 Experimental

Material

The synthesis of the unsupported Ni, Au and Ni-Au NPs is described in **Section 3.1.1** while their ACF-supported analogues were prepared following the procedure detailed in **Section 3.1.2.2**. Since ACFs surface was systematically oxidized by nitric acid before impregnating the pre-formed NPs, no subscript referring to this treatment has been included to the catalyst names (unlike in **Chapter 4**) to reduce the notation. Instead, the type of treatment applied to remove the traces of PVP is specified. For instance, the 2 nm Ni NPs supported on ACF and cleaned from the PVP by pyrolysis is referred as “Ni₂/ACF_{ΔT}” (“Ni₂/ACF_{UVO}” if cleaned by UV-ozone).

Characterization of the catalysts

Metal content was determined by AAS. The morphology of nanoparticles was observed by HRTEM and HRSEM. XRD was used to characterize the composition of the nanoparticles. The experimental conditions and instruments specifications used during these characterizations are described in **Section 3.4**.

Three-phase catalytic hydrogenation

The hydrogenation of *m*-DNB over unsupported or supported NPs was performed following the detailed procedure in **Section 3.2.3** and **Section 3.2.4**, respectively. A summary of the experimental conditions is found in **Table 3.1**. The calculations of conversion, selectivity, yield, transformation rate and turnover frequencies were realized using the equations presented in **Section 3.3**.

5.3 Results and Discussion

5.3.1 Preparation and characterization of the Ni NPs

The size of NPs depends on the proportion of particle nucleation relative to particle growth during their formation,¹⁴⁵ which in practical terms is influenced by several synthesis parameters like a reducing agent strength, temperature, solvent, pH and type of stabilizer to prevent agglomeration. Typically, other things being equal, strong reducing agents (NaBH₄) favor the formation of smaller NPs as these reducing agents induce rapid nucleation, whereas weak reducing agents, *e.g.* polyols, result in the formation of larger NPs due to reduced nucleation and NP growth mechanisms dominating. Consequently, we prepared a series of Ni NPs of different sizes (see below) from NiSO₄·6H₂O employing PVP as a stabilizer with a series of different reducing agents. Details are given in the Experimental and reaction conditions are summarized in **Table 5.1**.

Table 5.1. Conditions used in the preparation of the Ni NPs.

NPs	<i>d</i> (nm)	NiSO ₄ ·6H ₂ O	Solvent	PVP (M _w , mass)	Main Reducing reducing agent
Ni2	2	0.053 g	Ethylene glycol, 100 cm ³	10'000, 0.22 g	Ethylene glycol
Ni4	4	0.26 g	Ethylene glycol, 50 cm ³	29'000, 2.2 g	NaBH ₄ , 0.1 g
Ni11	11	0.26 g	Ethylene glycol, 120 cm ³	29'000, 2.2 g	N ₂ H ₄ ·H ₂ O, 0.1 g
Ni14	14	0.26 g	Tetra-ethyleneglycol, 120 cm ³	29'000, 2.2 g	Tetra-ethyleneglycol

The Ni NPs were characterized by TEM and HRTEM (**Figure 5.1**), revealing spherical morphologies with cubo-octahedral shape.¹⁴⁶ From the associated size distribution graphs (**Figure 5.1B, D**) the average size of the Ni NPs was determined as 2 nm (prepared using ethylene glycol, termed Ni2), 4 nm (prepared using NaBH₄, termed Ni4). The NPs prepared

using hydrazine hydrate, termed Ni11, or using tetra-ethyleneglycol, termed Ni14, measured 11 and 14 nm, respectively (cf. **Appendix, Figure S5.1 and S5.2**). Moreover, the histograms show a narrow size distribution.

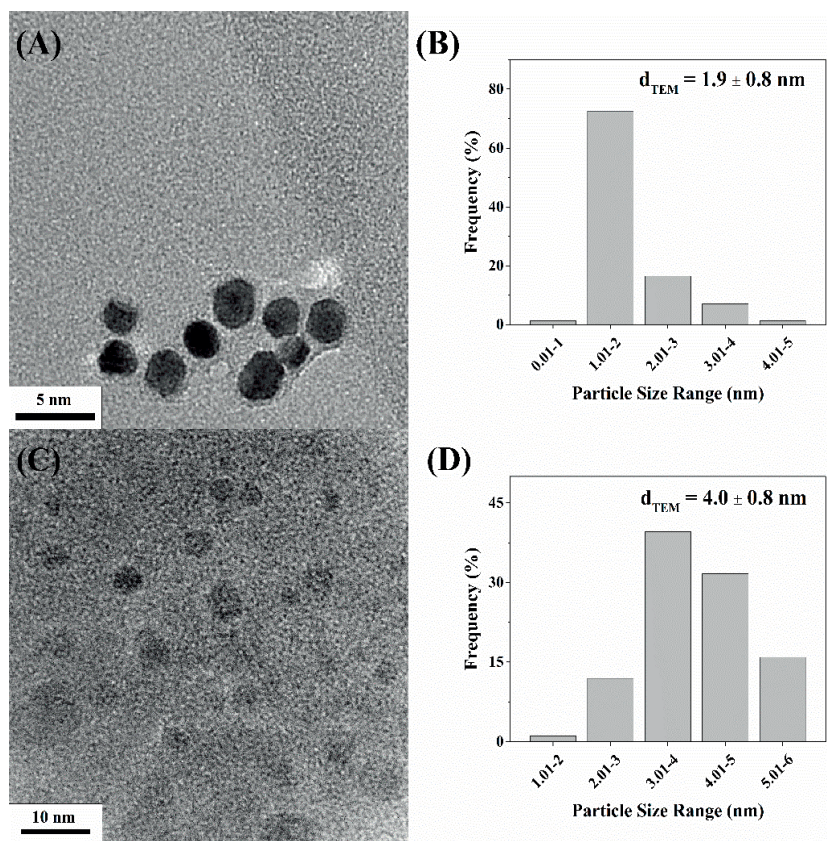


Figure 5.1. (A) Representative TEM image and (B) associated particle size distribution of the unsupported Ni2 NPs. (C) Representative HRTEM image and (D) associated particle size distribution of the unsupported Ni4 NPs.

5.3.2 Evaluation of the Ni NPs in the catalytic partial hydrogenation of *m*-DNB

Effect of the solvent

Along with the catalyst optimization, the effect of solvent was investigated using the Ni₄ NPs in a series of aliphatic alcohols (cf. **Figure 5.2**). The activity trend shows an optimum value at 0.66 mol_{*m*-DNB}·mol_{Ni}⁻¹·min⁻¹ using 1-PrOH, whereas the activities determined using MeOH and 2-hexanol are 2- and 3-fold lower, respectively. While these observations cannot be simply correlated with solvent properties, it is worth noting that the interpretation of solvent effects in catalytic hydrogenations is based on a combination of various parameters.¹⁴⁷ Berthero and co-workers¹⁴⁸ established solvent–catalyst interaction as the main factor influencing catalyst activity, where a strong interaction inhibits significantly the kinetics due to active site blockage. They reported higher hydrogenation rates in EtOH and 1-PrOH (compared to MeOH and toluene) due to substrate bond polarization/activation (through H-bond with the alcohol) and a subsequent low apparent activation energy. Similarly, Augustine *et. al.*¹⁴⁹ showed competition in the adsorption of MeOH and EtOH with H₂ on the catalytic active sites with 2-PrOH acting as a hydrogen donor. For the Pd-catalyzed acetophenone hydrogenation, Drelinkiewicz *et. al.*¹⁵⁰ pointed out that the catalyst activity was influenced more by the solvent polarity than H₂ solubility.

The dielectric constant (ϵ) is used as a quantitative characteristic of solvent polarity¹⁴⁷ and represents the ability of a solvent to separate and stabilize charge. The selectivity decreases as the dielectric constant of the solvent increases, MeOH ($\epsilon = 33$) to 2-hexanol ($\epsilon = 11$). This effect may be attributed to the higher solvation of the substrate and charge stabilization in polar solvents. Thus, high polarity solvents promote the activation/polarization of the nitro group and interaction with the catalyst.¹⁵¹

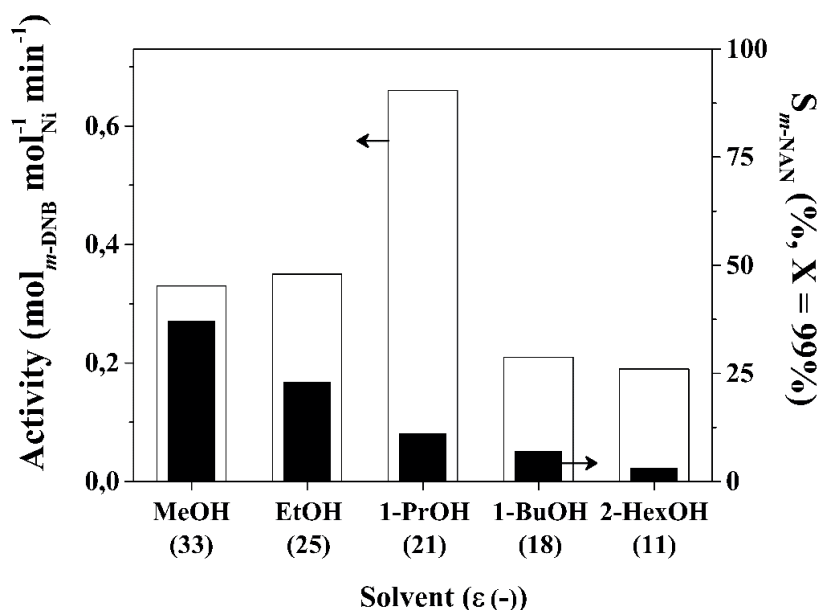


Figure 5.2. Variation of activity (open bars) and selectivity to *m*-NAN (solid bars) using the Ni₄ NPs for a range of alcoholic solvents with different dielectric constants. *Reaction conditions:* $C_{m\text{-DNB},0} = 3.7 \times 10^{-3} \text{ mol} \cdot \text{l}^{-1}$; 80 cm^3 of MeOH; $T = 423 \text{ K}$; $P_{\text{tot}} = 20 \text{ bar}$; $P_{\text{H}_2} = 6.1 \text{ bar}$; $m\text{-DNB}:\text{Ni} = 58$.

Structure sensitivity of the *m*-DNB partial hydrogenation

The Ni NPs (Ni₂, Ni₄, Ni₁₁ and Ni₁₄ nm) were evaluated as catalysts in the liquid-phase hydrogenation of *m*-DNB in MeOH (see **Figure 5.3**). Interestingly, the turnover frequency (TOF) of the Ni₁₄ NPs is 6-fold higher than that observed for the Ni₂ NPs, which is consistent with an antipathetic structure sensitivity.¹⁵² To the best of our knowledge, size effects of Ni NPs in liquid phase hydrogenation of *m*-DNB have not been reported.

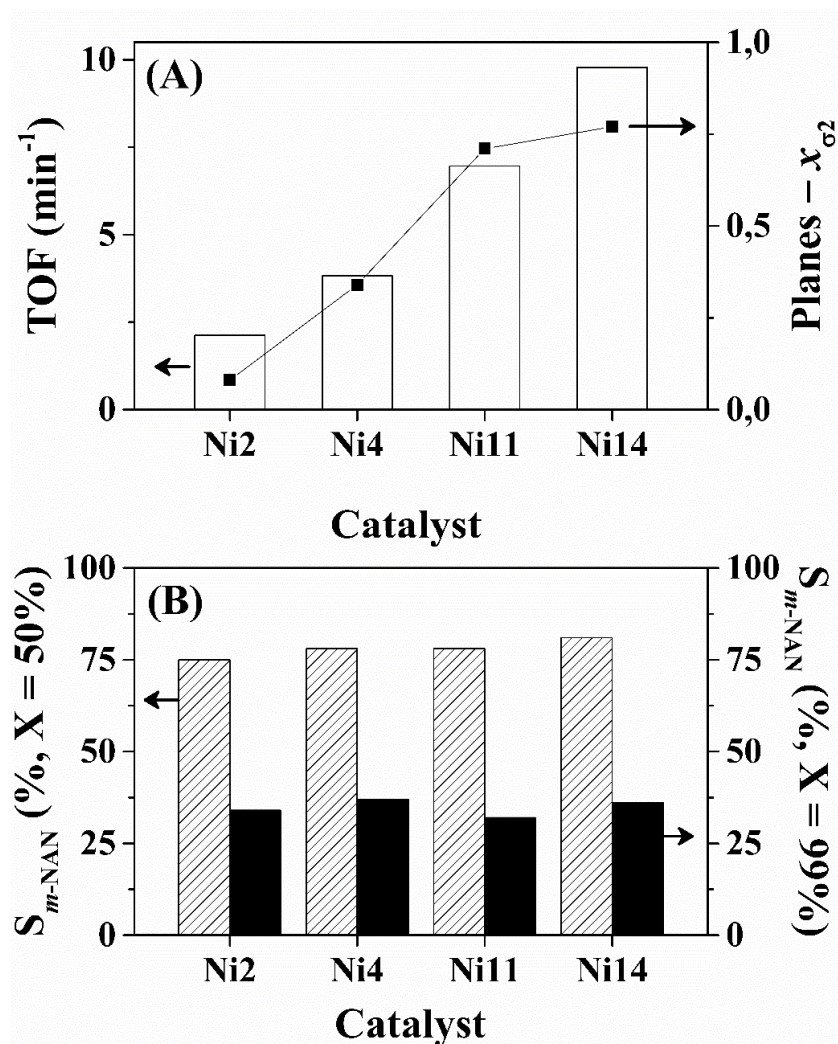


Figure 5.3. TOF (open bars) and fraction of planes x_{σ^2} (square symbols) and (B) Selectivity to m -NAN for unsupported Ni NPs at 50% (hatched bars) and 99% conversion (solid bars). Reaction conditions: $C_{m\text{-DNB},0} = 3.7 \times 10^{-3} \text{ mol} \cdot \text{l}^{-1}$; 80 cm^3 of MeOH; $T = 423 \text{ K}$; $P_{\text{tot}} = 20 \text{ bar}$; $P_{\text{H}_2} = 6.1 \text{ bar}$; $m\text{-DNB:Ni} = 58$.

NP size influences the TOF of a reaction due to electronic and geometric effects¹⁵³ and the relative ratio of the different types of surface atoms (edge, vertex and plane atoms), which changes substantially with particle size, *i.e.* larger NPs possess mainly large crystal planes with atoms of high coordination number, whereas in smaller NPs metal atoms with low coordination numbers are more prevalent. The non-ideal face-centered cubo-octahedron (fcc) model established by Hardeveld *et al.*¹⁵⁴ was used to determine the relative number of different atom types present on the surfaces of the different Ni NPs and the corresponding

surface atoms fractions (x_i) are reported in **Table 5.2**. Ni atoms with low coordination numbers, *i.e.* edge and vertex atoms, dominate in the Ni₂ NPs whereas planes dominate the Ni₁₄ NPs suggesting that plane Ni atoms are more active for the hydrogenation of *m*-DNB. The correlation between the TOF and planes fraction ($x_{\sigma 1}$) with the NPs size is shown in **Figure 5.3A**. This is probably linked to a stronger interaction of the –NO₂ group in the *m*-DNB substrate on the plane atoms.¹⁵⁵

Table 5.2. Estimated surface atom types for the Ni NPs.

NPs	Dispersion (%)	Fraction (-)	
		Planes – $x_{\sigma 1}$	Edges and vertices – $x_{\sigma 2}$
Ni ₂	47.6	0.08	0.53
Ni ₄	25.3	0.34	0.39
Ni ₁₁	9.7	0.71	0.17
Ni ₁₄	7.7	0.77	0.14

The selectivity to the partially hydrogenated *m*-NAN product was found to be essentially independent of the NP size, corresponding to 78±3% at a conversion of 50% and decreasing to 35±3% at a conversion of 99% (**Figure 5.3B**). This effect could be due to the influence of the PVP used as a stabilizing agent, despite removing excess PVP via extensive washing and re-dispersion of the NPs in EtOH (see Experimental for details).¹⁵⁶ PVP adsorbs preferentially on the edges and vertices of NPs (*i.e.* low coordination number sites compared to plane atoms). The existence of different strengths of adsorption between structure-directing agent and surface atoms with distinct miller indices have been demonstrated by density functional theory (DFT) calculations.^{157,158} Consequently, the low selectivity to the target product which is independent of the size of the Ni particle suggests that edge and vertex

atoms are probably responsible for the reaction selectivity, but in the disperse NPs they are blocked by PVP.

Preparation and characterization of Ni NPs supported on ACFs

Ni₂ and Ni₁₄ NPs were supported on ACFs and treated by UV-Ozone (UVO) or pyrolysis (ΔT) under an inert gas in order to remove residual PVP from the nickel surfaces (see Experimental for details). These catalysts are referred as Ni/ACF_{UVO} or Ni/ACF _{ΔT} , respectively. Representative HRSEM images of the Ni NPs after PVP removal by UVO treatment or pyrolysis are shown in **Figure 5.4A** and **B**. Only slight particle growth is observed following UVO treatment (Ni₂: 2.0 \rightarrow 2.3 nm; Ni₁₄: no change) whereas extensive Ni sintering occurs during the thermal treatment process (Ni₂: 2.0 \rightarrow 26 nm; Ni₁₄: 14.0 \rightarrow 30 nm).

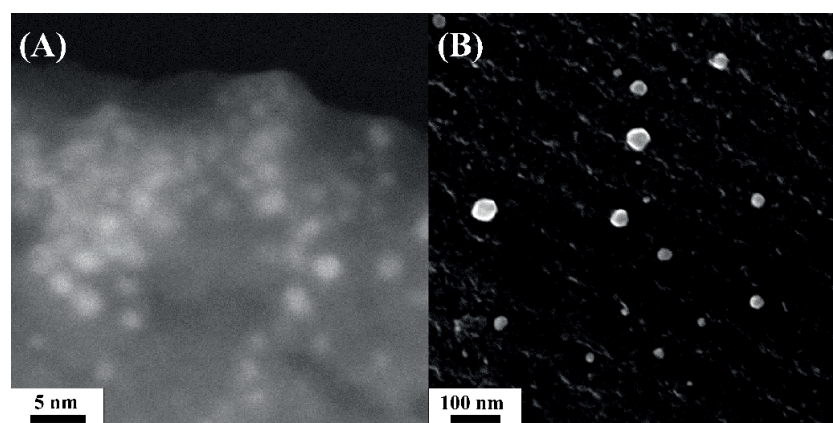


Figure 5.4. Representative HRSEM (Zeiss Merlin) images of supported (A) Ni₂/ACF_{UVO} and (B) Ni₂/ACF _{ΔT} catalysts.

PVP traces are believed to have a detrimental effect on the selectivity of the reaction due to their preferential adsorption on edges and vertices (see above). Using the PVP-free supported Ni/ACF catalysts a remarkable increase in selectivity to *m*-NAN (from 35% up to 96%) at 99% *m*-DNB conversion was observed (**Figure 5.5**). Moreover, the smaller (2 nm) supported NPs were found to provide the highest selectivity, confirming that the low

coordination Ni atoms (in the edges and vertices) are responsible for the high selectivity, since the smaller NPs have a high ratio of these atoms relative to planes, and that these sites appear to be fully accessible when the PVP is removed from the surface of the NPs.

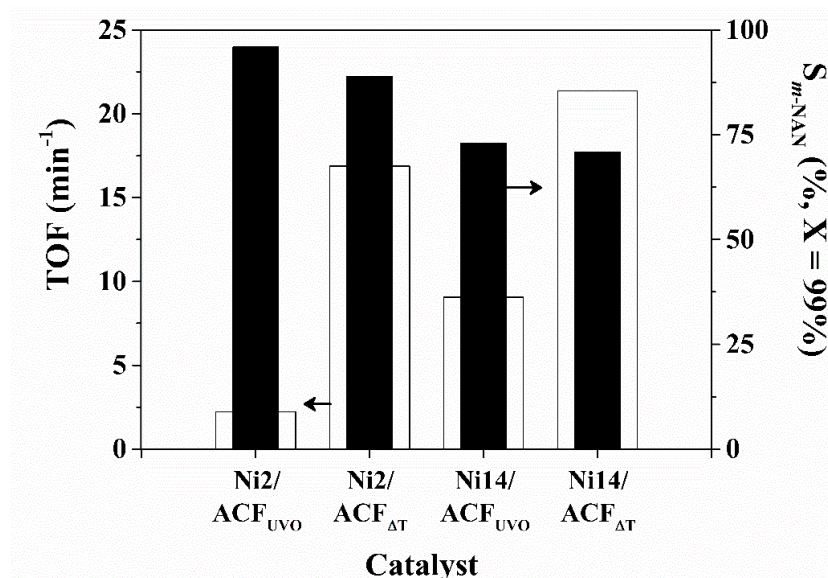


Figure 5.5. Variation of TOF (open bars) and selectivity to *m*-NAN (solid bars) over monodispersed (2 and 14 nm) Ni NPs/ACF treated by UV-Ozone or pyrolysis. Reaction conditions: $C_{m\text{-DNB},0} = 3.7 \cdot 10^{-3} \text{ mol} \cdot \text{l}^{-1}$, 80 cm^3 of MeOH, $P_{H_2} = 6.1 \text{ bar}$, $P_{tot} = 20 \text{ bar}$, $T = 423 \text{ K}$, *m*-DNB:Ni for the Ni2/ACF_{UVO}, Ni2/ACF_{ΔT}, Ni14/ACF_{UVO}, Ni14/ACF_{ΔT} = 31, 55, 32 and 62, respectively. Nickel loading (wt.%) = 1.79, 1.99, 2.56, 1.25, respectively (same order than for the *m*-DNB:Ni ratio).

The substrate and product distribution as a function of time for the Ni2/ACF_{UVO} catalyst is shown in **Figure 5.6A**. The *m*-DNB substrate is converted quasi-exclusively to *m*-NAN with a zero order kinetics (linear dependence of the concentration vs. time), up to 75% *m*-DNB conversion, with only a small amount ($\leq 5\%$) of the fully hydrogenated product, *m*-phenylenediamine (*m*-PDA). Comparison of the selectivity to *m*-NAN as a function of conversion for the unsupported PVP-stabilized Ni NPs vs. Ni/ACF_{UVO} catalysts (**Figure 5.6B, 4C**) reveals that the highest selectivity to *m*-NAN was recorded over the supported NPs. The Ni2/ACF_{UVO} catalyst is the most selective ($S_{m\text{-NAN}} \geq 95\%$ up to $X = 98\%$). In contrast, there is a continuous decrease in selectivity for unsupported Ni2 and Ni14 NPs as the conversion

increases. Consecutive/parallel reaction pathways are depicted in **Figure 5.7** presenting a simplified reaction scheme.

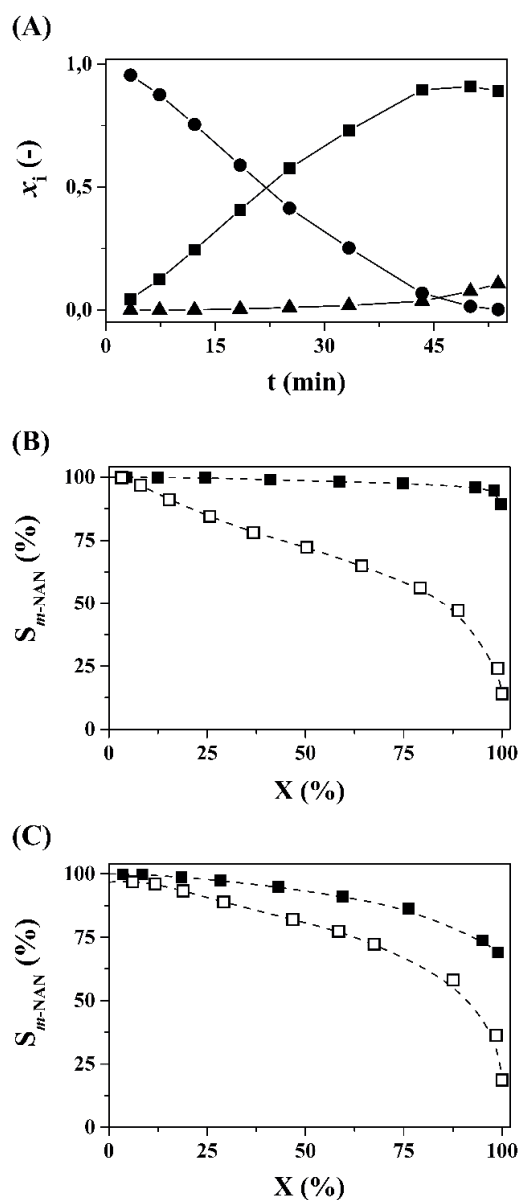


Figure 5.6. (A) Evolution of the molar fraction of (●) m -DNB, (■) m -NAN and (▲) m -PDA with time over cleaned supported 2 nm Ni NPs cleaned by UVO, Ni2/ACF_{UVO}; variation of selectivity with conversion for unsupported Ni (open symbols) and Ni/ACF_{UVO} catalysts (full symbols) for (B) Ni2 and (C) Ni14 NPs. Reaction conditions: $C_{m-DNB,0} = 3.7 \cdot 10^{-3} \text{ mol} \cdot \text{l}^{-1}$, 80 cm^3 of MeOH, $P_{H_2} = 6.1 \text{ bar}$, $P_{tot} = 20 \text{ bar}$, $T = 423 \text{ K}$, m -DNB:Ni = 58, 31, 58 and 32 for Ni2, Ni2/ACF_{UVO}, Ni14 and Ni14/ACF_{UVO}, respectively. Nickel loading (wt.%): (Ni2/ACF_{UVO}, Ni14/ACF_{UVO}) = 1.79, 2.56, respectively.

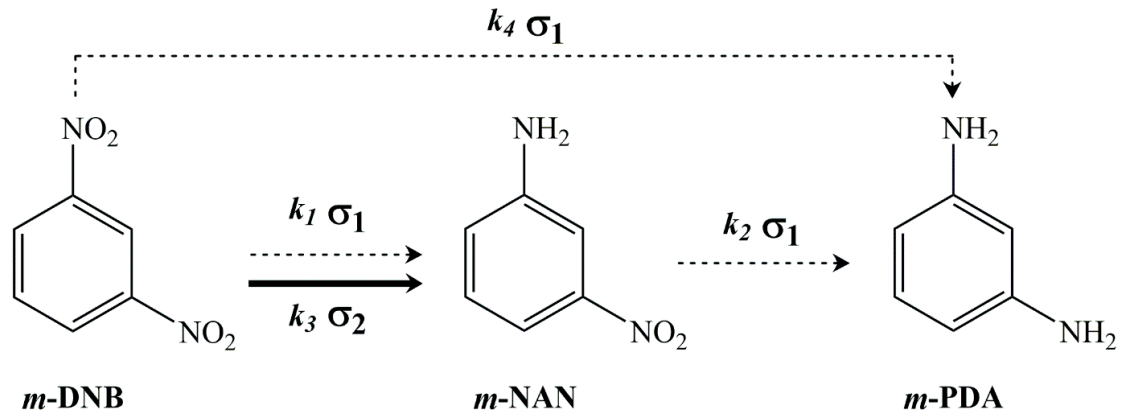
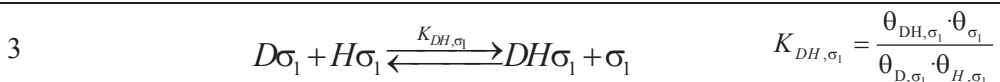
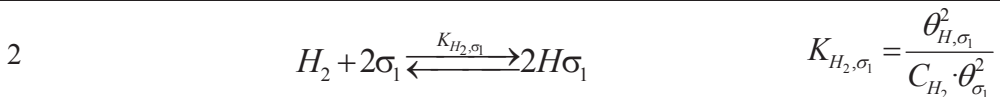
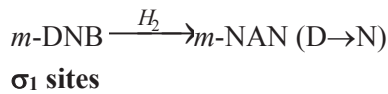


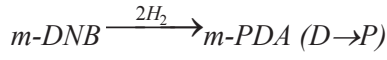
Figure 5.7. Reaction pathways associated with the hydrogenation of *m*-DNB to *m*-NAN and *m*-PDA. The targeted partial hydrogenation and undesired routes leading to hydrogenation of both nitro group are represented by bold and dashed arrows, respectively.

Kinetic modelling

The observed catalytic behaviour of the Ni2 and Ni14 and Ni2/ACFuvo and Ni14/ACFuvo systems was modelled by applying a Langmuir-Hinshelwood mechanism assuming two types of active sites, dissociative hydrogen adsorption and bimolecular reactions between the adsorbed species. The detailed derivation of the reaction rate expressions is based on the scheme presented in **Figure 5.7**. The rate equations were developed as follows with subscripts D, N and P referring to *m*-DNB, *m*-NAN and *m*-PDA, respectively, while DH, DH2, DH3 and NH correspond to the reaction intermediates:



4 (RDS*)	$DH\sigma_1 + H\sigma_1 \xrightarrow{k_{1,\sigma_1}} N\sigma_1 + \sigma_1$	$r_1 = k_{1,\sigma_1} \cdot \theta_{DH,\sigma_1} \cdot \theta_{H,\sigma_1}$
5	$N\sigma_1 \xrightleftharpoons{K_{N,\sigma_1}} N + \sigma_1$	$K_{N,\sigma_1} = \frac{\theta_{N,\sigma_1}}{C_N \cdot \theta_{\sigma_1}}$
<i>m</i> -DNB $\xrightarrow{H_2}$ <i>m</i> -NAN (D→N)		
σ_2 sites		
1	$D + \sigma_2 \xrightleftharpoons{K_{D,\sigma_2}} D\sigma_2$	$K_{D,\sigma_2} = \frac{\theta_{D,\sigma_2}}{C_D \cdot \theta_{\sigma_2}}$
2	$H_2 + 2\sigma_2 \xrightleftharpoons{K_{H_2,\sigma_2}} 2H\sigma_2$	$K_{H_2,\sigma_2} = \frac{\theta_{H,\sigma_2}^2}{C_{H_2} \cdot \theta_{\sigma_2}^2}$
3	$D\sigma_2 + H\sigma_2 \xrightleftharpoons{K_{DH,\sigma_2}} DH\sigma_2 + \sigma_2$	$K_{DH,\sigma_2} = \frac{\theta_{DH,\sigma_2} \cdot \theta_{\sigma_2}}{\theta_{D,\sigma_2} \cdot \theta_{H,\sigma_2}}$
4 (RDS*)	$DH\sigma_2 + H\sigma_2 \xrightarrow{k_{3,\sigma_2}} N\sigma_2 + \sigma_2$	$r_3 = k_{3,\sigma_2} \cdot \theta_{DH,\sigma_2} \cdot \theta_{H,\sigma_2}$
5	$N\sigma_2 \xrightleftharpoons{K_{N,\sigma_2}} N + \sigma_2$	$K_{N,\sigma_2} = \frac{\theta_{N,\sigma_2}}{C_N \cdot \theta_{\sigma_2}}$
<i>m</i> -NAN $\xrightarrow{H_2}$ <i>m</i> -PDA (N→P)		
σ_1 sites		
1	$N + \sigma_1 \xrightleftharpoons{K_{N,\sigma_1}} N\sigma_1$	$K_{N,\sigma_1} = \frac{\theta_{N,\sigma_1}}{C_N \cdot \theta_{\sigma_1}}$
2	$H_2 + 2\sigma_1 \xrightleftharpoons{K_{H_2,\sigma_1}} 2H\sigma_1$	$K_{H_2,\sigma_1} = \frac{\theta_{H,\sigma_1}^2}{C_{H_2} \cdot \theta_{\sigma_1}^2}$
3	$N\sigma_1 + H\sigma_1 \xrightleftharpoons{K_{NH,\sigma_1}} NH\sigma_1 + \sigma_1$	$K_{NH,\sigma_1} = \frac{\theta_{NH,\sigma_1} \cdot \theta_{\sigma_1}}{\theta_{N,\sigma_1} \cdot \theta_{H,\sigma_1}}$
4 (RDS*)	$NH\sigma_1 + H\sigma_1 \xrightarrow{k_{2,\sigma_1}} P\sigma_1 + \sigma_1$	$r_2 = k_{2,\sigma_1} \cdot \theta_{NH,\sigma_1} \cdot \theta_{H,\sigma_1}$
5	$P\sigma_1 \xrightleftharpoons{K_{P,\sigma_1}} P + \sigma_1$	$K_{P,\sigma_1} = \frac{\theta_{P,\sigma_1}}{C_P \cdot \theta_{\sigma_1}}$



σ_1 sites

1	$D + \sigma_1 \xrightleftharpoons{K_{D,\sigma_1}} D\sigma_1$	$K_{D,\sigma_1} = \frac{\theta_{D,\sigma_1}}{C_D \cdot \theta_{\sigma_1}}$
2	$H_2 + 2\sigma_1 \xrightleftharpoons{K_{H_2,\sigma_1}} 2H\sigma_1$	$K_{H_2,\sigma_1} = \frac{\theta_{H,\sigma_1}^2}{C_{H_2} \cdot \theta_{\sigma_1}^2}$
3	$D\sigma_1 + H\sigma_1 \xrightleftharpoons{K_{DH,\sigma_1}} DH\sigma_1 + \sigma_1$	$K_{DH,\sigma_1} = \frac{\theta_{DH,\sigma_1} \cdot \theta_{\sigma_1}}{\theta_{D,\sigma_1} \cdot \theta_{H,\sigma_1}}$
4	$DH\sigma_1 + H\sigma_1 \xrightleftharpoons{K_{DH2,\sigma_1}} DH2\sigma_1 + \sigma_1$	$K_{DH2,\sigma_1} = \frac{\theta_{DH2,\sigma_1} \cdot \theta_{\sigma_1}}{\theta_{DH,\sigma_1} \cdot \theta_{H,\sigma_1}}$
5	$DH2\sigma_1 + H\sigma_1 \xrightleftharpoons{K_{DH3,\sigma_1}} DH3\sigma_1 + \sigma_1$	$K_{DH3,\sigma_1} = \frac{\theta_{DH3,\sigma_1} \cdot \theta_{\sigma_1}}{\theta_{DH2,\sigma_1} \cdot \theta_{H,\sigma_1}}$
6 (RDS*)	$DH3\sigma_1 + H\sigma_1 \xrightarrow{k_{4,\sigma_1}} P\sigma_1 + \sigma_1$	$r_4 = k_{4,\sigma_1} \cdot \theta_{DH3,\sigma_1} \cdot \theta_{H,\sigma_1}$
7	$P\sigma_1 \xrightleftharpoons{K_{P,\sigma_1}} P + \sigma_1$	$K_{P,\sigma_1} = \frac{\theta_{P,\sigma_1}}{C_P \cdot \theta_{\sigma_1}}$

A surface balance of active sites gives coverage of vacancies for the two types of active sites. The coverage of the intermediate species was neglected:

$$1 = \theta_{\sigma_1} + \theta_{D,\sigma_1} + \theta_{N,\sigma_1} + \theta_{P,\sigma_1} + \theta_{H,\sigma_1} \quad (5.1)$$

$$1 = \theta_{\sigma_2} + \theta_{D,\sigma_2} + \theta_{N,\sigma_2} + \theta_{H,\sigma_2} \quad (5.2)$$

Coverages are expressed in terms of adsorption constants and bulk concentrations:

$$\theta_{\sigma_1} = \frac{1}{1 + K_{D,\sigma_1} C_D + K_{N,\sigma_1} C_N + K_{P,\sigma_1} C_P + \sqrt{K_{H_2,\sigma_1} C_{H_2}}} \quad (5.3)$$

$$\theta_{\sigma_2} = \frac{1}{1 + K_{D,\sigma_2} C_D + K_{N,\sigma_2} C_N + \sqrt{K_{H_2,\sigma_2} C_{H_2}}} \quad (5.4)$$

The reaction rate expressions were developed for the four paths of the reaction presented in

Figure 5.7:

$$r_1 = \frac{k_{1,\sigma_1} K_{DH,\sigma_1} K_{D,\sigma_1} C_D K_{H_2,\sigma_1} C_{H_2}}{\left(1 + K_{D,\sigma_1} C_D + K_{N,\sigma_1} C_N + K_{P,\sigma_1} C_P + \sqrt{K_{H_2,\sigma_1} C_{H_2}}\right)^2} \quad (5.5)$$

$$r_3 = \frac{k_{3,\sigma_2} K_{DH,\sigma_2} K_{D,\sigma_2} C_D K_{H_2,\sigma_2} C_{H_2}}{\left(1 + K_{D,\sigma_2} C_D + K_{N,\sigma_2} C_N + \sqrt{K_{H_2,\sigma_2} C_{H_2}}\right)^2} \quad (5.6)$$

$$r_2 = \frac{k_{2,\sigma_1} K_{NH,\sigma_1} K_{N,\sigma_1} C_N K_{H_2,\sigma_1} C_{H_2}}{\left(1 + K_{D,\sigma_1} C_D + K_{N,\sigma_1} C_N + K_{P,\sigma_1} C_P + \sqrt{K_{H_2,\sigma_1} C_{H_2}}\right)^2} \quad (5.7)$$

$$r_4 = \frac{k_{4,\sigma_1} K_{D,\sigma_1} K_{DH,\sigma_1} K_{DH2,\sigma_1} K_{DH3,\sigma_1} C_D K_{H_2,\sigma_1}^2 C_{H_2}^2}{\left(1 + K_{D,\sigma_1} C_D + K_{N,\sigma_1} C_N + K_{P,\sigma_1} C_P + \sqrt{K_{H_2,\sigma_1} C_{H_2}}\right)^2} \quad (5.8)$$

The rate equations can be simplified by considering the concentration of H₂ constant (large excess), by neglecting the coverage of H₂ and *m*-PDA and by grouping the constants of intermediate compounds in the numerator:

$$r_1 = \frac{k'_{1,\sigma_1} K_{D,\sigma_1} C_D}{\left(1 + K_{D,\sigma_1} C_D + K_{N,\sigma_1} C_N\right)^2} \quad (5.9)$$

$$r_3 = \frac{k'_{3,\sigma_2} K_{D,\sigma_2} C_D}{\left(1 + K_{D,\sigma_2} C_D + K_{N,\sigma_2} C_N\right)^2} \quad (5.10)$$

$$r_2 = \frac{k'_{2,\sigma_1} K_{N,\sigma_1} C_N}{\left(1 + K_{D,\sigma_1} C_D + K_{N,\sigma_1} C_N\right)^2} \quad (5.11)$$

$$r_4 = \frac{k'_{4,\sigma_1} K_{D,\sigma_1} C_D}{\left(1 + K_{D,\sigma_1} C_D + K_{N,\sigma_1} C_N\right)^2} \quad (5.12)$$

The mass balance for *m*-DNB, *m*-NAN and *m*-PDA are given by:

$$\frac{dC_D}{dt} = -r_1 - r_3 - r_4 \quad (5.13)$$

$$\frac{dC_N}{dt} = r_1 + r_3 - r_2 \quad (5.14)$$

$$\frac{dC_P}{dt} = r_2 + r_4 \quad (5.15)$$

The parallel *m*-DNB → *m*-PDA path was taken into consideration for the Ni14 NPs, as a small amount of over-hydrogenation is observed at low conversions (< 5%). Therefore, Equation (5.8) and the contribution of r_4 in the mass balance were considered for the larger NPs. Equations (5.9), (5.10), (5.11) and (5.12) were solved (using Berkeley Madonna software v.8.3.18 with Runge-Kutta's method for differential equations). A good correlation between the model and experimental values was obtained for the four systems (see **Figure 5.8**). It is worth noting that all catalysts required a short ($\leq 10\%$ of the total reaction time) induction period, presumably due to activation of the catalyst in the reaction mixtures¹⁵⁹ or to surface restructuring processes.¹⁶⁰ The former is considered more likely in the presence of H₂ which re-reduces any passivated surface layer.¹⁶¹ The induction periods were not included in the kinetic curves simulations.

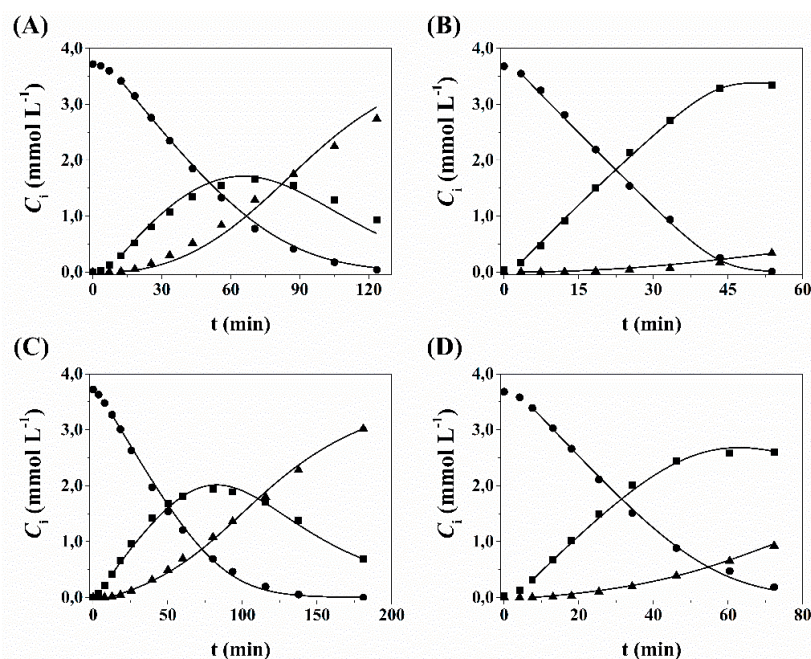


Figure 5.8. Experimental (●) *m*-DNB, (■) *m*-NAN and (▲) *m*-PDA and modelled (lines) concentration vs. time for (A) Ni2, (B) Ni2/ACF_{UVO}, (C), Ni14 (D) Ni14/ACF_{UVO}. Reaction conditions: $C_{m\text{-DNB},0} = 3.7 \cdot 10^{-3} \text{ mol} \cdot \text{l}^{-1}$, 80 cm^3 of MeOH, $P_{H_2} = 6.1 \text{ bar}$, $P_{tot} = 20 \text{ bar}$, $T = 423 \text{ K}$, *m*-DNB:Ni = 58, 31, 58 and 32 for Ni2, Ni2/ACF_{UVO}, Ni14 and Ni14/ACF_{UVO}, respectively. Ni loading (wt.%): (Ni2/ACF_{UVO}, Ni14/ACF_{UVO}) = 1.79, 2.56, respectively.

The adsorption and kinetic constants obtained are listed in **Table 5.3**. Similar values were fixed for the individual adsorption constants, which are slightly higher (< 2-fold) for the Ni2/ACF_{UVO} catalyst compared to the solvent dispersed Ni2 catalyst. The interaction of the *m*-DNB substrate is stronger (by about two orders of magnitude) with plane atoms (σ_1 sites) compared to the adsorption on edge and vertex atoms (σ_2 sites). The origin for this difference could come from the mode of adsorption with vertical (involving only one NO₂-group) on the edges and parallel to the crystallographic face on the plane atoms. By the same logic, the partially reduced *m*-NAN exhibit 10-fold higher adsorption constant (K_{N,σ_1}) in comparison with *m*-DNB (K_{D,σ_2}). For the Ni/ACF_{UVO} catalysts the kinetic constant, k_3 , related to the *m*-DNB to *m*-NAN hydrogenation steps on σ_2 sites is significantly higher (5- to 10-fold) than k_3 for the dispersed Ni NPs. Thus, with the dispersed Ni NPs the first hydrogenation step takes

place predominantly on σ_1 sites since the σ_2 sites are largely blocked by PVP. High k_3/k_1 and k_3/k_2 ratios demonstrates the key role of σ_2 sites in the first hydrogenation step with minimized over-hydrogenation, and accounts for the high selectivity of the Ni2/ACF_{UVO} catalyst.

Table 5.3. The adsorption and kinetic constants obtained from kinetic modelling.

Catalyst	Adsorption constants			Kinetic constants			
	K_{D,σ_1}	K_{D,σ_2}	K_{N,σ_1}	k_1	k_2	k_3	k_4
	(l mol ⁻¹)			(mmol _{<i>m</i>-DNB mol_{Ni}⁻¹ min⁻¹)}			
Ni2	330 ± 30	4.0	43 ± 1	0.21	0.86	0.04	-
Ni14				0.15	0.40	0.05	0.03
Ni2/ACF _{UVO}	550 ± 50	5.9 ± 1	73 ± 3	0.37	0.12	0.75	-
Ni14/ACF _{UVO}				0.26	0.20	0.28	0.02

Development of a bimetallic Ni-Au/ACF catalyst with separated Ni sites

The catalytic performance of the Ni NPs (see above) implies the key role of low coordination number Ni atoms to achieve high selectivity to *m*-NAN. Consequently, an active phase consisting of single Ni atoms could be highly effective and, therefore, Ni-Au NPs were prepared together with Au NPs for comparison purposes. The Au NPs were prepared in the same way as that described for the Ni NPs, *i.e.* from NaAuCl₄ in the presence of PVP using ethylene glycol as the reductant. The corresponding HRTEM images (**Figure 5.9A, C**) reveal spherical Au NPs, albeit with some degree of agglomeration, with a mean diameter of 6.9 ± 1.5 nm (Au7).

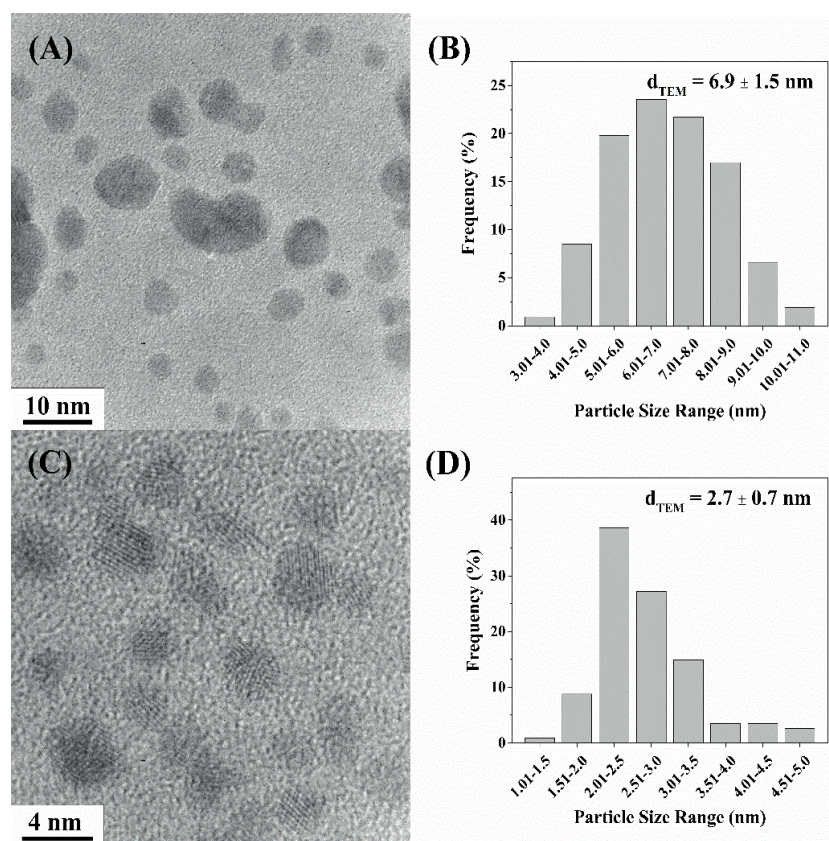


Figure 5.9. Representative HRTEM images of (A) Au₇ and (C) Ni-Au PVP-stabilized NPs and associated metal particle size distributions (B and D).

The Ni-Au NPs were synthesized by reduction of NiSO₄ and NaAuCl₄ (1:1) with NaBH₄ employing PVP as a stabilizer and the HRTEM images and associated size distribution graph of the bimetallic NPs are shown in **Figure 5.9**. The Ni-Au NPs have an average size of 2.7 ± 0.7 nm and the EDX spectrum (**Figure 5.10**) confirms the presence of gold and nickel in a single NP. The bulk binary Ni-Au phase diagram¹⁶² has a large miscibility gap excluding Ni-Au alloy formation at low temperatures. However, it has been shown by STM¹³⁹, low energy ion scattering and low energy electron diffraction¹⁶³ and Monte Carlo simulations in combination with *in situ* X-ray absorption fine structure studies¹⁶⁴ that a surface alloy between Au and Ni can exist in small NPs.

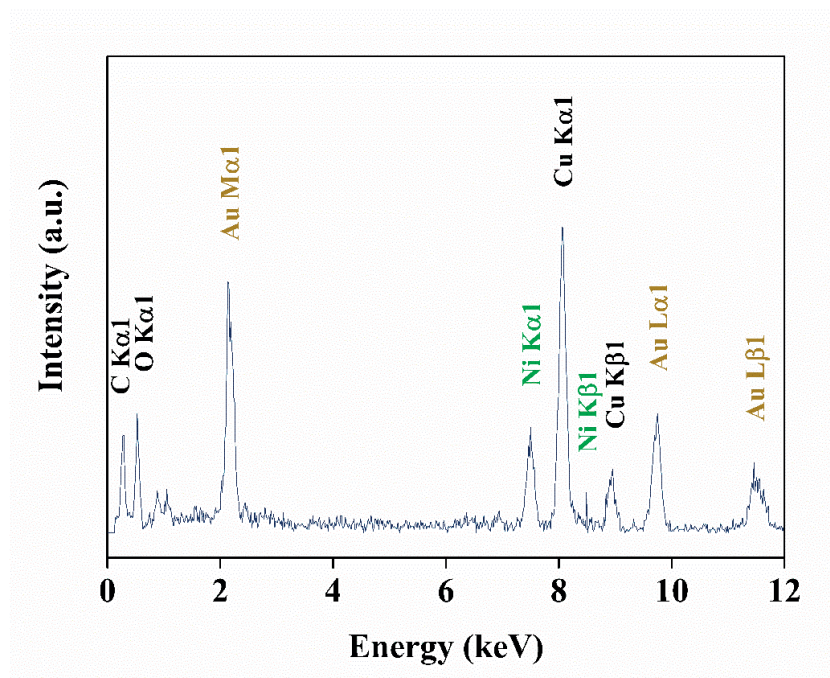


Figure 5.10. EDX spectrum of the Ni-Au NPs using a narrow beam with a 7 nm diameter.

Figure 5.11 shows the XRD diffractograms in the range 30–50° for monometallic Ni and Au NPs in comparison with the bimetallic Ni-Au NPs. The two main peaks for the Ni-Au NPs are observed at 38.3° (111) and 44.1° (200) indicating that the fcc crystallographic structure corresponds to the one of the monometallic gold (Au₇) with a cell parameter of 4.09 ± 0.02 Å. The Ni-Au NPs prepared in this work differ from those previously reported which exhibit peaks as a combination of the metallic components (Ni and Au) and shrinkage of the lattice structure.^{165,166} It indicates the absence of bulk alloy in the prepared bimetallic NPs. The larger peak width for the Ni-Au NPs sample could be due to the higher dispersion (2.7 nm), which is in line with the HRTEM images.

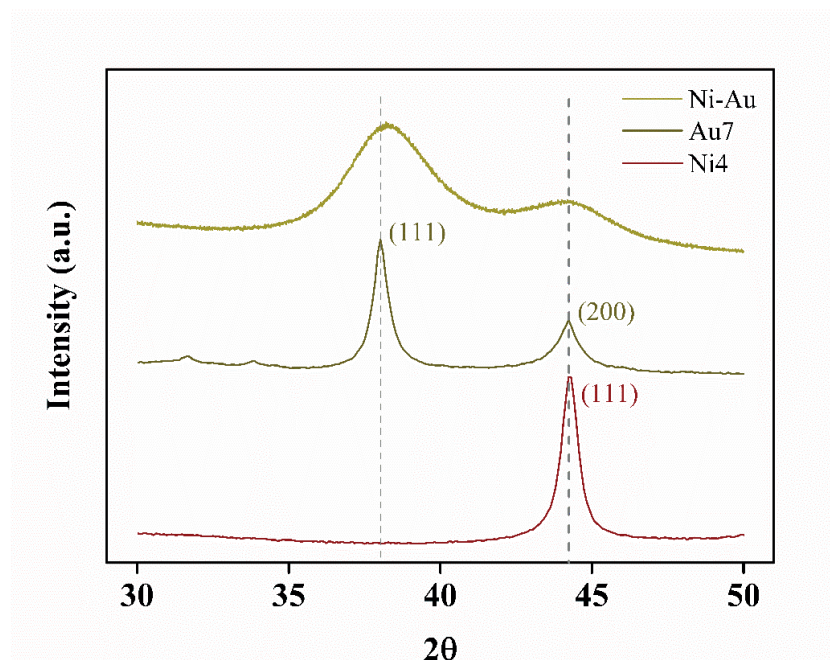


Figure 5.11. XRD profiles of Ni₄, Au₇ and Ni-Au colloids.

The Ni-Au NPs were evaluated as a catalyst in the liquid-phase hydrogenation of *m*-DNB in comparison to the Ni₂ and Au₇ NPs (**Figure 5.12**). Notably, the catalytic activity of all the NPs is of the same order of magnitude, whereas they exhibit considerable differences in selectivity. At close to full conversion ($X_{m\text{-DNB}} = 99\%$), the Au NPs affords mostly the fully hydrogenated product, *m*-PDA (selectivity towards *m*-NAN < 5%). The Ni NPs are somewhat more selective with about 35% *m*-NAN obtained. Gold is more electronegative than Ni, indicating that a more electron rich surface is detrimental to the selectivity of the reaction towards the *m*-NAN product. In contrast, the Ni-Au NPs afforded almost exclusively the desired *m*-NAN product ($S_{m\text{-NAN}} = 99\%$). Such a high selectivity may be attributed to the high dispersity of Ni atoms in the bimetallic Ni-Au NPs and, due to the presence of the electronegative Au atoms, the increased electropositive character of the separated Ni atoms.

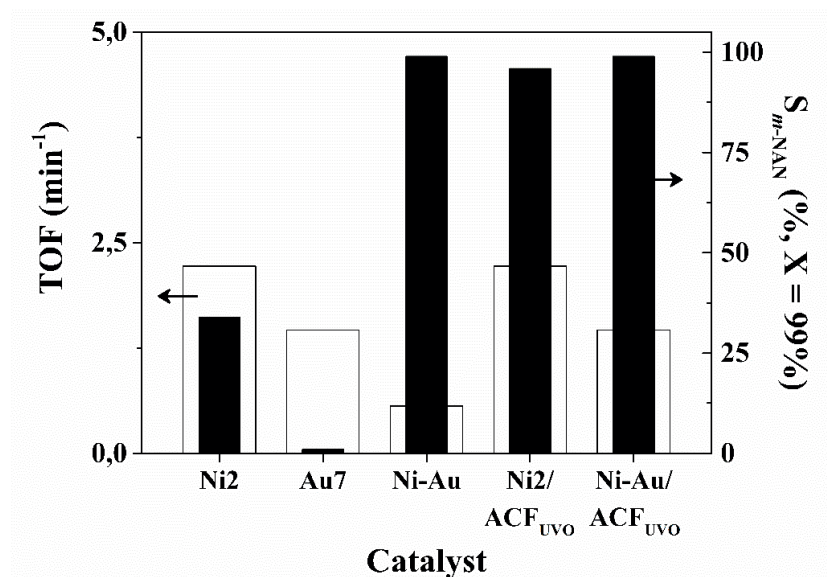


Figure 5.12. Variation of turnover frequency (TOF) (open bars) and selectivity to *m*-NAN (solid bars) using dispersed Ni₂, Au₇ and Ni-Au NPs and supported Ni₂/ACF_{UVO} and Ni-Au/ACF_{UVO} catalysts. *Reaction conditions:* $C_{m\text{-DNB},0} = 3.7 \times 10^{-3} \text{ mol} \cdot \text{l}^{-1}$; 80 cm³ of MeOH; T = 423 K; $P_{\text{tot}} = 20 \text{ bar}$; $P_{\text{H}_2} = 6.1 \text{ bar}$; *m*-DNB:Ni = 58. Ni loading (wt.%): (Ni₂/ACF_{UVO}, Ni-Au/ACF_{UVO}) = 1.79, 2.56, respectively.

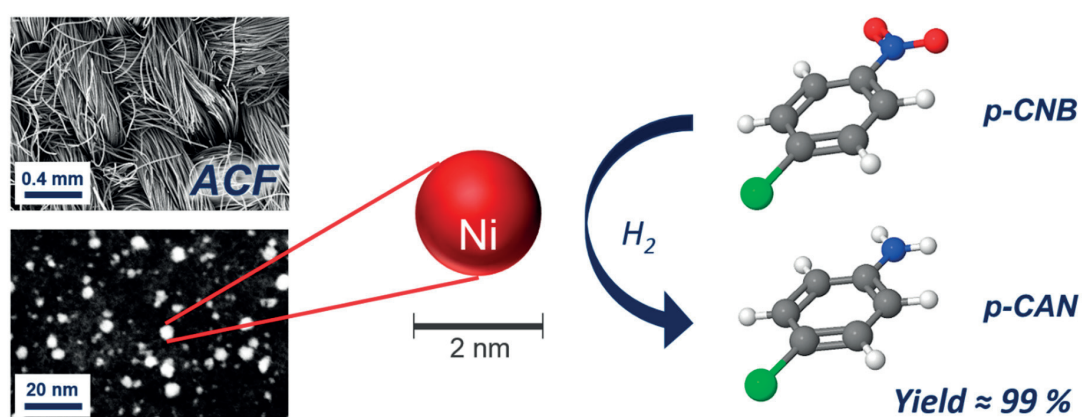
ACFs supported Ni-Au NPs were prepared in the same way described for the Ni₂/ACF_{UVO} system (see Experimental). The initial reaction rate was 3-fold higher for the Ni-Au/ACF_{UVO} catalyst compared to the unsupported bimetallic NPs and, importantly, the selectivity towards the desired product ($S_{m\text{-NAN}} = 99\%$) was preserved allowing *m*-NAN to be obtained in > 98% yield. In comparison, the yield of *m*-NAN obtained over the best monometallic supported Ni (Ni₂/ACF_{UVO}) catalyst was slightly lower (96%). To the best of our knowledge, a yield of *m*-NAN exceeding 98% is unprecedented for a Ni-based catalysts, although a yield of 94% was previously achieved using Ni-Ag core-shell NPs but hydrazine was used instead of hydrogen as a reducing agent.¹¹⁶ Elsewhere, the full hydrogenation rendering *m*-PDA product has been systematically reported from the H₂-assisted hydrogenation of *m*-DNB.¹⁶⁷

5.4 Conclusions

Monodispersed Ni NPs with mean diameters between 2–14 nm were prepared using PVP as a stabilizing agent and evaluated as catalysts in the partial hydrogenation of *m*-DNB to *m*-NAN. The catalytic activity of the NPs increased with the NP size, however, the selectivity of the reaction was low and over-hydrogenation to *m*-PDA was observed, especially at high conversions of *m*-DNB. Edge and vertex Ni atoms were shown to afford the desired *m*-NAN product whereas plane atoms preferentially lead to fully hydrogenated *m*-PDA. The low selectivity of the Ni NPs was attributed to preferential adsorption of the PVP stabilizer on the edge and vertex Ni atoms, consistent with a two-site Langmuir-Hinshelwood kinetic model developed to rationalize the obtained results. Immobilization of the smallest Ni NPs on ACFs followed by removal of the PVP from the NP surfaces via UVO treatment afforded a Ni₂/ACF_{UVO} catalyst that was considerably more selective to the partial hydrogenation product at close to full substrate conversion, *i.e.* the yield of *m*-NAN approaches 96%.

Based on the proposed mechanism, *i.e.* that low Ni coordination sites lead to the high selectivity, bimetallic PVP-stabilized Ni-Au NPs (Ni:Au = 1:1) were prepared with separated Ni surface sites. Indeed, the selectivity of the dispersed Ni-Au towards *m*-NAN compared to the monometallic Ni and Au NPs was significantly higher. This synergy was additionally ascribed to the more electropositive character of the Ni atoms due to the electron-withdrawing effect of the electronegative Au atoms. Finally, immobilization of the Ni-Au NPs on ACFs followed by UVO treatment gives a supported heterogeneous catalyst that affords *m*-NAN in > 98% yield. Such a high selectivity appears to be unprecedented and shows how careful nanocatalyst design, guided by detailed structural characterization and mechanistic studies, can lead to highly selective catalysts of industrial relevance.

Ni-based Structured Catalysts for Selective 3-Phase Hydrogenation of Nitroaromatics



This chapter is based on the following publication:

Beswick, O., *et al.*, *Ni-based structured catalyst for selective 3-phase hydrogenation of nitroaromatics*. *Catalysis Today*, 2016. **273**: p. 244-251.

Abstract

This chapter addresses the development of Ni-based catalysts using activated carbon fibres (ACFs) as a structured support and their application for the three-phase hydrogenation of nitroarenes ($T = 353 \text{ K}$; $P_{\text{tot}} = 10 \text{ bar}$). It was shown that metallic Ni^0 nanoparticles (NPs) with a mean diameter of $\sim 2.0 \text{ nm}$ stabilized by the ACFs microporous network were responsible for the catalytic transformation. To obtain optimum catalytic activity, the Ni/ACF catalyst must be freshly prepared and activated *in situ* by H_2 at $T > 353 \text{ K}$. Pre-treatment of the ACFs by nitric acid boosted the activity of the Ni/ACF catalyst, which exhibits high performance in hydrogenation of nitrobenzene to aniline (yield, $Y \sim 100\%$). The catalyst was tested for the reuse attaining a quasi-steady-state after the sixth reaction thereafter remaining relatively stable over seven consecutive runs. Near-quantitative transformation ($Y > 99\%$) of *p*-chloronitrobenzene to *p*-chloroaniline was achieved under mild conditions over the Ni/ACF catalyst with a *ca.* 20-fold higher activity than conventional Raney Ni. Thus, new catalyst reported here represents a significant step forward towards a simple, heterogeneous catalytic selective hydrogenation of nitroarenes that employs H_2 as the hydrogen source.

6.1 Introduction

Chapter 2 has shown that catalysts based on nickel are commonly used in the industrial production of nitroarenes. The lower activity of Raney nickel, for instance, compared to Pt or Pd has been compensated so far by its very low price, which explains the viability of Ni-based catalysts in industrial processes. Raney nickel, in particular, was used for the catalytic synthesis of chloroanilines from chloronitrobenzenes where the major challenge lies in avoiding dechlorination. Effective strategies to prevent the C-Cl cleavage and improving the activity have consisted in either adding additives to existing system²⁶ or modifying the Raney nickel by carbon deposition.^{27,28} A step forward could be taken by developing catalysts with higher dispersion of active metal which would not depend on the use of additives.

Chapter 5 has shown that the smallest (2 nm) Ni NPs supported on ACFs exhibited a higher selectivity to *m*-nitroaniline. However, the complex procedure employed for the preparation reduces the attractiveness of these catalysts for an industrial use. At the same time, the simple incipient wetness impregnation of ACFs afforded 2 nm metal Fe, Co or Ni oxide NPs (**Chapter 4**). An adjustment of the preparation protocol and experimental procedure is required to enable the creation of metallic Ni NPs and use their catalytic potential.

This chapter reports the facile preparation of ACF-based structured catalysts with supported Ni-NPs of high dispersion (1–2 nm) as an active phase. The influence of catalyst storage in ambient conditions on the Ni oxidation state has been assessed by TPR. The implementation of “in-situ” activation step under hydrogen prior to the catalytic run reduce the oxidized fraction of Ni NPs rendering highly selective and active catalysts in nitroarenes hydrogenation.

The activity/selectivity of optimized various Ni/ACF catalyst was compared to industrial Raney nickel (which serves as a benchmark catalyst), showing ~20-fold higher activity with ~99% *p*-CAN selectivity.

6.2 Experimental

Material

The preparation of the Ni/ACF catalysts is described in **Section 3.1.2.3**. For catalysts based on pre-treated ACFs, the treatment, its duration and the temperature at which it was performed, are specified as subscript in the catalyst name. For instance, “Ni/ACF_{HNO₃-373}” refers to a catalyst whose ACFs support was treated in nitric acid at 373 K.

Characterization of the catalysts

Metal content was determined by AAS. Specific surface area and pore volumes were measured by N₂ isotherm adsorption at 77 K (BET). TPR was used to study the oxidation state of nickel during the preparation of the catalysts and the behaviour of prepared catalysts towards ambient oxidation. The decomposition of metal precursors was studied by TPD. The morphology of nanoparticles was observed by STEM-HAADF. XRD, *in-situ* XRD and XPS were used to characterize the composition of the nanoparticles. The experimental conditions and instruments specifications used during these characterizations are described in **Section 3.4**.

Three-phase catalytic hydrogenation

The hydrogenation of *p*-CNB over Ni/ACF catalysts was performed as described in **Section 3.2.5**. The main experimental conditions are summarized in **Table 3.1**. The calculations of conversion, selectivity, yield, and transformation rate were realized using the equations presented in **Section 3.3**.

6.3 Results and Discussion

6.3.1 Catalyst Characterization

BET

BET analyses were performed with different ACFs samples and the associated SSAs and pore volumes are summarized in **Table 6.1**. A very high SSA ($> 2000 \text{ m}^2 \cdot \text{g}^{-1}$) was found for the as received, non-treated ACFs (entry 1). Nitric acid treatment at 373 K decreased both the SSA and the pore volume (entry 2). This effect has been already reported by Shim *et al.*¹⁶⁸ and is due to: *i*) the increased amount of functional O-groups on the surface and *ii*) a change in the carbon morphology. The surface atomic oxygen content on ACFs after the nitric treatment was reported to increase from $0.4 \text{ mmol} \cdot \text{g}^{-1}$ to $7.5 \text{ mmol} \cdot \text{g}^{-1}$.¹⁶⁹ By heating under an inert gas the HNO_3 pre-treated ACFs recovered the initial SSA and the total pore volume (entry 3). It is plausible that the O-containing groups rendered part of the porous structure inaccessible for nitrogen adsorption. The deposition of 5 wt.% Ni (entries 4 and 5) changed only slightly the SSA (by 5–8%) and the pore volume of the ACFs compared to the initial value, indicating that the deposition of the metal salt does not lead to pore blocking.¹⁷⁰

Table 6.1. BET analysis of ACFs support and Ni/ACF catalysts, treated by HNO_3 or not.

N°	Sample	Ni content (wt.%)	Comment	SSA ($\text{m}^2 \cdot \text{g}^{-1}$)	Specific pore volume ($\text{cm}^3 \cdot \text{g}^{-1}$)
1	ACFs	0	as received	2120	0.88
2	$\text{ACF}_{\text{HNO}_3-373}$	0	⁴ HNO_3 treated	1750	0.73
3	$\text{ACF}_{\text{HNO}_3-373-\Delta}$	0	⁴ HNO_3 + thermal treatment in Ar at 673 K	2000	0.84
4	Ni/ACF	4.8	Calcination 673 K - reduction 673 K - passivation at RT	1960	0.83
5	$\text{Ni}/\text{ACF}_{\text{HNO}_3-373}$	3.8	Calcination 673 K - reduction 673 K - passivation at RT	2000	0.79

⁴ treated with nitric acid: 15% HNO_3 , 373 K, 15 min

6.3.2 Temperature Programmed Decomposition (TPD) and reduction (TPR)

The ACFs freshly impregnated by the Ni precursor, after drying, was studied by TPD to determine the decomposition of the precursor. The NO signal at the reactor outlet was monitored and the results are presented in **Figure 6.1**. The NO peak at 432 K corresponds to the decomposition (323–473 K) of the surface nitrates leading to the formation of NO₂.¹⁷¹ The second NO peak at 521 K results exclusively from the decomposition of the HNO₃ vapour (473–573 K) into NO₂.¹⁷² At the end of the calcination step NiO NPs are formed. Therefore, during catalyst preparation, the pyrolysis step was at 673 K to ensure complete decomposition of the nitrates. The surface O-groups are decomposed giving CO and CO₂ during TPD runs.⁹³

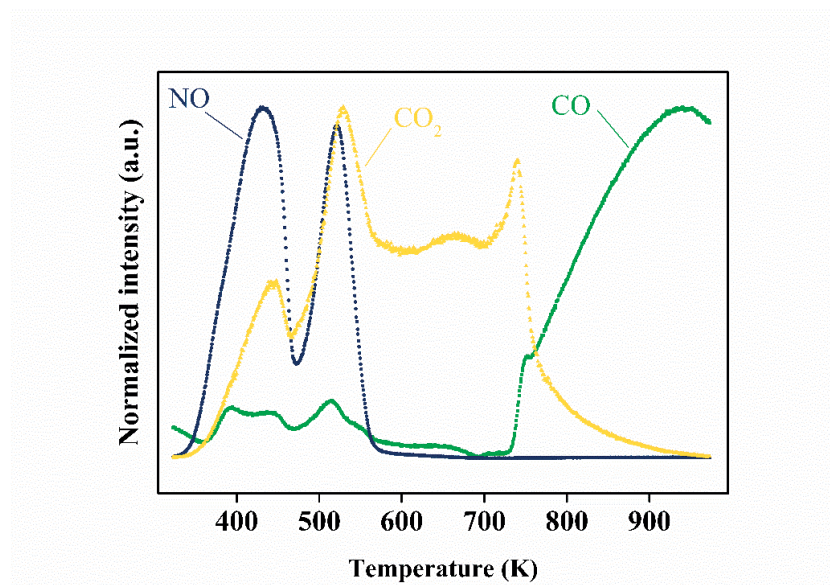


Figure 6.1. TPD profile of Ni(NO₃)₂/ACF_{HNO₃-373 (■ CO; ▲ CO₂; ◆ NO). Ramp = 6 K·min⁻¹; Flowrate = 50 cm³·min⁻¹ of He; masses monitored = 2, 16, 18, 28, 30, 44, 46 (2, 16, 18 and 46 are not shown on the chart).}

In order to choose a suitable reduction temperature, after the calcination step the catalyst was studied by TPR. The H₂-TPR profile of the NiO_x/ACF_{HNO₃-373} material exhibits two peaks at 602 and 778 K (**Figure 6.2A**). The first one (602 K) is attributed to the reduction of NiO_x NPs and the second one is due to methanation of ACFs. Performing the same procedure with

MS instead of TCD confirmed the peak attribution to CH₄, H₂ and H₂O signals (**Figure 6.2B**). Therefore, the reduction step during the catalyst preparation was set at 673 K for 1 hour to ensure formation of metallic Ni NPs while minimizing detrimental methanation of the ACFs support.

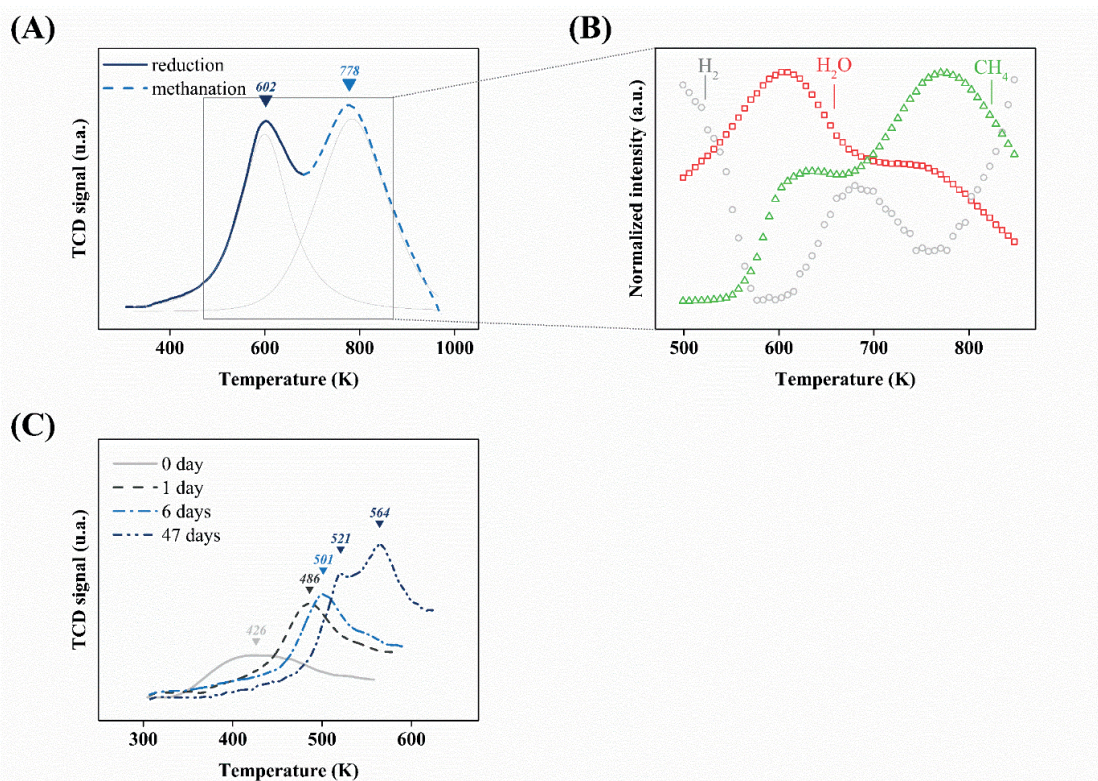


Figure 6.2. H₂-TPR profile of NiO_x/ACF_{HNO3-373} (after nitrates decomposition) using (A) a TCD detector and (B) a MS (Δ CH₄; \circ H₂; \square H₂O). Ramp = 2 K·min⁻¹; Flowrate = 20 cm³·min⁻¹ of 5% v/v H₂/Ar; masses monitored = 2, 16, and 18. H₂-TPR profile of (C) Ni/ACF_{HNO3-373} after reduction, passivation and exposition in air during different time.

Catalytic testing has demonstrated that *in-situ* activation under H₂ of freshly prepared catalysts was necessary to obtain significant catalytic activity. Since the catalyst was passivated after reduction, this activation seems to be responsible for the removal of thin oxide layer from the Ni NPs surface. To confirm this assumption and to get a better insight on the dynamics of oxidation of the Ni NPs, the passivated samples were exposed to air for different periods of time and analysed by H₂-TPR. Without exposure to air (0 day, **Figure**

6.2C) the hydrogen consumption was lower with the maximum at 426 K. Therefore, the Ni-oxides species are readily reducible during *in-situ* activation. The longer was the air exposure time, the higher the temperature and the larger the hydrogen consumption. The H₂-TPR profile of the sample exposed for to air 24 hours exhibited a peak maximum at 486 K and for the sample exposed for 6 days a peak maximum was at 501 K. After 47 days of air exposure the profile has two peaks at 521 and 564 K, suggesting that to activate the catalyst *in-situ* a temperature of 353 K is not enough. During the reduction of NiO to Ni, occurring at the interface of the two phases, the hydrogen and the water produced diffuse through the Ni formed.¹⁷³ The growth of the NiO thickness and volume of the nanoparticles increases the hydrogen diffusion distance during the TPR and could explain the observed shift in reduction peak with the exposure time to air of the Ni/ACF_{HNO3-373} catalyst.

In-situ XRD analysis

The nature of the Ni phase was studied *in-situ* by XRD analysis following each step of the precursor decomposition/reduction until no more changes were observed to the diffraction pattern. Pattern **A** shown in **Figure 6.3** represents the initial ACFs support and pattern **B** corresponds to the ACFs after deposition of the Ni(NO₃)₂·6H₂O precursor. A sample of impregnated ACFs was subjected to a thermal treatment (298 K to 723 K, 2 K·min⁻¹) under a 60 cm³·min⁻¹ flow of N₂ and left during one hour at the final temperature (**Figure 6.3C**). Finally, pattern **D** represents the impregnated sample subjected to a thermal treatment (298 K to 723 K, 2 K·min⁻¹) under a 60 cm³·min⁻¹ flow of 10% v/v H₂/N₂. Diffraction patterns **C** and **D** show additional components compared to patterns **A** and **B**, suggesting that both N₂ and H₂/N₂ treatments lead to the formation of a Ni⁽⁰⁾ phase by comparison with the JCPDS-ICDD reference standard, *i.e.* fcc Ni (04-0850).

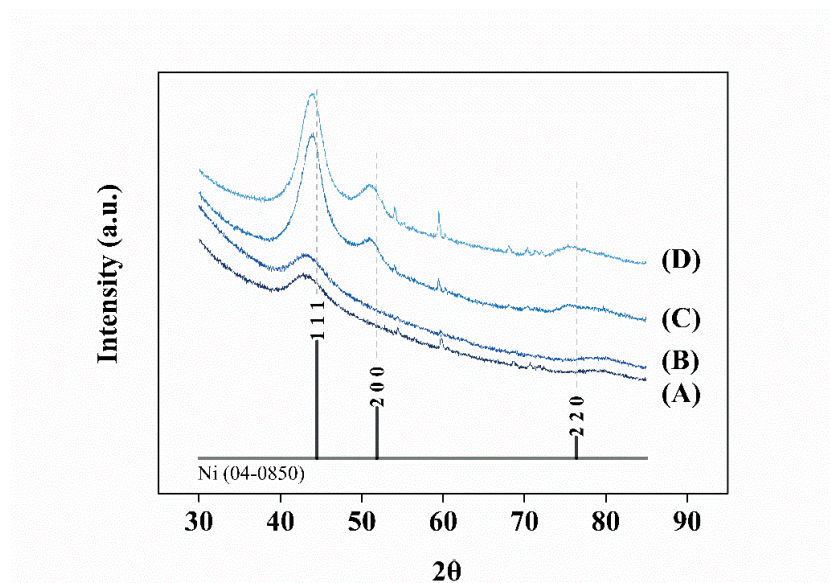


Figure 6.3. *In-situ* XRD profile of ACFs (A), Ni(NO₃)₂/ACF_{HNO₃-373} before (B) and after treatments in N₂ (C) and N₂/H₂ (D) at 723 K with JCPDS-ICDD reference diffractogram for Ni⁰ (standard card 04-0850).

The XRD analysis of the passivated Ni/ACF_{HNO₃-373} catalyst exposed to air over 6 days generated the pattern shown in **Figure 6.4**. The profile exhibits four main peaks over the 2θ range 20–90°, corresponding to the (222), (400), (440) and (440) planes of face-centred cubic NiO (JCPDS-ICDD 89-5881), and confirming the presence of nickel oxide after the standard treatment and air exposure.

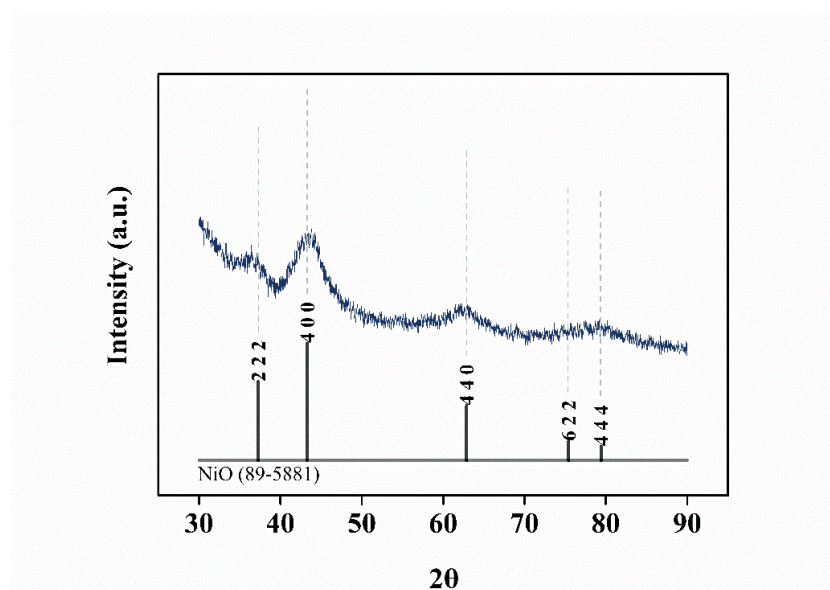


Figure 6.4. XRD pattern of Ni/ACF_{HNO₃-373} after 6 days of exposure in air with JCPDS-ICDD reference diffractogram for NiO (standard card 89-5881).

XPS analysis

Freshly prepared passivated Ni/ACF_{HNO₃-373} was studied by XPS before and after argon sputtering to gain information on the Ni NPs composition. Before sputtering the profile exhibits a symmetric Ni 2p_{3/2} peak at 855.7 eV and its satellite at 861.3 eV, respectively (**Figure 6.5A**). The contributions of the main peak of NiO produce two visible maxima (at 853.7 and 855.4 eV) whereas a single symmetric peak is detected corresponding to Ni(OH)₂.¹⁷⁴ The higher intensity of the Ni 2p_{1/2} peak measured at 873.7 eV compared to the satellite at 880.1, indicates that the NPs surface consists mainly of Ni(OH)₂. A contribution of NiO cannot be completely ruled out since the carbonaceous nature of catalyst results in low signal-to-signal.

After 5 min of Ar sputtering (2 nm) the position of the Ni 2p_{3/2} peak maxima was found to be shifted by 1.5 eV to 854.2 eV (**Figure 6.5B**). The shape presents an asymmetry visible on the left side of the peak that is characteristic of a NiO contribution. The position of the Ni 2p_{1/2} peak satellite at 878.1 eV, half-way from NiO (879 eV) and Ni⁰ (874 eV), could indicate some

contributions from Ni⁰.

In summary, XRD and XPS studies confirm that the conditions of Ni/ACF preparation lead to the formation of metallic Ni NPs during the reduction under hydrogen. These particles were covered by a thin Ni-oxide/hydroxide layer formed during the passivation step.

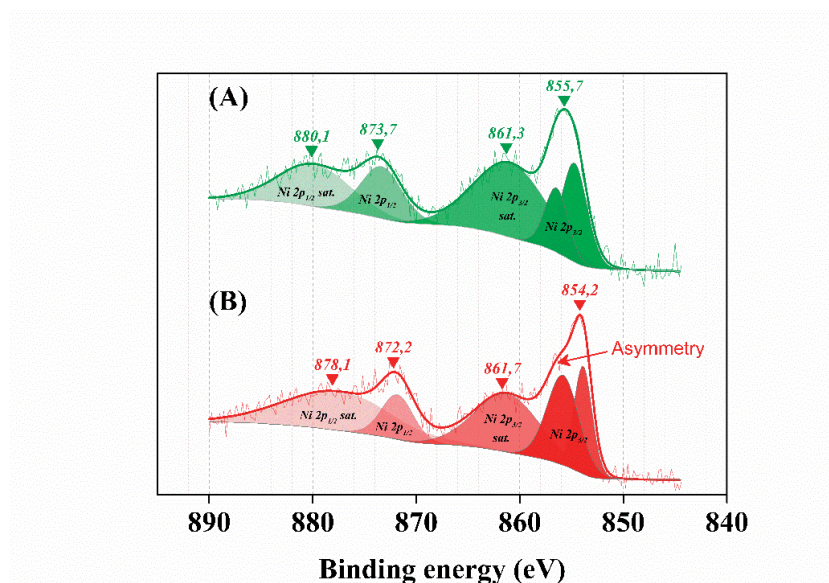


Figure 6.5. XPS profiles of freshly prepared Ni/ACF_{HNO₃-373} (A) before and (B) after 5 min of Ar sputtering.

STEM

HAADF STEM measurements were performed to observe the size and morphology of the Ni NPs. In the images they appear as bright contrast within the ACFs support composed of a lower density carbon material (Z-contrast).

Figure 6.6 shows the images of Ni/ACF and Ni/ACF_{HNO₃-373} (A, D) and outlines of the Ni NPs of these samples (B, E), respectively. The STEM derived histogram for the Ni/ACF catalyst (C) (with support non-treated by HNO₃) is characterized by a distribution of the NP size between 1.4–2.3 nm with 52% within the range. A mean particle diameter of 1.7 ± 0.8 nm was found. Analysis of Ni/ACF_{HNO₃-373} (F) (with non-treated by HNO₃ support)

reveals NPs in the range of 1.6–2.6 nm for 53% of the NPs with a mean particle size of 2.1 ± 1 nm.

Analysis of NiO_x/ACF and NiO_x/ACF_{HNO₃-373} (without H₂ during thermal treatment) revealed NPs with a mean particle size of 1.4 ± 0.5 nm and 1.3 ± 0.5 nm, respectively (images not shown).

Thus, the thermal treatment in the presence of hydrogen leads to only an increase in the mean NPs size. Note that the presence of particles with sizes below the detection threshold, not visible with the high magnification (1.3 Mx), cannot be excluded. Imaging with the aberration corrected microscope (FEI Titan Themis) of the Ni/ACF_{HNO₃-373} specimen suggested a larger proportion of NPs in the sub-nm range (0.5–1 nm) exist than detected with the FEI Talos F200S (cf. **Appendix, Figure S6.1**). Their enhanced catalytic properties could arise from their irregular shape and dangling chains of atoms on the surface, increasing the number active sites. Also, the distribution of the Ni/ACF_{HNO₃-373} specimen (**Figure 6.6C**) suggests that the NPs are attached rather than stacked. Therefore, the effective NPs surface available for catalysis might be greater for this sample, despite its larger mean diameter.

In summary, the oxidative pre-treatment of ACFs support by HNO₃ weakly affects the NiO_x NPs size. In contrast, the reductive treatment process at 673 K slightly diminishes the NP dispersion with a concomitant increase of average diameter of the NPs from 1.8 ± 0.7 to 2.1 ± 1.0 nm.

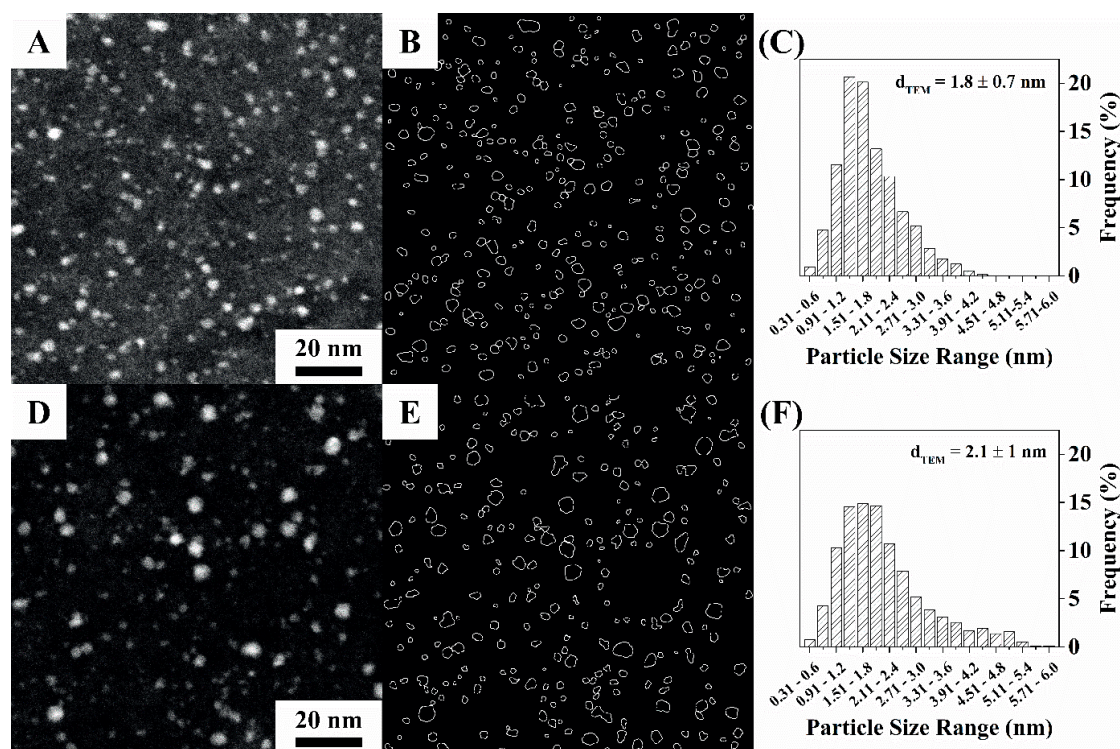


Figure 6.6. Representative STEM-HAADF images (**A, D**), outlines of the particles isolated after ImageJ processing (**B, E**) and related particles size distribution (**C, F**) for 5 wt.% Ni/ACF (above) and Ni/ACF_{HNO₃-373} (below) after reduction in H₂ followed by passivation, respectively.

6.3.3 Catalytic results

Effect of the ACFs acidic pre-treatment on catalytic performance

It is well-known that the concentration of oxygen-containing (O-) groups on an ACFs surface can be increased by acidic treatments.⁹³ In this study we applied a HNO₃ treatment at 298 K or 373 K to modify the ACFs (see experimental section for details). Nickel (5 wt.%) was deposited on pre-treated and non-treated ACFs and the obtained catalysts were tested in *p*-chloronitrobenzene (*p*-CNB) to *p*-chloroaniline (*p*-CAN) hydrogenation. **Figure 6.7** shows that the selectivity of all the catalysts was close to 100% while the activity drastically increases (3-fold) for the ACFs treated at 373 K. It is worth to noting that a yield of *p*-CAN close to 100% was obtained for all catalysts before dechlorination (cleavage C-Cl) starts.

Catalytic tests also demonstrated that *in-situ* activation under H₂ of freshly prepared/passivated catalysts was necessary to obtain catalytic activity.

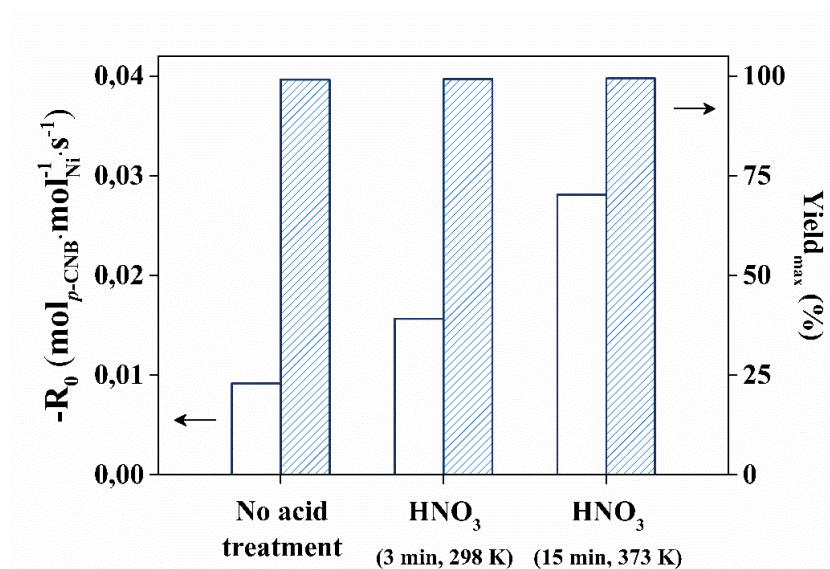


Figure 6.7. Effect of ACFs pre-treatment by HNO₃ on the selectivity to *p*-CAN (hatched bars) and activity (open bars) for the hydrogenation of *p*-CNB. Reaction conditions: $C_{p\text{-CNB},0} = 1.2 \times 10^{-1} \text{ mol} \cdot \text{L}^{-1}$, 100 cm³ of EtOH; T = 353 K; P_{tot} = 10 bar; P_{H₂} = 8.5 bar; molar *p*-CNB:Ni ratio = 50.

The effect of the ACFs oxidative treatment can be related to the Ni NPs size and to the concentration and the nature of functional O-groups on the carbon surface. The HNO₃-treated carbon was previously shown to display a high density of weak and strong acid sites.¹⁷⁵ During the calcination step in the catalyst preparation it is likely that the strong O-containing groups (rendering CO₂ during TPD runs) were removed whereas majority of weak groups (rendering CO in TPD) remain. In fact, during TPD performed over the catalysts after the calcination step, a 60% higher amount of CO was detected from Ni/ACF_{HNO₃-373} as compared to Ni/ACF (4.3 vs 2.7 mmol·g⁻¹). These weak O-groups were reported by Toebes *et al.*¹⁰⁵ to maintain the dispersion of Pt NPs on ACFs while the activity towards cinnamaldehyde hydrogenation was attributed to electronic effects. Also Ramaker *et al.* demonstrated that the lower electron density of the oxygen atoms of weak O-groups leads to the higher ionization

potential of the supported Pt NPs, increasing the TOF during hydrogenation of a tetralin ring.¹⁷⁶ Therefore, we suggest that the larger number of weak O-groups of Ni/ACF_{HNO3} as compared to Ni/ACF favour substrate adsorption on Ni NPs via the NO₂ group and thereby increasing the catalytic activity.¹⁷⁷

Reaction scope: Nitrobenzene hydrogenation

The Ni/ACF_{HNO3-373} catalyst is the most active and also has been tested in the hydrogenation of nitrobenzene (NB). **Figure 6.8A** illustrates the effect of the *in-situ* activation on the activity by showing the concentration of NB during catalytic runs performed with and without this step. The initial transformation was *ca.* 13 times higher when reducing *in-situ* the partially oxidized Ni NPs of the freshly prepared Ni/ACF_{HNO3-373} catalyst. We established that a temperature of 353 K during the *in-situ* activation was sufficient to obtain the optimal catalytic potential of a freshly prepared catalyst while a temperature > 393 K was required to reach the same activity with catalyst stored 16 days.

Representative concentration *vs* time profiles are shown in **Figure 6.8B**. Linear dependency of NB consumption was observed until close to 100% conversion. The aniline formation passes via azo- and azoxy-intermediates indicative of the condensation route established by Haber.¹⁶ It is important to note that the selectivity and yield of the desired aniline product continues to increase even after the full conversion of NB due to the completion of consecutive transformations of intermediates. Therefore, the maximum yield (and not the selectivity at close to full conversion) is the most important parameter to assess the catalytic performance.

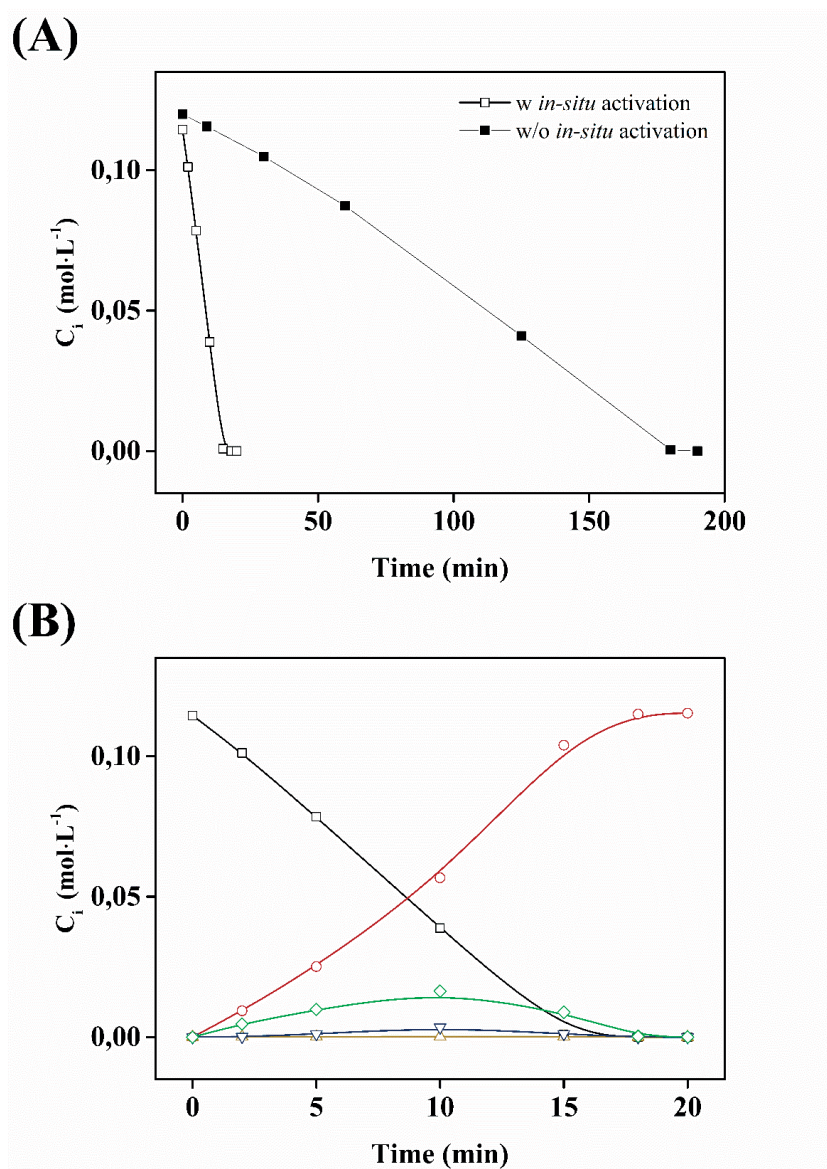


Figure 6.8. Nitrobenzene hydrogenation over Ni/ACF_{HNO3-373}. **(A)** comparison of NB concentration vs reaction time with and without *in-situ* activation and **(B)** Concentrations vs reaction time with *in-situ* activation (\square NB; \circ AN; \triangle azobenzene; ∇ azoxybenzene; \diamond nitrosobenzene). Reaction conditions: $C_{NB,0} = 1.2 \times 10^{-1}$ mol·l⁻¹; 100 cm³ of EtOH; T = 353 K; $P_{tot} = 10$ bar; $P_{H_2} = 8.5$ bar; molar ratio NB:Ni = 50.

The 5 wt.% Ni/ACF_{HNO3-373} catalyst was also evaluated in other challenging hydrogenations (Table 6.2). For the nitro-aromatics containing functional groups which are sensitive to the reduction conditions (e.g. alkenes, halogens, etc.), the maximum yields of the desired anilines are the main issue. These yields were compared to ones obtained using Raney

Ni under the same reaction conditions. The developed 5 wt.% Ni/ACF_{HNO3-373} catalyst outperformed, by *ca.* 20-fold, the Raney Ni catalyst in terms of activity in *p*-CNB hydrogenation and the maximum yield was also slightly higher (99.0 vs. 98.0%). It is worth to note that dechlorination after reaction completion (100% conversion of *p*-CNB) was much higher over Raney Ni resulting in rapid deactivation of the catalyst. At reaction completion (*X* = 100 %), selectivities towards aniline of 0.25% and 1.50% were obtained for the Ni/ACF_{HNO3-373} and the Raney nickel catalysts, respectively. The 5 wt.% Ni/ACF_{HNO3-373} catalyst was also highly efficient in *m*-dinitrobenzene hydrogenation affording a high yield of *m*-nitroaniline (99%).

Table 6.2. Activity and maximum yield of the amine for the hydrogenation of nitroaromatics (NC) over 5 wt.%Ni/ACF_{HNO3} and Raney Ni. *Reaction conditions:* $C_{NC,0} = 1.2 \times 10^{-1} \text{ mol} \cdot \text{l}^{-1}$; 100 cm³ of EtOH; T = 353 K; P_{tot} = 10 bar; P_{H2} = 8.5 bar; molar NC:Ni ratio = 50.

Nº	Catalyst	Substrate (NC)	Activity, $-R_0 \times 10^2$ (mol _{NC} · mol ⁻¹ _{Ni} · s ⁻¹)	Maximum Yield (%)	Time to reach X = 98% (min) ^A
1 ^B	Ni/ACF _{HNO3-373}	NB	0.24	100.0	171
2		NB	3.2	100.0	15
3		<i>m</i> -DNB ^C	0.15	97.0	409
4		<i>p</i> -CNB	2.8	99.0	23
5	Raney Ni	<i>p</i> -CNB	0.13	98.0	672

^A Without *in-situ* activation.

^B Normalized according to molar NC:Ni ratio towards the NB reduction (entry nº2).

^C Catalyst was tested at 423 K.

The developed Ni/ACF_{HNO3-373} catalyst has been compared to the state-of-the art Ni-based systems and the results are summarized in the **Table 6.3**. The high transformation rate exhibited by the Ni/ACF_{HNO3-373} catalyst under soft conditions (T = 353 K, P_{H2} = 8.5 bar)

(entry n°11), can be ascribed to the high dispersion of the nickel active phase. By far, this is the smallest Ni NPs reported for carbon supports. The lower specific reaction rate showed by the carbon-supported nickel catalysts with larger nanoparticles (entries n°2–7) supports this hypothesis.

Table 6.3. Comparison of the results obtained with the NiACF_{HNO3-373} in the hydrogenation of *p*-CNB, to previously reported catalysts.

N°	Catalyst	d ^A (nm)	P _{tot} /P _{H₂} / Solvent	T (K)	-R _{average} ^B (mol _{NC} ·mol _{Ni} ⁻¹ ·s ⁻¹)	X _{<i>p</i>-CNB} (%)	S _{<i>p</i>-CAN} (%)	Y _{<i>p</i>-CAN} (%)	Ref.
1	RaNi+N-modifier ^C	-	NA/12/ MeOH	353	1.4x10 ⁻³	100	99.7	99.7	26
2	NiFC1	19	NA/15/ MeOH	393	8.4x10 ⁻⁴	100	99	99.0	27
3	NiC-3	-	NA/15/ MeOH	393	4.3x10 ⁻³	-	> 99	-	28
4 ^D	Ni/CNFs	11	20/NA/ EtOH	413	3.3x10 ⁻³	99	98	97.0	32
5	Ni/C (magnetic)	5–15	20/NA/ EtOH	413	2.2x10 ⁻²	100	84.5	84.5	33
6	Ni-NiO/NGr@C	10–50	NA/50/ THF:H ₂ O (1:1)	383	6.9x10 ⁻⁴	-	-	99	35
7	NiC-Ni/CNFs	20 ^E	NA/20/ EtOH	413	3.0x10 ⁻³	100	99.5	99.5	34
8 ^D	Ni/TiO ₂	20	15/NA/ EtOH	363	1.4x10 ⁻²	99.1	99.2	98.3	29
9 ^D	Ni/TiO ₂ (T773)	18	15/NA/ EtOH	353	1.4x10 ⁻³	> 98	> 98	96.0	30
10	Ni/TiO ₂ (SG-673)	34	NA/10/ EtOH	348	3.0x10 ⁻³	> 98	> 99	> 97.0 ^F	31
11	Ni/ACF _{HNO3-373}	2	10/8.5/ EtOH	353	2.2x10 ⁻²	100	99.3	99.3	This work

^A The diameter d corresponds to the average diameter given in the references or the approximate observed range.

^B The average transformation rate was calculated with equation (3.4) for the reaction time required to reach the conversion associated the highest yield given in the references.

^C The N-modifier refers to formamidine acetate.

^D *o*-CNB was tested rather than *p*-CNB.

^E Estimated from the TEM published images. The authors mentioned bigger NPs (40–60 nm) being present.

^F Based on available kinetic data, the yield could be higher.

So, we may conclude that the catalyst developed in this work demonstrated the highest efficiency under mild conditions being unprecedented result for hydrogenation of nitroaromatics.

Catalyst Stability

Catalyst stability was assessed via 13 consecutive reaction runs using the same 5 wt.% Ni/ACF_{HNO3-373} catalyst. Deactivation was more pronounced during the first run with a tendency towards stabilization after the sixth run. The total activity drop (about 45%) may be due to leaching of loosely attached Ni NPs during the first run, some mechanical losses and slow accumulation of intermediates on the catalyst surface during the following reaction runs. The post-reaction mixture was analysed using AAS and no traces of Ni were detected. Therefore, the deactivation is probably due to contamination from some residuals or due to reconstructions of active sites in the course of the hydrogenation reactions, leading to the quasi-steady-state attained after 6–7 runs.

In summary, the structured 5 wt.% Ni/ACF_{HNO3-373} catalyst is highly efficient for the 3-phase hydrogenation of nitro-aromatics tolerating different functionalities. In addition to obtaining near-quantitative yields of the desired anilines, the catalyst is reusable and simple to handle.

6.4 Conclusions

Structured catalysts consisting of small Ni NPs (~2.0 nm) supported on activated carbon fibers (ACFs) have been prepared which efficiently catalyse the chemoselective hydrogenation of nitro-aromatics under relatively mild conditions ($T = 353$ K; $P_{tot} = 10$ bar). The technique used to prepare the catalyst was optimised, with pre-treatment of the ACFs by nitric acid (prior to the impregnation by Ni-precursor) slightly affecting the Ni⁰ dispersion (1.8 nm → 2.1 nm), but creating a high concentration of functional O-groups, led to the enhanced (3-fold) activity of the resulting catalyst in the hydrogenation of *p*-CNB.

In-situ XRD and XPS analysis showed that the Ni NPs generated following reduction of the nickel salt are metallic. The TPD and H₂-TPR data allowed the optimal reduction temperature in H₂-flow of 673 K to be established and indicated the necessity for the passivated catalyst to undergo *in-situ* activation in the reaction mixture at 353 K. Although deactivation of the catalyst was observed following storage in ambient air, catalytic activity could be regenerated by *in-situ* activation in the reaction mixture at temperatures above 393 K.

The best catalytic performance was observed for 5 wt.% Ni/ACF_{HNO₃-373}, which is *ca.* 20-fold more active than the benchmark Raney Ni catalyst. Thus, the new catalyst reported here represents a significant step forward towards a simple, heterogeneous catalytic selective hydrogenation of nitroarenes that employs H₂ as the hydrogen source.

Chapter 7

General Conclusions and Outlook

7.1 Achieved results

The objective of the thesis was to develop new structured catalysts for the selective hydrogenation of nitroarenes under mild conditions. Furthermore, we wanted to use inexpensive metals like iron, cobalt or nickel and avoid using rare and expensive ones like platinum or palladium. Immobilization of active metal nanoparticles on structured supports should facilitate their potential industrial use in continuous operations. Activated carbon fibres (ACFs) were selected as support for their well-organized macro-structure, a practical feature that could enable their use in flow reactors without big pressure drop. The high porosity of ACFs was one of the sought-after properties in the support for affording the formation and stabilization of small nanoparticles and thereby surpass the current benchmark catalysts.

First, the viability of Fe, Co or Ni oxide NPs supported on ACFs as catalysts for the catalytic transfer hydrogenation (CTH) of nitroaromatics under mild conditions was first evaluated in the reduction of *para*-chloronitrobenzene (*p*-CNB) to *para*-chloroaniline (*p*-CAN) with hydrazine as reducing agent. The FeO_x/ACF and CoO_x/ACF catalysts were found to be far more active compared to the nickel analogues. While the cleavage of the Cl-C bond was avoided with all tested catalysts, only the FeO_x/ACF catalyst prevented the formation of condensation intermediates (azoxy-, azo-). STEM-HAADF imaging showed that the active metal oxide phase consists of very small nanoparticles ($d = 2$ nm), evenly distributed in the

carbonaceous matrix of the ACF. The FeO_x/ACF catalyst converted many nitroarenes to their corresponding anilines in high yield (> 93%), but led to C=C bond reduction ($Y_{m-VA} < 80\%$) during the synthesis of *meta*-vinylaniline (*m*-VA) from *meta*-nitrostyrene (*m*-NS). The CoO_x/ACF catalyst demonstrated a higher selectivity towards the NO₂ group compared to the vinyl group ($Y_{m-VA} = 98\%$), which was further improved ($Y_{m-VA} = 99.4\%$) by increasing the surface oxygen-containing groups of ACF. To the best of our knowledge, this performance is unprecedented in terms of *m*-VA yield.

The second part of this work was devoted to the development of Ni-based structured catalysts for the H₂-assisted hydrogenation of nitroaromatics. Unsupported Ni PVP-stabilized NPs in the range of 2–14 nm were synthesized and tested in the partial hydrogenation of *meta*-dinitrobenzene (*m*-DNB) to *meta*-nitroaniline (*m*-NAN) to study possible size effects. The turnover frequency increased with the NP diameter, showing this reaction to have antipathetic structure sensitivity. At contrast, the highest selectivity to *m*-NAN (96%) was obtained over the smallest (2 nm) Ni NPs after their deposition on ACFs. These NPs have the highest fraction of edge and vertex atoms, which were hypothesized to be responsible of the selectivity to *m*-NAN by enabling a vertical rather than a flat mode of *m*-DNB adsorption. The experimental kinetic results were successfully fitted with the two-sites Langmuir-Hinshelwood kinetic model. Bimetallic Ni-Au NPs afforded *m*-NAN with a yield above 98%. This catalytic performance during the partial hydrogenation of *m*-DNB was attributed to the electropositive character of Ni-sites separation induced by neighbouring Au atoms and thereby avoiding flat adsorption of *m*-DNB.

On the basis of the findings obtained from the colloidal Ni NPs, ~2 nm Ni supported on ACFs were prepared using the simple wet impregnation method and tested for the hydrogenation of nitroarenes. The passivation of the Ni NPs to avoid pyrophoric behaviour, combined with the ongoing oxidation in ambient conditions during storage, were detrimental

to the reaction rate in the hydrogenation of *p*-CNB to *p*-CAN. The creation of an oxide fraction in the nanocrystallites was found to be reversible by *in-situ* activation step in H₂ under 10 bars (P_{H2} = 8.5 bar). A temperature of 353 K was sufficient to achieve this goal for freshly prepared catalysts while 393 K was necessary for catalysts stored over an extended period of time. The carbonaceous nature of the ACF afforded the generation of O-containing surface groups that increased the specific reaction rate, *i.e.* Ni/ACF_{HNO3}, compared to non-treated Ni/ACF catalyst. Micrographs of these catalysts showed that the dispersion of the two catalyst was similar, thereby eliminating the cause due an increase of catalytic surface. The hypothesis of additional surface oxygen-containing groups in the Ni/ACF_{HNO3} catalyst, affecting electronically the nickel NPs, was retained. Finally, the Ni/ACF_{HNO3} catalyst exhibited an order of magnitude higher specific activities in the hydrogenation of *p*-CNB to *p*-CAN compared to Raney nickel catalyst commonly used in industry.

7.2 Outlook

The prepared structured catalysts consisting of non-precious metal/metal oxide nanoparticles of ~2 nm, stabilized within the network of the ACFs support, have shown to be selective and active in the partial reduction of functionalized nitroarenes. More specifically, the FeO_x/ACF and CoO_x/ACF catalysts were able to completely avoid the scission of the C-Cl bond in the hydrazine-assisted CTH of *p*-CNB into *p*-CAN ($Y_{p-CAN} \approx 100\%$), even at complete conversion. The specific activity of the Fe-based catalyst was significantly higher than the catalysts reported by Lauwiner⁶⁸ and Beller⁷⁸ groups, under similar conditions. Moreover, a *m*-VA yield above 99% in was obtained over the CoO_x/ACF_{HNO3} catalyst, which, to the best of our knowledge, has never been achieved to date. In the liquid-phase H₂-assisted hydrogenation of *p*-CNB, the 2 nm Ni NPs on ACFs showed a *p*-CAN selectivity comparable

to the system reported by Blaser,²⁶ which involved Raney nickel with additives, and surpassed by an order of magnitude the specific activity of this system. Regarding these two model reactions, the developed catalysts can be considered as benchmarks.

Nevertheless, there are incentives for possible improvements. First, to the requisite for continuous operations, is undoubtedly its mechanical and catalytic stability in liquid-phase for long period on stream. One reason of the slight but gradual deactivation of the catalyst was its erosion by losing micro-fragments over time. The optimization of this parameter is conceivable by applying chemical treatments on the ACFs. It was already shown that the strength of activated carbon could be improved by liquid phase oxidative (H_2SO_4 , HNO_3 and H_2O_2) treatment at room temperature.¹⁷⁸ This approach should be studied.

Regarding the addition of oxygen-containing groups on ACF surface, their beneficial effects on both the formation of small NPs and catalytic response was established. The amount of O-group could be controlled by HNO_3 or H_2O_2 treatment and should be addressed. For example, the selectivity in *m*-VA and the activity during *p*-CNB transformation were increased over catalysts pre-treated by HNO_3 . Despite the gain of knowledge on the reasons lying behind certain effects of these surface functionalities, part of the picture remains incomplete. A quantification of the O-containing groups of the Ni/ACF catalysts after their preparation could be useful to link their concentrations to the reaction rate. Besides, the temperature-programmed decomposition (TPD) non-destructive techniques should instead be employed. (FTIR, DRIFTS). The incorporation of nitrogen has shown promising results for enhancing the catalytic activity, selectivity and even stability of several carbon-based systems.⁴⁶ ACFs seem to be particularly appropriate since they would provide a great surface area that could lead to an intimate contact between the surface C-N species and nanoparticles. The decomposition of nitrogen-containing organic molecules (*e.g.* ethylenediamine, 1,10-phenanthroline) at high temperature is the most common approach tested so far and would be

suitable for ACFs. The challenge would be to obtain a highly dispersed active phase since the nitrogen-doping generally favours the creation of large nanoparticles.

The unsupported bimetallic Ni-Au nanoparticles have exhibited excellent catalytic properties in the hydrogenation of *m*-DNB, both in terms of selectivity and activity towards the production of *m*-NAN. Their elaborate preparation via a colloidal approach, with notably the use surfactants, is certainly too complicated for industrial applications. The impregnation of precursors within ACFs porosity followed by their pyrolysis or reduction in liquid-phase should be tested.

The transfer of discoveries made in the laboratory to an industrial scale is often mentioned in the research dedicated to the development of catalysts. However, the scaling up of new catalytic systems is laborious. Here, the ACFs being suitable for continuous operations should be tested in flow-reactors. Parameters that cannot be evaluated in semi-batch reactor, such as the catalyst stability over a prolonged duration and heat transfer issues should therefore be addressed.

Appendix

Chapter 4

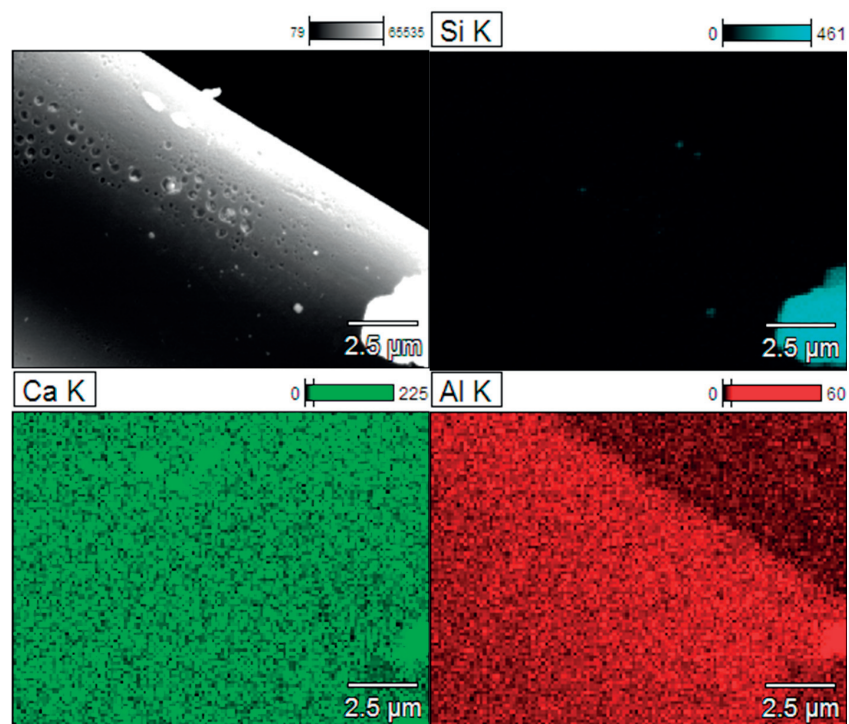


Figure S4.1. SEM images of FeO_x/ACF at high (8000 X) magnification. Fe loading (wt.%): 3.5. EDX mapping of Si, Ca and Al.

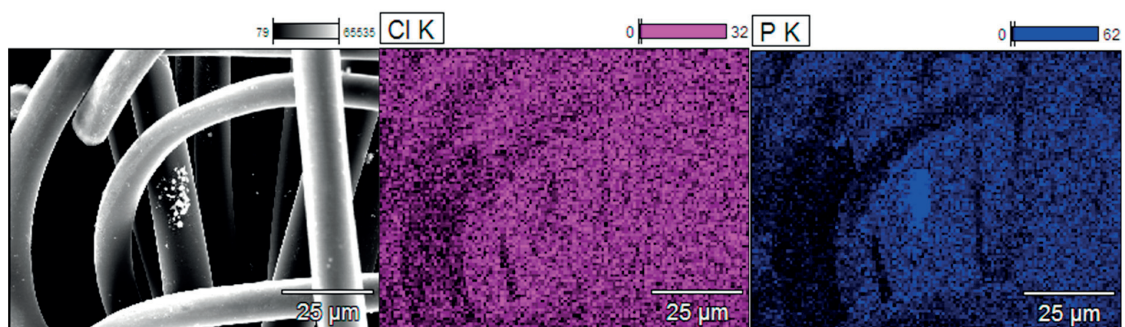


Figure S4.2. SEM images of FeO_x/ACF at high (1200 X) magnification. Fe loading (wt.%): 3.5. EDX mapping of Cl and P.

Chapter 5

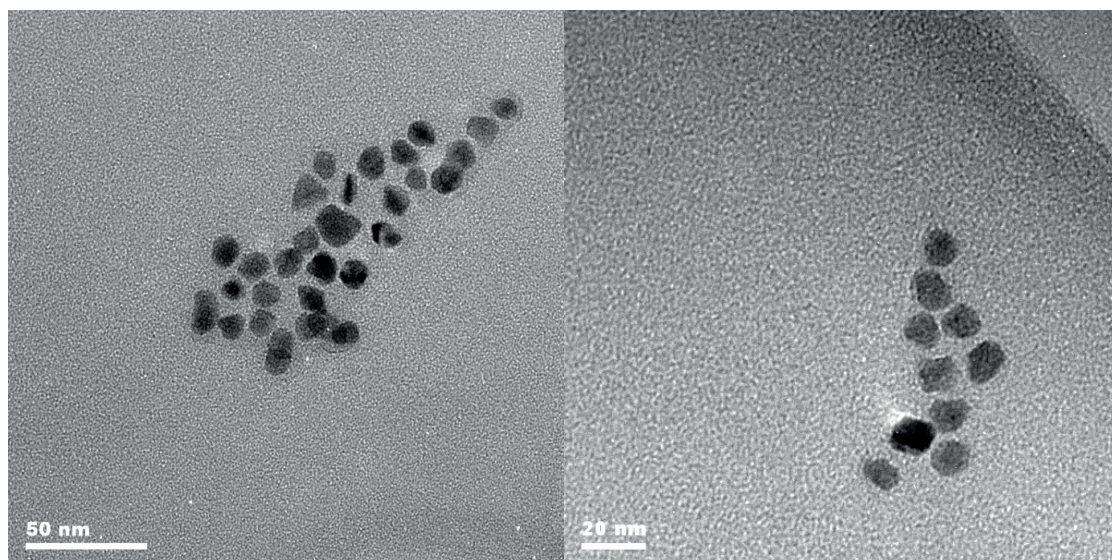


Figure S5.1. Representative TEM images of the unsupported Ni11 NPs.

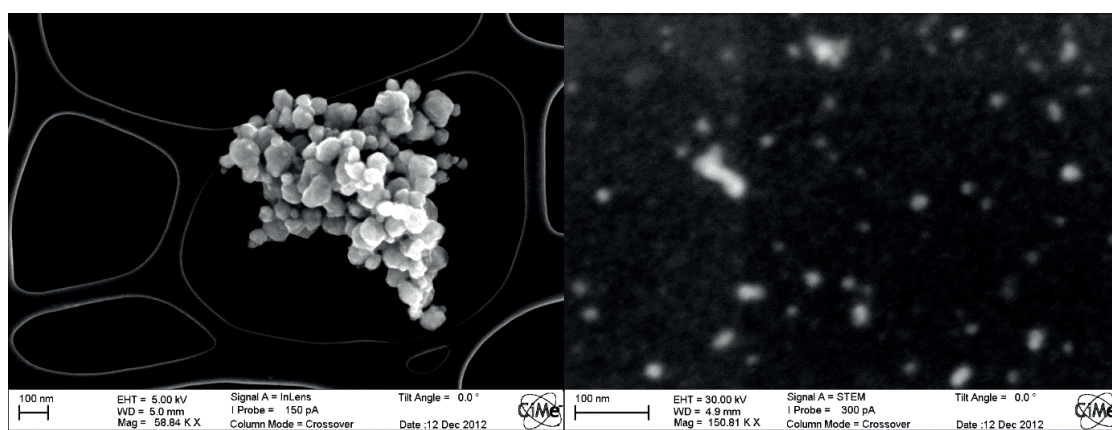


Figure S5.2. Representative (left) HRSEM and (right) STEM images (Zeiss Merlin) of the unsupported Ni14 NPs.

Chapter 6

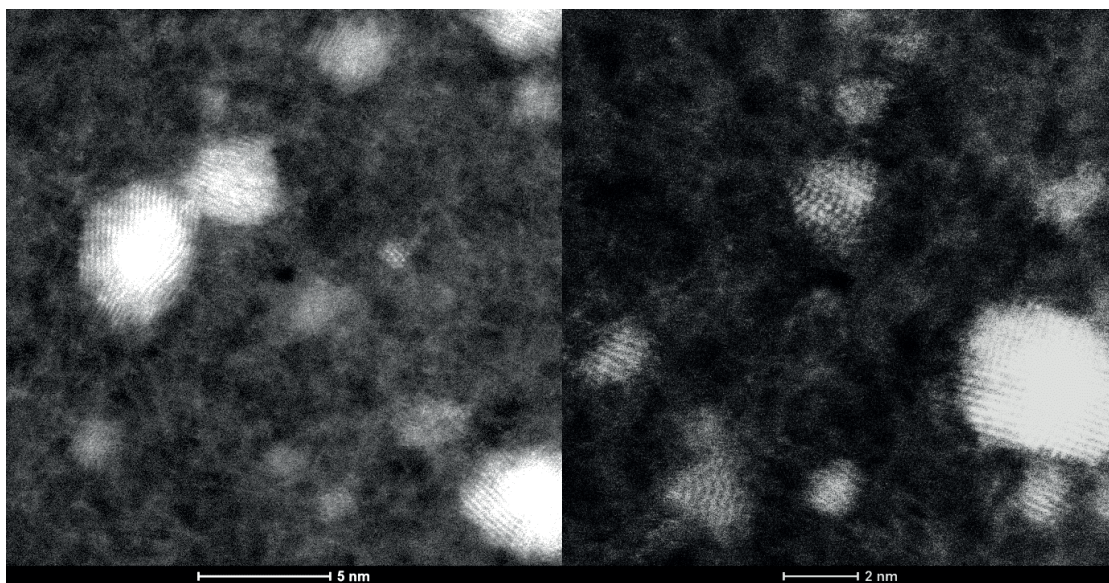


Figure S5.1. Representative STEM-HAADF images of the Ni/ACF_{HNO3-373} catalyst acquired by the FEI Titan Themis.

References

1. Kahl, T., et al., *Aniline*, in *Ullmann's Encyclopedia of Industrial Chemistry*. 2011, Wiley-VCH Verlag GmbH & Co. KGaA.
2. Popat, V. and N. Padhiyar, *Kinetic Study of Bechamp Process for P-Nitrotoluene Reduction to P-Toluidine*. *International Journal of Chemical Engineering and Applications*, 2013. **4**(6): p. 401-405.
3. Travis, A.S., *Manufacture and uses of the Anilines: A Vast Array of Processes and Products*, in *The Chemistry of Anilines*. 2007, John Wiley & Sons, Ltd. p. 715-782.
4. Gelder, E.A., S.D. Jackson, and C.M. Lok, *The hydrogenation of nitrobenzene to aniline: a new mechanism*. *Chemical Communications*, 2005(4): p. 522-524.
5. Smith, G.V., et al., *Hydrogenation of Nitrosobenzene over Palladium Catalysts*. *Catalysis of Organic Reactions*, 1994. **53**: p. 137-149.
6. Baumeister, P., H.U. Blaser, and M. Studer, *Strong reduction of hydroxylamine accumulation in the catalytic hydrogenation of nitroarenes by vanadium promoters*. *Catalysis Letters*, 1997. **49**(3-4): p. 219-222.
7. Figueras, F. and B. Coq, *Hydrogenation and hydrogenolysis of nitro-, nitroso-, azo-, azoxy- and other nitrogen-containing compounds on palladium*. *Journal of Molecular Catalysis a-Chemical*, 2001. **173**(1-2): p. 223-230.
8. Wisniak, J. and M. Klein, *Reduction of Nitrobenzene to Aniline*. *Industrial & Engineering Chemistry Product Research and Development*, 1984. **23**(1): p. 44-50.
9. Sheng, T., et al., *Insights into the mechanism of nitrobenzene reduction to aniline over Pt catalyst and the significance of the adsorption of phenyl group on kinetics*. *Chemical Engineering Journal*, 2016. **293**: p. 337-344.
10. Dumesic, J.A., G.W. Huber, and M. Boudart, *Principles of Heterogeneous Catalysis*, in *Handbook of Heterogeneous Catalysis*. 2008, Wiley-VCH Verlag GmbH & Co. KGaA.
11. National Research Council (U.S.). Panel on New Directions in Catalytic Science and Technology., *Catalysis looks to the future*. 1992, Washington, D.C.: National Academy Press. viii, 86 p.
12. Nerozzi, F., *Heterogeneous Catalytic Hydrogenation Platinum group metals as hydrogenation catalysts in a two-day course*. *Platinum Metals Review*, 2012. **56**(4): p. 236-241.
13. Roessler, F., *Catalytic hydrogenation in the liquid phase*. *Chimia*, 2003. **57**(12): p. 791-798.
14. Harry, J.T. and V.C. Edward, *Catalytic hydrogenation of nitro aromatic compounds to produce the corresponding amino compounds*, 1966, Google Patents.
15. Gonzalez, R.A., *Hydrogenation of aromatic nitro compounds*, 1970, Google Patents.
16. Blaser, H.U., H. Steiner, and M. Studer, *Selective Catalytic Hydrogenation of Functionalized Nitroarenes: An Update*. *Chemcatchem*, 2009. **1**(2): p. 210-221.
17. Ferrier, G.G. and F. King, *A New Platinum Catalyst for the Hydrogenation of Halonitroaromatics*. *Platinum Metals Review*, 1983. **27**(2): p. 72-77.
18. Auer, E., et al., *New catalytic systems for the selective hydrogenation of halogenated aromatic nitro compounds*. *Catalysis of Organic Reactions*, 1998. **75**: p. 551-558.
19. Corma, A. and P. Serna, *Chemoselective hydrogenation of nitro compounds with supported gold catalysts*. *Science*, 2006. **313**(5785): p. 332-334.
20. Serna, P. and A. Corma, *Transforming Nano Metal Nonselective Particulates into Chemoselective Catalysts for Hydrogenation of Substituted Nitrobenzenes*. *Acs Catalysis*, 2015. **5**(12): p. 7114-7121.
21. Chen, Y.Y., et al., *Ag/SiO₂: A novel catalyst with high activity and selectivity for hydrogenation of chloronitrobenzenes*. *Chemical Communications*, 2005(42): p. 5298-5300.

References

22. Chen, Y.Y., et al., *Preparation and application of highly dispersed gold nanoparticles supported on silica for catalytic hydrogenation of aromatic nitro compounds*. Journal of Catalysis, 2006. **242**(1): p. 227-230.
23. He, D.P., et al., *Synthesis of chloroanilines: selective hydrogenation of the nitro in chloronitrobenzenes over zirconia-supported gold catalyst*. Green Chemistry, 2007. **9**(8): p. 849-851.
24. Sabatier, P. and A. Mailhe, *The direct reduction of aromatic halogen derivatives by divided nickel and hydrogen*. Comptes Rendus Hebdomadaires Des Seances De L Academie Des Sciences, 1904. **138**: p. 245-249.
25. Winans, C.F., *Nickel as a Catalyst for the Hydrogenation of Aromatic Halogen Compounds*. Journal of the American Chemical Society, 1939. **61**(12): p. 3564-3565.
26. Baumeister, P., H.U. Blaser, and W. Scherrer, *Chemoselective Hydrogenation of Aromatic Chloronitro Compounds with Amidine Modified Nickel Catalysts*, in *Studies in Surface Science and Catalysis*, J.B.C.B.D.D.G.P.R.M. M. Guisnet and C. Montassier, Editors. 1991, Elsevier. p. 321-328.
27. Mahata, N., et al., *Hydrogenation of chloronitrobenzenes over filamentous carbon stabilized nickel nanoparticles*. Catalysis Communications, 2009. **10**(8): p. 1203-1206.
28. Mahata, N., et al., *Simultaneous Elimination of Pyrophoricity and Enhancement of Activity of Raney Nickel by Carbon Deposition: Synthesis of Highly Active NiC Catalysts*. Chemcatchem, 2010. **2**(3): p. 330-335.
29. Xiong, J., J.X. Chen, and J.Y. Zhang, *Liquid-phase hydrogenation of o-chloronitrobenzene over supported nickel catalysts*. Catalysis Communications, 2007. **8**(3): p. 345-350.
30. Yao, N., et al., *Influence of support calcination temperature on properties of Ni/TiO₂ for catalytic hydrogenation of o-chloronitrobenzene to o-chloroaniline*. Catalysis Communications, 2008. **9**(6): p. 1510-1516.
31. Chen, J.X., et al., *Hydrogenation of chloronitrobenzene to chloroaniline over Ni/TiO₂ catalysts prepared by sol-gel method*. Chemical Engineering Journal, 2009. **148**(1): p. 164-172.
32. Wang, C., et al., *Carbon nanofiber supported Ni catalysts for the hydrogenation of chloronitrobenzenes*. Catalysis Communications, 2008. **9**(8): p. 1749-1753.
33. Zhang, P., et al., *Magnetically recoverable Ni/C catalysts with hierarchical structure and high-stability for selective hydrogenation of nitroarenes*. Physical Chemistry Chemical Physics, 2015. **17**(1): p. 145-150.
34. Kang, J., et al., *In situ synthesis of nickel carbide-promoted nickel/carbon nanofibers nanocomposite catalysts for catalytic applications*. Chemical Engineering Journal, 2015. **275**: p. 36-44.
35. Pisiewicz, S., et al., *Synthesis of Nickel Nanoparticles with N-Doped Graphene Shells for Catalytic Reduction Reactions*. Chemcatchem, 2016. **8**(1): p. 129-134.
36. Campos, C.H., et al., *Chemoselective hydrogenation of o-, p- and m-chloronitrobenzene at ambient temperature on Au/Fe₂O₃ catalysts*. Applied Catalysis a-General, 2014. **482**: p. 127-136.
37. Cardenas-Lizana, F., et al., *Gold nano-particles supported on hematite and magnetite as highly selective catalysts for the hydrogenation of nitro-aromatics*. International Journal of Nanotechnology, 2012. **9**(1-2): p. 92-112.
38. Niu, H.L., et al., *Iron Oxide as a Catalyst for Nitroarene Hydrogenation: Important Role of Oxygen Vacancies*. Industrial & Engineering Chemistry Research, 2016. **55**(31): p. 8527-8533.
39. Jagadeesh, R.V., et al., *Nanoscale Fe₂O₃-Based Catalysts for Selective Hydrogenation of Nitroarenes to Anilines*. Science, 2013. **342**(6162): p. 1073-1076.
40. Westerhaus, F.A., et al., *Heterogenized cobalt oxide catalysts for nitroarene reduction by pyrolysis of molecularly defined complexes*. Nature Chemistry, 2013. **5**(6): p. 537-543.
41. Wang, X. and Y.W. Li, *Chemoselective hydrogenation of functionalized nitroarenes using MOF-derived co-based catalysts*. Journal of Molecular Catalysis a-Chemical, 2016. **420**: p. 56-65.

42. Wei, Z.Z., et al., *In Situ-Generated Co₀-Co₃O₄/N-Doped Carbon Nanotubes Hybrids as Efficient and Chemoselective Catalysts for Hydrogenation of Nitroarenes*. *Acs Catalysis*, 2015. **5**(8): p. 4783-4789.
43. Liu, L.C., P. Concepcion, and A. Corma, *Non-noble metal catalysts for hydrogenation: A facile method for preparing Co nanoparticles covered with thin layered carbon*. *Journal of Catalysis*, 2016. **340**: p. 1-9.
44. Chen, B.F., et al., *Recyclable and Selective Nitroarene Hydrogenation Catalysts Based on Carbon-Coated Cobalt Oxide Nanoparticles*. *Chemcatchem*, 2016. **8**(6): p. 1132-1138.
45. Xing, L., et al., *A new approach to high performance Co/C catalysts for selective hydrogenation of chloronitrobenzenes*. *Journal of Catalysis*, 2007. **250**(2): p. 369-372.
46. He, L., et al., *Synthesis, Characterization, and Application of Metal Nanoparticles Supported on Nitrogen-Doped Carbon: Catalysis beyond Electrochemistry*. *Angewandte Chemie-International Edition*, 2016. **55**(41): p. 12582-12594.
47. Siegrist, U., et al., *The selective hydrogenation of functionalized nitroarenes: New catalytic systems*. *Catalysis of Organic Reactions*, 1998. **75**: p. 207-219.
48. Kosak, J.R., *HYDROGENATION OF HALOAROMATIC NITRO COMPOUNDS A2* - Jones, William H, in *Catalysis in Organic Syntheses*. 1980, Academic Press. p. 107-117.
49. Yarulin, A., et al., *Increasing Pt selectivity to vinylaniline by alloying with Zn via reactive metal-support interaction*. *Catalysis Today*, 2015. **256**: p. 241-249.
50. Wei, H.S., et al., *FeOx-supported platinum single-atom and pseudo-single-atom catalysts for chemoselective hydrogenation of functionalized nitroarenes*. *Nature Communications*, 2014. **5**.
51. Knoevenagel, E. and B. Bergdolt, *On the behaviour of Delta(2-5)-dihydroterephthalic acid dimethylesters in high temperatures and in the presence of anodised palladium*. *Berichte Der Deutschen Chemischen Gesellschaft*, 1903. **36**: p. 2857-2860.
52. Braude, E.A. and R.P. Linstead, *Hydrogen Transfer .1. Introductory Survey*. *Journal of the Chemical Society*, 1954(Oct): p. 3544-3547.
53. Johnstone, R.A.W., A.H. Wilby, and I.D. Entwistle, *Heterogeneous Catalytic Transfer Hydrogenation and Its Relation to Other Methods for Reduction of Organic-Compounds*. *Chemical Reviews*, 1985. **85**(2): p. 129-170.
54. Sanfilippo, D. and P.N. Rylander, *Hydrogenation and Dehydrogenation*, in *Ullmann's Encyclopedia of Industrial Chemistry*. 2000, Wiley-VCH Verlag GmbH & Co. KGaA.
55. Schirmann, J.-P. and P. Bourdauducq, *Hydrazine*, in *Ullmann's Encyclopedia of Industrial Chemistry*. 2000, Wiley-VCH Verlag GmbH & Co. KGaA.
56. Wienhofer, G., et al., *General and Selective Iron-Catalyzed Transfer Hydrogenation of Nitroarenes without Base*. *Journal of the American Chemical Society*, 2011. **133**(32): p. 12875-12879.
57. Jagadeesh, R.V., et al., *Highly selective transfer hydrogenation of functionalised nitroarenes using cobalt-based nanocatalysts*. *Green Chemistry*, 2015. **17**(2): p. 898-902.
58. Jagadeesh, R.V., et al., *Nitrogen-Doped Graphene-Activated Iron-Oxide-Based Nanocatalysts for Selective Transfer Hydrogenation of Nitroarenes*. *Acs Catalysis*, 2015. **5**(3): p. 1526-1529.
59. Datta, K.J., et al., *Base-Free Transfer Hydrogenation of Nitroarenes Catalyzed by Micro-Mesoporous Iron Oxide*. *Chemcatchem*, 2016. **8**(14): p. 2351-2355.
60. Mohapatra, S.K., et al., *Heterogeneous catalytic transfer hydrogenation of aromatic nitro and carbonyl compounds over cobalt(II) substituted hexagonal mesoporous aluminophosphate molecular sieves*. *Tetrahedron Letters*, 2002. **43**(47): p. 8527-8529.
61. Mohapatra, S.K., et al., *Reductive cleavage of azo dyes and reduction of nitroarenes over trivalent iron incorporated hexagonal mesoporous aluminophosphate molecular sieves*. *Applied Catalysis B-Environmental*, 2003. **46**(1): p. 155-163.
62. Selvam, P., et al., *Chemo- and regioselective reduction of nitroarenes, carbonyls and azo dyes over nickel-incorporated hexagonal mesoporous aluminophosphate molecular sieves*. *Tetrahedron Letters*, 2004. **45**(9): p. 2003-2007.

References

63. Shi, Q.X., et al., *Simple and eco-friendly reduction of nitroarenes to the corresponding aromatic amines using polymer-supported hydrazine hydrate over iron oxide hydroxide catalyst*. *Green Chemistry*, 2006. **8**(10): p. 868-870.
64. Liu, X., et al., *Mild, selective and switchable transfer reduction of nitroarenes catalyzed by supported gold nanoparticles*. *Catalysis Science & Technology*, 2013. **3**(12): p. 3200-3206.
65. Sanjini, N.S. and S. Velmathi, *Iron impregnated SBA-15, a mild and efficient catalyst for the catalytic hydride transfer reduction of aromatic nitro compounds*. *Rsc Advances*, 2014. **4**(30): p. 15381-15388.
66. Nunes, R.C., M.H. Araujo, and E.N. dos Santos, *The unique behavior of the catalytic system Pd(OAc)₂/N-heterocyclic carbene on the telomerization of isoprene with methanol*. *Catalysis Communications*, 2007. **8**(11): p. 1798-1802.
67. Hirashima, T. and O. Manabe, *Catalytic Reduction of Aromatic Nitro-Compounds with Hydrazine in Presence of Iron(III) Chloride and Active Carbon*. *Chemistry Letters*, 1975(3): p. 259-260.
68. Lauwiner, M., P. Rys, and J. Wissmann, *Reduction of aromatic nitro compounds with hydrazine hydrate in the presence of an iron oxide hydroxide catalyst. I. The reduction of monosubstituted nitrobenzenes with hydrazine hydrate in the presence of ferrihydrite*. *Applied Catalysis a-General*, 1998. **172**(1): p. 141-148.
69. Kim, S., E. Kim, and B.M. Kim, *Fe₃O₄ Nanoparticles: A Conveniently Reusable Catalyst for the Reduction of Nitroarenes Using Hydrazine Hydrate*. *Chemistry-an Asian Journal*, 2011. **6**(8): p. 1921-1925.
70. Cantillo, D., M.M. Moghaddam, and C.O. Kappe, *Hydrazine-mediated Reduction of Nitro and Azide Functionalities Catalyzed by Highly Active and Reusable Magnetic Iron Oxide Nanocrystals*. *Journal of Organic Chemistry*, 2013. **78**(9): p. 4530-4542.
71. Miura, M., M. Shinohara, and M. Nomura, *Cobalt-Catalyzed Reduction of Aromatic Nitro-Compounds*. *Journal of Molecular Catalysis*, 1988. **45**(2): p. 151-153.
72. Sharma, U., et al., *Highly Chemo- and Regioselective Reduction of Aromatic Nitro Compounds Catalyzed by Recyclable Copper(II) as well as Cobalt(II) Phthalocyanines*. *Advanced Synthesis & Catalysis*, 2010. **352**(11-12): p. 1834-1840.
73. Braden, R., H. Knupfer, and H. Ziemann, *Process for the preparation of unsaturated amino compounds*, 1977, Google Patents.
74. Baumeister, P. and U. Siegrist, *Process for the preparation of unsaturated amino compounds*, 1999, Google Patents.
75. Zhu, H.Z., et al., *Selective hydrogenation of nitroaromatics by ceria nanorods*. *Nanoscale*, 2013. **5**(16): p. 7219-7223.
76. Guha, N.R., D. Bhattacharjee, and P. Das, *Solid supported rhodium(0) nanoparticles: an efficient catalyst for chemo- and regio-selective transfer hydrogenation of nitroarenes to anilines under microwave irradiation*. *Tetrahedron Letters*, 2014. **55**(18): p. 2912-2916.
77. Singh, A., T. Raj, and N. Singh, *Highly Selective and Efficient Reduction of Nitroarenes by Imidazolium Salt Stabilized Copper Nanoparticles in Aqueous Medium*. *Catalysis Letters*, 2015. **145**(8): p. 1606-1611.
78. Jagadeesh, R.V., et al., *Efficient and highly selective iron-catalyzed reduction of nitroarenes*. *Chemical Communications*, 2011. **47**(39): p. 10972-10974.
79. Cybulski, A. and J.A. Moulijn, *Structured catalysts and reactors*. 2nd ed. Chemical industries. 2006, Boca Raton: Taylor & Francis. xix, 829 p.
80. He, Y.Q., et al., *Metal nanoparticles supported graphene oxide 3D porous monoliths and their excellent catalytic activity*. *Materials Chemistry and Physics*, 2012. **134**(2-3): p. 585-589.
81. Verho, O., et al., *Mild and Selective Hydrogenation of Nitro Compounds using Palladium Nanoparticles Supported on Amino-Functionalized Mesocellular Foam*. *Chemcatchem*, 2014. **6**(11): p. 3153-3159.
82. Verho, O., et al., *Nanopalladium on Amino-Functionalized Mesocellular Foam as an Efficient and Recyclable Catalyst for the Selective Transfer Hydrogenation of Nitroarenes to Anilines*. *Chemcatchem*, 2014. **6**(1): p. 205-211.

-
83. Holler, V., et al., *Bubble columns staged with structured fibrous catalytic layers: Residence time distribution and mass transfer*. *Industrial & Engineering Chemistry Research*, 2001. **40**(6): p. 1575-1579.
84. Holler, V., et al., *Three-phase nitrobenzene hydrogenation over supported glass fiber catalysts: Reaction kinetics study*. *Chemical Engineering & Technology*, 2000. **23**(3): p. 251-255.
85. Tomasic, V. and F. Jovic, *State-of-the-art in the monolithic catalysts/reactors*. *Applied Catalysis a-General*, 2006. **311**: p. 112-121.
86. Twigg, M.V. and J.T. Richardson, *Theory and applications of ceramic foam catalysts*. *Chemical Engineering Research & Design*, 2002. **80**(A2): p. 183-189.
87. Richardson, J.T., Y. Peng, and D. Remue, *Properties of ceramic foam catalyst supports: pressure drop*. *Applied Catalysis a-General*, 2000. **204**(1): p. 19-32.
88. De Jong, K.P. and J.W. Geus, *Carbon nanofibers: Catalytic synthesis and applications*. *Catalysis Reviews-Science and Engineering*, 2000. **42**(4): p. 481-510.
89. Parmon, V.N., et al., *New Catalysts and Catalytic Processes to Produce Hydrogen and Syngas from Natural gas and other Light Hydrocarbons*, in *Studies in Surface Science and Catalysis*, D.S.F.F.A.V. A. Parmaliana and F. Arena, Editors. 1998, Elsevier. p. 677-684.
90. Auer, E., et al., *Carbons as supports for industrial precious metal catalysts*. *Applied Catalysis a-General*, 1998. **173**(2): p. 259-271.
91. Matatov-Meytal, Y. and M. Sheintuch, *Catalytic fibers and cloths*. *Applied Catalysis a-General*, 2002. **231**(1-2): p. 1-16.
92. Mochida, I., et al., *Removal of SO_x and NO_x over activated carbon fibers*. *Carbon*, 2000. **38**(2): p. 227-239.
93. Figueiredo, J.L., et al., *Modification of the surface chemistry of activated carbons*. *Carbon*, 1999. **37**(9): p. 1379-1389.
94. Boehm, H.P., *Some Aspects of the Surface-Chemistry of Carbon-Blacks and Other Carbons*. *Carbon*, 1994. **32**(5): p. 759-769.
95. Pradoburguete, C., et al., *Effect of Carbon Support and Mean Pt Particle-Size on Hydrogen Chemisorption by Carbon-Supported Pt Catalysts*. *Journal of Catalysis*, 1991. **128**(2): p. 397-404.
96. Pradoburguete, C., et al., *The Effect of Oxygen-Surface Groups of the Support on Platinum Dispersion in Pt/Carbon Catalysts*. *Journal of Catalysis*, 1989. **115**(1): p. 98-106.
97. Nieto-Marquez, A., et al., *Gas phase hydrogenation of nitrobenzene over acid treated structured and amorphous carbon supported Ni catalysts*. *Applied Catalysis a-General*, 2009. **363**(1-2): p. 188-198.
98. Dongil, A.B., et al., *Synthesis of palladium nanoparticles over graphite oxide and carbon nanotubes by reduction in ethylene glycol and their catalytic performance on the chemoselective hydrogenation of para-chloronitrobenzene*. *Applied Catalysis a-General*, 2016. **513**: p. 89-97.
99. Tauster, S.J., S.C. Fung, and R.L. Garten, *Strong Metal-Support Interactions - Group-8 Noble-Metals Supported on TiO₂*. *Journal of the American Chemical Society*, 1978. **100**(1): p. 170-175.
100. Tauster, S.J., *Strong Metal-Support Interactions*. *Accounts of Chemical Research*, 1987. **20**(11): p. 389-394.
101. Boronat, M., et al., *A molecular mechanism for the chemoselective hydrogenation of substituted nitroaromatics with nanoparticles of gold on TiO₂ catalysts: A cooperative effect between gold and the support*. *Journal of the American Chemical Society*, 2007. **129**(51): p. 16230-16237.
102. Joyner, R.W., et al., *Metal Support Interactions in Heterogeneous Catalysis*. *Surface Science*, 1984. **138**(1): p. 84-94.
103. Derbyshire, F.J., et al., *The Influence of Surface Functionality on the Activity of Carbon-Supported Catalysts*. *Applied Catalysis*, 1986. **27**(1): p. 117-131.

References

104. Gong, T., et al., *Activated Carbon Supported Palladium Nanoparticle Catalysts Synthesized by Atomic Layer Deposition: Genesis and Evolution of Nanoparticles and Tuning the Particle Size*. Journal of Physical Chemistry C, 2015. **119**(21): p. 11544-11556.
105. Toebes, M.L., et al., *Support effects in the hydrogenation of cinnamaldehyde over carbon nanofiber-supported platinum catalysts: characterization and catalysis*. Journal of Catalysis, 2004. **226**(1): p. 215-225.
106. Rodrigues, E.G., et al., *Influence of activated carbon surface chemistry on the activity of Au/AC catalysts in glycerol oxidation*. Journal of Catalysis, 2011. **281**(1): p. 119-127.
107. Wang, L., et al., *Significant catalytic effects induced by the electronic interactions between carboxyl and hydroxyl group modified carbon nanotube supports and vanadium species for NO reduction with NH₃ at low temperature*. Chemical Engineering Journal, 2014. **254**: p. 399-409.
108. Zhu, Z.H., et al., *The role of carbon surface chemistry in N₂O conversion to N₂ over Ni catalyst supported on activated carbon*. Catalysis Today, 1999. **53**(4): p. 669-681.
109. Boudart, M., *Turnover Rates in Heterogeneous Catalysis*. Chemical Reviews, 1995. **95**(3): p. 661-666.
110. Vanharde.R and F. Hartog, *Statistics of Surface Atoms and Surface Sites on Metal Crystals*. Surface Science, 1969. **15**(2): p. 189-&.
111. Bond, G.C. and D.T. Thompson, *Catalysis by gold*. Catalysis Reviews-Science and Engineering, 1999. **41**(3-4): p. 319-388.
112. Coq, B. and F. Figueras, *Structure-activity relationships in catalysis by metals: some aspects of particle size, bimetallic and supports effects*. Coordination Chemistry Reviews, 1998. **178**: p. 1753-1783.
113. Rosenthal, D., et al., *Combined XPS and TPD study of oxygen-functionalized carbon nanofibers grown on sintered metal fibers*. Carbon, 2010. **48**(6): p. 1835-1843.
114. Brunauer, S., P.H. Emmett, and E. Teller, *Adsorption of gases in multimolecular layers*. Journal of the American Chemical Society, 1938. **60**: p. 309-319.
115. Travis, A.S., *Anilines: Historical Background*, in *The Chemistry of Anilines*. 2007, John Wiley & Sons, Ltd. p. 1-73.
116. Gawande, M.B., et al., *First application of core-shell Ag@Ni magnetic nanocatalyst for transfer hydrogenation reactions of aromatic nitro and carbonyl compounds*. Rsc Advances, 2013. **3**(4): p. 1050-1054.
117. de Miguel, S.R., et al., *Preparation of Pt catalysts supported on activated carbon felts (ACF)*. Applied Catalysis a-General, 2002. **232**(1-2): p. 237-246.
118. Perez, M.C.M., C.S.M. deLecea, and A.L. Solano, *Platinum supported on activated carbon cloths as catalyst for nitrobenzene hydrogenation*. Applied Catalysis a-General, 1997. **151**(2): p. 461-475.
119. Zhu, J.J., et al., *Supported Cobalt Oxide Nanoparticles As Catalyst for Aerobic Oxidation of Alcohols in Liquid Phase*. Acs Catalysis, 2011. **1**(4): p. 342-347.
120. Brundle, C.R., T.J. Chuang, and K. Wandelt, *Core and Valence Level Photoemission Studies of Iron-Oxide Surfaces and Oxidation of Iron*. Surface Science, 1977. **68**(1): p. 459-468.
121. Zhang, X., et al., *Structural evolution and characteristics of the phase transformations between alpha-Fe₂O₃, Fe₃O₄ and gamma-Fe₂O₃ nanoparticles under reducing and oxidizing atmospheres*. Crystengcomm, 2013. **15**(40): p. 8166-8172.
122. Biesinger, M.C., et al., *Resolving surface chemical states in XPS analysis of first row transition metals, oxides and hydroxides: Cr, Mn, Fe, Co and Ni*. Applied Surface Science, 2011. **257**(7): p. 2717-2730.
123. Cantillo, D., M. Baghbanzadeh, and C.O. Kappe, *In Situ Generated Iron Oxide Nanocrystals as Efficient and Selective Catalysts for the Reduction of Nitroarenes using a Continuous Flow Method*. Angewandte Chemie-International Edition, 2012. **51**(40): p. 10190-10193.
124. Kumbhar, P.S., et al., *Mg-Fe hydrotalcite as a catalyst for the reduction of aromatic nitro compounds with hydrazine hydrate*. Journal of Catalysis, 2000. **191**(2): p. 467-473.
125. Benz, M., A.M. van der Kraan, and R. Prins, *Reduction of aromatic nitrocompounds with hydrazine hydrate in the presence of an iron oxide hydroxide catalyst - II. Activity, X-ray*

- diffraction and Mossbauer study of the iron oxide hydroxide catalyst*. Applied Catalysis a-General, 1998. **172**(1): p. 149-157.
126. Lamani, M., G.S. Ravikumara, and K.R. Prabhu, *Iron(III) Chloride-Catalysed Aerobic Reduction of Olefins using Aqueous Hydrazine at Ambient Temperature*. Advanced Synthesis & Catalysis, 2012. **354**(8): p. 1437-1442.
127. Crozier, P.A., *Nanocharacterization of Heterogeneous Catalysts by Ex Situ and In Situ STEM*, in *Scanning Transmission Electron Microscopy: Imaging and Analysis*, S.J. Pennycook and P.D. Nellist, Editors. 2011, Springer New York: New York, NY. p. 537-582.
128. Kirkland, E.J., *Advanced computing in electron microscopy*. 1998, New York: Plenum Press. ix, 250 p.
129. Nellist, P.D. and S.J. Pennycook, *Direct imaging of the atomic configuration of ultradispersed catalysts*. Science, 1996. **274**(5286): p. 413-415.
130. Serp, P. and J.L. Figueiredo, *Carbon materials for catalysis*. 2009, Hoboken, N.J.: John Wiley & Sons. xxi, 579 p.
131. Wang, J.H., et al., *Hydrogenation of Nitrobenzene to Aniline over Silica Gel Supported Nickel Catalysts*. Industrial & Engineering Chemistry Research, 2010. **49**(10): p. 4664-4669.
132. Raj, K.J.A., et al., *Liquid Phase Hydrogenation of Nitrobenzene over Nickel Supported on Titania*. Chinese Journal of Catalysis, 2012. **33**(8): p. 1299-1305.
133. Du, Y. and R. Chen, *Effect of nickel particle size on alumina supported nickel catalysts for p-nitrophenol hydrogenation*. Chemical and Biochemical Engineering Quarterly, 2007. **21**(3): p. 251-255.
134. Kalbasi, R.J., A.A. Nourbakhsh, and F. Babaknezhad, *Synthesis and characterization of Ni nanoparticles-polyvinylamine/SBA-15 catalyst for simple reduction of aromatic nitro compounds*. Catalysis Communications, 2011. **12**(11): p. 955-960.
135. Claus, P., et al., *Supported gold nanoparticles from quantum dot to mesoscopic size scale: Effect of electronic and structural properties on catalytic hydrogenation of conjugated functional groups*. Journal of the American Chemical Society, 2000. **122**(46): p. 11430-11439.
136. Rodriguez, D., et al., *Mutations in the Fanconi anaemia group C gene in the State of Sao Paulo-Brazil*. Blood, 1999. **94**(10): p. 19b-19b.
137. Semagina, N. and L. Kiwi-Minsker, *Recent Advances in the Liquid-Phase Synthesis of Metal Nanostructures with Controlled Shape and Size for Catalysis*. Catalysis Reviews-Science and Engineering, 2009. **51**(2): p. 147-217.
138. Bennett, C.O. and M. Che, *Some Geometric Aspects of Structure Sensitivity*. Journal of Catalysis, 1989. **120**(2): p. 293-302.
139. Sinfelt, J.H., *Bimetallic catalysts : discoveries, concepts, and applications*. 1983, New York: Wiley. xi, 164 p.
140. Nielsen, L.P., et al., *Initial Growth of Au on Ni(110) - Surface Alloying of Immiscible Metals*. Physical Review Letters, 1993. **71**(5): p. 754-757.
141. Besenbacher, F., et al., *Design of a surface alloy catalyst for steam reforming*. Science, 1998. **279**(5358): p. 1913-1915.
142. Singh, A.K. and Q. Xu, *Synergistic Catalysis over Bimetallic Alloy Nanoparticles*. Chemcatchem, 2013. **5**(3): p. 652-676.
143. Narayanamoorthy, B., et al., *Pt3M (M: Co, Ni and Fe) Bimetallic Alloy Nanoclusters as Support-Free Electrocatalysts with Improved Activity and Durability for Dioxygen Reduction in PEM Fuel Cells*. Electrocatalysis, 2016. **7**(5): p. 400-410.
144. Diodati, S., et al., *Oxygen reduction reaction and X-ray photoelectron spectroscopy characterisation of carbon nitride-supported bimetallic electrocatalysts*. Electrochimica Acta, 2016. **215**: p. 398-409.
145. Kimling, J., et al., *Turkevich method for gold nanoparticle synthesis revisited*. The journal of physical chemistry. B, 2006. **110**(32): p. 15700-7.
146. Xia, Y., et al., *Shape-controlled synthesis of metal nanocrystals: simple chemistry meets complex physics?* Angewandte Chemie Int Ed Engl, 2009. **48**(1): p. 60-103.
147. Singh, U.K. and M.A. Vannice, *Kinetics of liquid-phase hydrogenation reactions over supported metal catalysts - a review*. Applied Catalysis a-General, 2001. **213**(1): p. 1-24.

References

148. Bertero, N.M., et al., *Solvent effect in the liquid-phase hydrogenation of acetophenone over Ni/SiO₂: A comprehensive study of the phenomenon*. Applied Catalysis a-General, 2011. **394**(1-2): p. 228-238.
149. Augustine, R.L., R.W. Warner, and M.J. Melnick, *Heterogeneous Catalysis in Organic-Chemistry .3. Competitive Adsorption of Solvents during Alkene Hydrogenations*. Journal of Organic Chemistry, 1984. **49**(25): p. 4853-4856.
150. Drelinkiewicz, A., et al., *Acetophenone Hydrogenation on Polymer-Palladium Catalysts. The Effect of Polymer Matrix*. Catalysis Letters, 2004. **94**(3-4): p. 143-156.
151. Ma, L., et al., *Effect of Solvent Polarity Properties on the Selectivity and Activity for 3,4-Dichloronitrobenzene Hydrogenation over Pd/C Catalyst*. Advanced Materials Research, 2011. **396-398**: p. 2379-2383.
152. Che, M. and C.O. Bennett, *The Influence of Particle-Size on the Catalytic Properties of Supported Metals*. Advances in Catalysis, 1989. **36**: p. 55-172.
153. Ruta, M., N. Semagina, and L. Kiwi-Minsker, *Monodispersed Pd Nanoparticles for Acetylene Selective Hydrogenation: Particle Size and Support Effects*. The Journal of Physical Chemistry C, 2008. **112**(35): p. 13635-13641.
154. Van Hardeveld, R. and F. Hartog, Surface Science, 1969. **15**: p. 189-230.
155. Hub, S., L. Hilaire, and R. Touroude, *Hydrogenation of but-1-yne and but-1-ene on Palladium Catalysts - Particle-Size Effect*. Applied Catalysis, 1988. **36**(1-2): p. 307-322.
156. Quintanilla, A., et al., *Weakly bound capping agents on gold nanoparticles in catalysis: Surface poison?* Journal of Catalysis, 2010. **271**(1): p. 104-114.
157. Kilin, D.S., O.V. Prezhdo, and Y.N. Xia, *Shape-controlled synthesis of silver nanoparticles: Ab initio study of preferential surface coordination with citric acid*. Chemical Physics Letters, 2008. **458**(1-3): p. 113-116.
158. Al-Saidi, W.A., H.J. Feng, and K.A. Fichthorn, *Adsorption of Polyvinylpyrrolidone on Ag Surfaces: Insight into a Structure-Directing Agent*. Nano Letters, 2012. **12**(2): p. 997-1001.
159. Lu, Y., et al., *Thermosensitive Core-Shell Particles as Carrier Systems for Metallic Nanoparticles*. The Journal of Physical Chemistry B, 2006. **110**(9): p. 3930-3937.
160. Johnson, J.A., et al., *Size-Dependent Hydrogenation of p-Nitrophenol with Pd Nanoparticles Synthesized with Poly(amido)amine Dendrimer Templates*. Journal of Physical Chemistry C, 2013. **117**(44): p. 22644-22651.
161. Capone-Neto, A., et al., *Effects of early fluid resuscitation on cerebral hemodynamics and cerebral oxygen extraction in an experimental model of brain injury and hemorrhagic shock*. Critical Care Medicine, 1999. **27**(12): p. A63-A63.
162. Massalski, T.B., et al., *Binary alloy phase diagrams*. 1986, Metals Park, Ohio: American Society for Metals.
163. Boerma, D.O., et al., *Atomic Positions of Au Atoms on a Ni(110) Surface*. Surface Science, 1994. **307**: p. 674-679.
164. Knoppers, B., W. Ekau, and A.G. Figueiredo, *The coast and shelf of east and northeast Brazil and material transport*. Geo-Marine Letters, 1999. **19**(3): p. 171-178.
165. Figueiredo, J.L., *Reactivity of coke deposited on metal surfaces*. Materials and Corrosion-Werkstoffe Und Korrosion, 1999. **50**(12): p. 696-699.
166. Figueiredo, J.M.L., et al., *Optical modulation at around 1550 nm in an InGaAlAs optical waveguide containing an InGaAs/AlAs resonant tunneling diode*. Applied Physics Letters, 1999. **75**(22): p. 3443-3445.
167. Vijaykumar, G. and S.K. Mandal, *An abnormal N-heterocyclic carbene based nickel complex for catalytic reduction of nitroarenes*. Dalton Transactions, 2016. **45**(17): p. 7421-7426.
168. Shim, J.W., S.J. Park, and S.K. Ryu, *Effect of modification with HNO₃ and NaOH on metal adsorption by pitch-based activated carbon fibers*. Carbon, 2001. **39**(11): p. 1635-1642.
169. Baur, G.B., et al., *Activated carbon fibers for efficient VOC removal from diluted streams: the role of surface functionalities*. Adsorption-Journal of the International Adsorption Society, 2015. **21**(4): p. 255-264.
170. Baur, G.B., I. Yuranov, and L. Kiwi-Minsker, *Activated carbon fibers modified by metal oxide as effective structured adsorbents for acetaldehyde*. Catalysis Today, 2015. **249**: p. 252-258.

-
171. Brockner, W., C. Ehrhardt, and M. Gjikaj, *Thermal decomposition of nickel nitrate hexahydrate, Ni(NO₃)₂(·)6H₂O in comparison to Co(NO₃)₂(6H₂O)-H₂O and Ca(NO₃)₂(·)4H₂O*. *Thermochimica Acta*, 2007. **456**(1): p. 64-68.
 172. Johnston, H.S., et al., *The Kinetics of the Thermal Decomposition of Nitric Acid Vapor*. *Journal of the American Chemical Society*, 1951. **73**(5): p. 2319-2321.
 173. Richardson, J.T., R. Scates, and M.V. Twigg, *X-ray diffraction study of nickel oxide reduction by hydrogen*. *Applied Catalysis a-General*, 2003. **246**(1): p. 137-150.
 174. Biesinger, M.C., et al., *X-ray photoelectron spectroscopic chemical state quantification of mixed nickel metal, oxide and hydroxide systems*. *Surface and Interface Analysis*, 2009. **41**(4): p. 324-332.
 175. Torres, G.C., et al., *Effect of the carbon pre-treatment on the properties and performance for nitrobenzene hydrogenation of Pt/C catalysts*. *Applied Catalysis a-General*, 1997. **161**(1-2): p. 213-226.
 176. Ramaker, D.E., et al., *Nature of the metal-support interaction in supported Pt catalysts: Shift in Pt valence orbital energy and charge rearrangement*. *Journal of Catalysis*, 2001. **203**(1): p. 7-17.
 177. Coq, B., et al., *Influence of Support and Metallic Precursor on the Hydrogenation of P-Chloronitrobenzene over Supported Platinum Catalysts*. *Journal of Molecular Catalysis*, 1993. **79**(1-3): p. 253-264.
 178. Qiao, W.M., et al., *Preparation of an activated carbon artifact: oxidative modification of coconut shell-based carbon to improve the strength*. *Carbon*, 2002. **40**(3): p. 351-358.

Curriculum Vitae

EDUCATION

PHD IN CHEMICAL ENGINEERING Swiss Federal Institute of Technology Lausanne (EPFL) Group of Catalytic Reaction Engineering (GGRC)	2013–2017
MASTER OF SCIENCE MSC IN CHEMICAL ENGINEERING & BIOTECHNOLOGY Swiss Federal Institute of Technology Lausanne (EPFL) <ul style="list-style-type: none">• Master Project : « Removal of VOC Traces over Activated Carbon Fibers », <i>Best possible grade (6/6)</i>• Winter semester project about heterogeneous catalysis : « Hydrogenation of Chloronitrobenzene as a Case Study », <i>Best grade of the class (6/6)</i>	2010–2012
BACHELOR OF SCIENCE BSC IN CHEMISTRY Swiss Federal Institute of Technology Lausanne (EPFL)	2006–2010

WORK EXPERIENCE

CLINIQUE LA LIGNIÈRE S.A., Gland (Civilian Service) Quality assistant : Improvement of the Documentation System	09.2012–02.2013
SWISS FEDERAL INSTITUTE OF TECHNOLOGY LAUSANNE (EPFL) Teaching assistant : 3 rd year bachelor Chemical engineering practice (8h per week)	02.2012–06.2012
MERCK SERONO S.A., Aubonne QA Biotech intern : « Lead Time Reduction by optimizing the Production Batch Record Review in Quality Assurance Manufacturing group »	08.2011–01.2012
TUTORING In chemistry (about 2–4h per week)	2010–2012
CLINIQUE LA LIGNIÈRE S.A., Gland Receptionist/telephonist at the reception (about 8h per week)	2006–2011

ASSOCIATIVE INVOLVMENT

BARAMINE 2009 , association of the section of chemistry and chemical engineering to raise money for a study trip <ul style="list-style-type: none">• In charge of the drinks supplying and management within a bar during student manifestations	2009–2010
---	-----------

IT SKILLS

Office automation softwares : World, Excel, Powerpoint
Technical softwares : Matlab, Aspen

Curriculum Vitae

LANGUAGES

French : Mother tongue
English : B2 (Common European Framework of Reference for Languages), *Master courses in English, Time spent in England, Australia and in the US*
German : High School knowledge

MAIN INTERESTS

Organizing trips abroad with a group of friends, cinema

PUBLICATIONS

Lamey, D.; Beswick, O.; Cárdenas-Lizana, F.; Dyson, P. J.; Sulman, E.; Kiwi-Minsker, L., Highly selective immobilized bimetallic Ni-Au nanoparticle catalyst for the partial hydrogenation of m-dinitrobenzene. *Applied Catalysis A: General*. (submitted in February. 2017)

Beswick, O.; Parastaev, A.; Yuranov, I.; LaGrange, T.; Dyson, P. J.; Kiwi-Minsker, L., Highly dispersed cobalt oxides nanoparticles on activated carbon fibres as efficient structured catalysts for the transfer hydrogenation of m-nitrostyrene. *Catal Today* **2017**.

Beswick, O.; Lamey, D.; Muriset, F.; LaGrange, T.; Oberson, L.; Yoon, S.; Sulman, E.; Dyson, P. J.; Kiwi-Minsker, L., Ni-based structured catalyst for selective 3-phase hydrogenation of nitroaromatics. *Catal Today* **2016**, *273*, 244-251.

Beswick, O.; Yuranov, I.; Alexander, D. T. L.; Kiwi-Minsker, L., Iron oxide nanoparticles supported on activated carbon fibers catalyze chemoselective reduction of nitroarenes under mild conditions. *Catal Today* **2015**, *249*, 45-51.

Baur, G. B.; Beswick, O.; Spring, J.; Yuranov, I.; Kiwi-Minsker, L., Activated carbon fibers for efficient VOC removal from diluted streams: the role of surface functionalities. *Adsorption* **2015**, *21* (4), 255-264.

PRESENTATIONS

ICOSCAR-V, June 21st-24th, 2016. Donostia-San Sebastián, Spain. Oliver A. Beswick, A. Parastaev, Igor Youranov, Lioubov Kiwi-Minsker. Transition Metal Oxides Nanoparticles on Activated Carbon Fibres as Efficient Catalyst for Nitroarenes Reduction under Mild Conditions.

Europacat XII, August 30th – September 4th, 2015. Kazan, Russia. Oliver A. Beswick, A. Parastaev, Igor Youranov, Lioubov Kiwi-Minsker. Transition Metal Oxides Nanoparticles on Activated Carbon Fibres as Efficient Catalyst for Nitroarenes Reduction under Mild Conditions.

SCS Fall Meeting 2014, September 11th, 2014. Zürich, Switzerland. Oliver A. Beswick, Igor Youranov, Lioubov Kiwi-Minsker. Structured Fe₂O₃ –based Catalyst for Reduction of Nitroarenes under Mild Conditions.

Carbocat VI, 22–25 Juin, 2014. Trondheim, Norway. Oliver A. Beswick, Igor Youranov, Lioubov Kiwi-Minsker. Reduction of Nitroarenes over Nanosized Fe₂O₃ Supported on Activated Carbon Fibres under mild conditions.

Prizes

Teaching prize 2015 from the Chemistry and Chemical Engineering Section for outstanding teaching activities.

